University of Pretoria

Department of Materials Science and Metallurgical Engineering

Effect of Hot Working Characteristics on the Texture Development in AISI 430 and 433 Ferritic Stainless Steel

By

Kofi Ahomkah Annan

Supervised by

Dr. Charles W. Siyasiya

Prof. Waldo E. Stumpf

Submitted in Partial fulfillment of the requirement for the degree
Master of Science (Metallurgy)

In the

Department of Materials Science and Metallurgical Engineering
Faculty of Engineering, Built Environment & Information Technology

University of Pretoria
Republic of South Africa

November 2012.

UNIVERSITEIT VAN PRETORIA
UNIVERSITY OF PRETORIA
YUNIBESITHI YA PRETORIA

Acknowledgement

My first and foremost thanks go to the Almighty God for giving me grace to go through this study successfully. I would like to thank the many people who were so helpful and kind to me during my time at University of Pretoria. First, I wish to express my deepest gratitude to my supervisors, Professor W.E. Stumpf and Dr. C.W. Siyasiya**.** They provided an excellent environment to work in, generously extending immeasurable help, experience, direction and kindness throughout my studies. I would also like to thank the Advanced Material Division (AMD) of MINTEK for providing me with the assistantship in my hot rolling and texture measurement by bearing all the costs of such work. I am grateful to Mr. Richard Couperthwaite for all the help with the texture measurement at MINTEK. I am also very grateful to the Industrial Metals and Minerals Research Institute of University of Pretoria for provision of equipment for my studies. Columbus Stainless Steels needs a special mention and appreciation for provision of materials for the studies. I also thank the Centre for Materials Engineering of the University of Cape Town and in particular Dr. Sarah George for the high strain rate tests on the Gleeble 3800^{TM}. I would like to thank my fellow students who provided a great atmosphere for me at Tuks and Pretoria in general. I wish I could name them all as they all deserve it, but I would like to pick out Richard Nkhoma, Given Maruma, and Bundjoko Kweto. Finally, I would like to thank my family especially my wife, Celestine and my daughter Efua, for all of their support.

To everyone I left out; please accept my apologies and thanks.

Abstract

The last seven hot rolling passes of the ferritic stainless steels (FSS) AISI 430 and AISI 433 (the latter an Al-added variant of 430) were simulated on Gleeble-1500D® and Gleeble-3800TM® thermo-mechanical simulators to investigate the effect of temperature, strain rate and inter-pass time on the development of texture in these steel grades and its subsequent influence on ridging. The compression tests were carried out over a wide range of strain rates (0.1 s^{-1} to 5 s^{-1}, 25 s^{-1} and 50 s^{-1}) and temperatures (1100 to 820 ^{o}C) with different inter-pass times (2 s, 10 s, 20 s and 30 s). The transition temperature from dynamic recrystallization (which may introduce a texture change) to dynamic recovery (in which no texture changes are expected) was determined by examining the relationship between the mean flow stress and the deformation temperature in multi-pass tests. Both macrotexture (XRD) and microtexture (EBSD) analyses were employed to characterise and study the texture present in these steels. It was found that the texture in the central layer of the compressed sample is a strong recrystallization-type. The through-thickness textural and microstructural banding was found to be responsible for ridging in these grades of stainless steels. Dynamic recrystallization which promotes the formation of the desired γ-fibre texture leading to high ductility, formability and eventually reduction or elimination of ridging, was found to occur in both AISI 430 and AISI 433 at high temperatures, low strain rates and longer inter-pass times with multi-pass testing. Generally AISI 433 has a stronger gamma texture developed than the AISI 430 when hot rolled under similar conditions, which leads to improved ductility and less ridging in AISI 433 than AISI 430.

Keywords: Ferritic Stainless Steel, electron backscattering diffraction (EBSD), hot rolling, dynamic recovery, dynamic recrystallization.

Publications / Conference presentations

1. Annan KA, Siyasiya C.W, Stumpf W.E.: Effect of Hot Rolling Conditions on Ridging in 16 wt%Cr Ferritic Stainless Steel Sheet – Presented at the Ferrous Metals Development Network conference, Magaliesberg, South Africa, 15-17 October 2012 – Published conference proceedings, October 2012.
2. Annan KA, Siyasiya C.W, Stumpf W.E.: Effect of Hot Rolling Conditions on texture development in 16 wt%Cr Ferritic Stainless Steel Sheet – Submitted to the Journal of The South African Institute of Mining and Metallurgy –Under-review.
3. Annan KA, Siyasiya C.W, Stumpf W.E.: Hot rolling conditions and the development of texture in AISI 430 and AISI 433 Ferritic Stainless Steels –In preparation.

.

Candidate : Kofi Ahomkah Annan

Supervisors : Professor Waldo Edmund Stumpf
: Dr. Charles Witness Siyasiya

Department : Materials Science and Metallurgical Engineering

University : University of Pretoria, South Africa

Degree : MSc (Applied Science) (Metallurgy)

1 Table of Contents

2 List of Figures

3 List of Tables

4 List of Abbreviations

AMD	Advance Materials Division
FSS	Ferritic Stainless Steel
AISI	American Iron and Steel Institute
XRD	X-Ray Diffraction
EBSD	Electron Back Scattering Diffraction
DRX	Dynamic Recrystallization
SRX	Static Recrystallization
DRV	Dynamic Recovery
DR_{TT}	Dynamic Recrystallization to Dynamic Recovery Transition Temperature
RD	Rolling Direction
TD	Transverse Direction
ND	Normal Direction
FEI	Field Emission In-Lens
SEM	Scanning Electron Microscope
TEM	Transmission Electron Microscope
MFS	Mean Flow Stress
GBCD	Grain Boundary Character Distribution
ODF	Orientation Distribution Function
AOD	Argon-Oxygen Decarboriser
FCC	Face Centred Cubic
BCC	Body Centred Cubic
BCT	Body-Centred Tetragonal
SIBM	Strain Induced Boundary Migration
SAC	Selected Area Channelling
CBED	Convergent Beam Electron Diffraction
PC	Pattern Centre
FEGSEM	Field Emission Gun Scanning Electron Microscope
SSCCD	Slow-Scan Charge Couple Device
SIT	Silicon Intensified Target

CF	Cube-On-Face
CC	Cube-On-Corner
LDR	Limit Drawing Ratio
RT	Reheat Temperature
CSL	Coincident Site Lattice
LAGB	Low Angle Grain Boundary
HAGB	High Angle Grain Boundary

1 CHAPTER 1: GENERAL BACKGROUND

1.1 Introduction

Columbus Stainless Steel in Middleburg, South Africa; produces flat products of high quality stainless steels of which AISI 430 is one of the ferritic products of the company. One sector that is constantly growing in the use of this steel is the automotive components industry, especially in silencers (mufflers) of exhaust systems. The manufacture of automotive emission control systems in South Africa is one of the most rapidly growing industrial sectors in the world. Silencers of exhaust systems is the third largest automotive component exported from South Africa, since 2010 accounting for 5.5 % of the total automotive components exported from the country[1]. The trend of growth of exports of exhaust systems from South Africa has been significant, see Figure 1.1

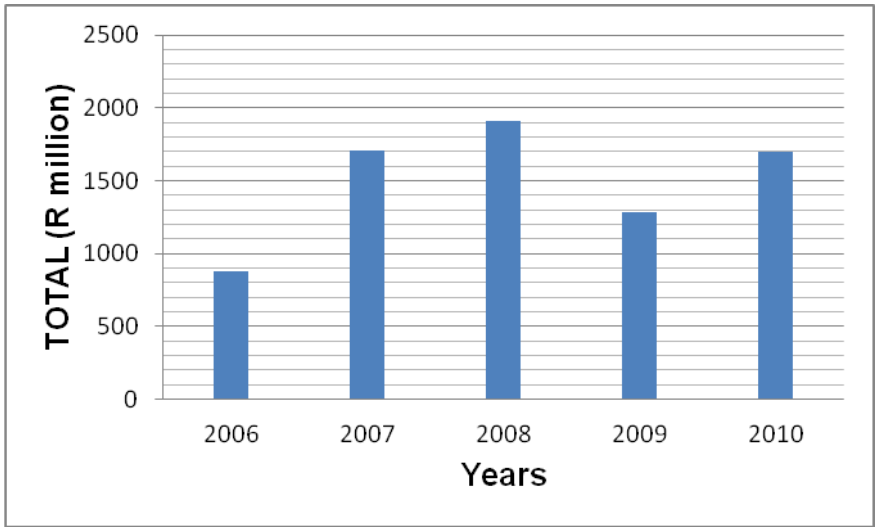

Figure 1.1: Exhaust systems industry growth in South Africa [1].

Mufflers of car's exhaust systems are used to moderate the level of noise produced by engines; they also decline deterioration and enhance performance of the internal combustion engines. The operating temperatures of mufflers are in the range of 140 ^{o}C – 400 ^{o}C, but due to an automobile's intermittent use, mufflers are associated with severe temperature fluctuations [2]. Hot exhaust gases and other wastes from the engine are discharged through the muffler of the exhaust system. Mufflers are

modeled in such a way that a low pressure is produced and the principle of sound cancellation is obeyed. See figure 1.2 below

Figure 1.2: Muffler fitted onto the exhaust of a car (a), and unfitted muffler (b).

Therefore, the material for such an application requires a non-heat treatable stainless steel with superior performance in its strength, ductility, formability, good corrosion and oxidation resistance, thermal conductivity and surface finish quality. The primary steel used in the production of mufflers is AISI 430 ferritic stainless steel. This steel is fully ferritic over a wide range of operating temperatures and the steel contains 16 wt% Cr which makes it dual phase during the hot rolling process (1100 ^{o}C – 800 ^{o}C) [3]. This phase change behaviour is confirmed by thermomechanical software such as Thermocalc^{TM}. Hot Rolling within this dual structure has consequences for drawability, grain structure and carbide distribution [2, 4]. The phenomenon of ridging is often observed which leads to the discarding of a large number of finished sheet items which raises the production costs. Ridging reduces the cosmetic quality of ferritic stainless steel (FSS) sheet. This undesirable surface defect obliges the manufacturer to add costs in a polishing operation. Ridging is characterised by the formation of surface ridges and troughs during the forming operation which run parallel to the original sheet rolling direction. Ridges in ferritic stainless steel sheet can lengthen over the entire sheet lengthwise, and may have a depth of 20 – 50 µm [4-7]. See figure 1.3.

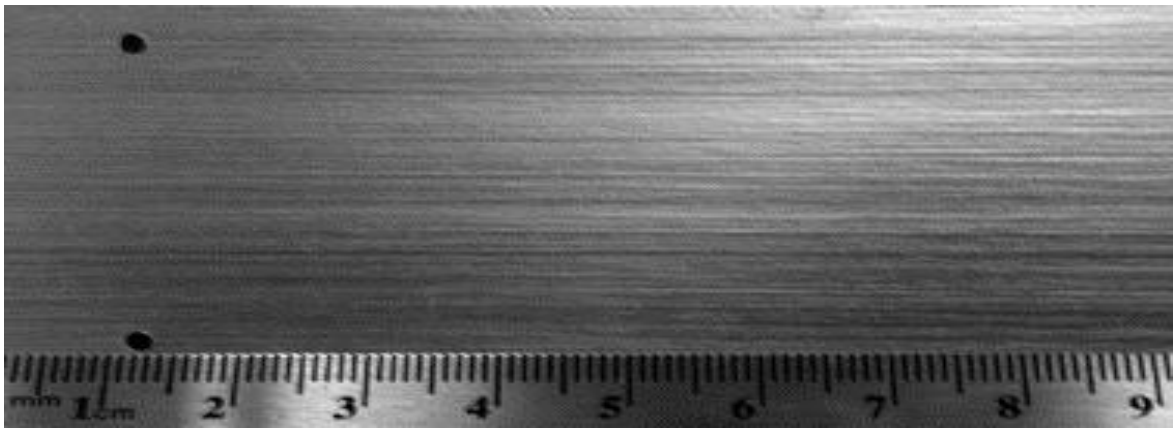

Figure 1.3: Ridging topography under uniaxial tension in the RD at 25 % elongation [5]

The initial texture and its spatial distribution were found to be the predominant factors for development of ridging [6 -8]. Undoubtedly ridging originates from anisotropic plastic flow of mixed textures and the origin of these textures may be traced to textural and microstructural banding during hot rolling [9]. To minimise ridging in AISI 430, aluminium (Al) addition has been made to the steel to increase the A_{c1} temperature such that finish rolling can occur in the ferritic region only. The addition of Al to AISI 430 has led to the designation of the steel as type 433 (also known as U-430DDQ). The characteristics of the AISI 430 and AISI 433 stainless steels depend on the chemical composition, casting practice and the thermomechanical processing conditions [8]. The compositions of the AISI 430 and AISI 433 stainless steels are shown in Table 1-1.

Table 1-1: The composition of AISI 430 and AISI 433 stainless steel (wt %) [10]

AISI 430	**C**	**Si**	**Mn**	**P**	**S**	**Cr**	**Ni**	**Al**
Min		1.0	1.0	0.04	0.015	16.0	0.75	
Max	0.08					18.0		0.008
AISI 433	**C**	**Si**	**Mn**	**P**	**S**	**Cr**	**Ni**	**Al**
Min		1.0	1.0	0.04	0.015	16.0	0.75	
Max	0.08					18.0		0.30

The effect of partial transformation on texture development in this steel during dynamic recrystallization as well as the degree or contribution of hot rolling conditions to the development of hot band texture and microstructure has clearly not been studied in depth [8-9].

1.2 Problem Statement

Columbus Stainless Steel experiences a surface defect problem from time to time resulting from texture produced during hot rolling which requires extra polishing cost to remove it. Complaints from customers indicate that ridging is greatly observed in this steel during applications involving stretching of the sheet in the rolling direction. This problem is considered to arise from anisotropic plastic flow of mixed textures. The origin of these textures may be traced to textural and microstructural banding during hot rolling. It was assumed that the ridging in this steel might be attributed to the pre-dominant texture resulting from hot rolling [7]. This is because the final texture present in the ferrite is an inherited texture from the austenite-ferrite phase change during the hot rolling stage within a temperature range of 1100 ^{o}C – 800 ^{o}C. It is believed that the thermomechanical conditions under which the sheets are rolled have a great influence on the kind of texture produced and subsequently on the ridging.

1.3 Objectives

The pre-dominant texture present in this steel which is influenced by the hot rolling conditions, has a direct effect on the occurrence of ridging. The following objectives have been identified:

- Determination of the contribution of the hot rolling conditions namely entry and exit temperatures, strain rate and inter-pass time to the formation of the pre-dominant texture during hot rolling.
- Determination of the relationship between the pre-dominant texture and ridging.

One common assumption, on which models used to study ridging in this steel are based, is the fact that there are longitudinal hot rolling bands in which the grains are similarly oriented [5].

2 CHAPTER 2: THERMOMECHANICAL PROCESSING OF FERRITIC STAINLESS STEELS

2.1 Introduction

Amongst the diverse reasons for thermal processing of stainless steels are: heating for hot working, annealing to soften after cold working, solution annealing to homogenize, heating to temper martensite, or to stress relieve. Differences in parameters such as strain rates, temperatures, inter-pass times, heating and cooling rates as well as the control of the atmosphere can have multifaceted and easily unintended consequences. Therefore a good understanding of the hot rolling process conditions is crucial in achieving desired properties of the steel. Many alloying elements found in stainless steels are thermodynamically reactive [11]. Thus many phases are thermodynamically possible at different hot rolling temperatures. The production of AISI 430 and AISI 433 stainless steels usually involves a mixture of raw materials comprising of chromium, iron, carbon and other alloying elements which are melted in an electric arc furnace. The steel is decarburised by blowing oxygen, argon and nitrogen into the molten metal contained in a vessel known as an Argon-Oxygen Decarburiser (AOD) before continuous casting into a solid strand. Slabs of typical dimensions of 900 mm and 1600 mm wide, 200 mm thick are cut into lengths of 4 m and 12 m through the use of a flame cutter at the exit of the continuous casting machine. The slabs are then passed through the processes of hot rolling in both a roughing mill as well as a Steckel mill, annealing and pickling, cold rolling and finishing and finally polishing [10, 12].

2.2 Stainless steels

Stainless steels are alloys having iron as the base element and containing at least 10.5 wt% chromium for adequate corrosion resistance. Currently the chromium content in some stainless steels, depending on the desired properties, even exceeds 30 wt%. Alloying elements are added for different reasons. Whilst the addition of austenite formers (Ni, Mn, Co, Ru, Pd, Rh, Os, Ir and Pt.) increases the austenitic phase at the expense of the ferrite, addition of ferrite formers (Si, Al, Be and P) leads to an increase in the ferrite phase at the expense of the austenite phase. Addition of Ti, V, Mo and Cr leads to formation of various

kinds of carbides such as $M_{23}C_6$, MC, M_7C_3 etc in the stainless steel. These alloying elements are added also for improved corrosion resistance (Cr, Ni, N, and Mo), strength (Mo, N, Al, Cu, and Ti), machinability (S and Se) and formability and toughness (Ni). Depending on the alloy content as well as the internal structures, upon rapid cooling stainless steels are categorized into three major classes namely; Austenitic (face-centred cubic, FCC), Ferritic (body-centred cubic, BCC) and Martensitic (body-centred tetragonal, BCT) stainless steels.

2.2.1 Austenitic stainless steel

This steel derives its name from its phase at room temperature as well as from its crystallographic structure, (FCC). They are most easily recognized as non-magnetic. These steels contain between about 16 wt% and 25 wt% chromium and 7 wt% -10 wt% nickel as well as nitrogen in solution. The Cr and the N contribute to their high corrosion resistance whilst nickel helps stabilize their austenitic structure. Due to their good mechanical properties and the ease of fabrication, austenitic stainless steels are more extensively used than ferritic stainless steels, accounting for about 75 % of worldwide stainless steel usage [11, 12].

2.2.2 Ferritic stainless steels

Ferritic stainless steels' name originates from the bcc crystallographic structure which is stable from room temperature up to the liquidus temperature. These steels contain between 11 wt% and 30 wt% of chromium. The ferritic stainless steels are the lowest-cost highly corrosion and oxidation resisting iron-based alloys in existence. Owing to their sufficient corrosion resistance and low cost they have become the preferred choice compared to austenitic stainless steels for less severe applications such as replacement of mild carbon steels in automobile exhaust systems. Ferritic stainless steels are fully magnetic. Generally, ferritic stainless steels are non-heat treatable with annealed yield strengths between 275 and 350 MPa [11-12]. They, however, have very poor weldability which leads to a fracture toughness reduction, mainly from grain growth in the HAZ [2].

2.2.3 Martensitic stainless steel

These alloys contain 12 to 17 wt % of chromium. Martensitic stainless steels are limited in their corrosion resistance because of the need of keeping alloy levels low to produce the martensitic structure. Austenite formers are added to form the necessary austenite during solution treatment for subsequent martensite formation. Martensitic stainless steels have a higher content of carbon which stabilizes the austenite at higher temperatures. The high carbon content increases their strength through interstitial solid solution strengthening and precipitation of large volumes of (Fe, Cr) carbides. The quench and temper process is usually used to achieve a high strength and appreciable ductility. Their superior hardenability which is achieved through the high carbon content, often leads to a reduction in the corrosion resistance as compared to that of austenitic and ferritic stainless steels.

2.3 Phase transformation in ferritic stainless steel

Highly alloyed ferritic stainless steels (FSS) unlike standard low-carbon steels undergo only limited phase transformations [6]. With an appreciable content of chromium, the gamma-phase field is suppressed while extending the alpha phase field at the same time. This eventually leads to the formation of the so called gamma loop shown in figure 2.1. In the absence of carbon and nitrogen, the gamma loop extends to a chromium content of just over 12 wt% [2, 13, and 14]. With higher chromium contents, no transformation to austenite takes place and therefore leaves the metal fully ferritic up to the melting point. In instances like this a completely different type of steel emerges in which grain refinement cannot take place by transformation through heat treatment [10-12].

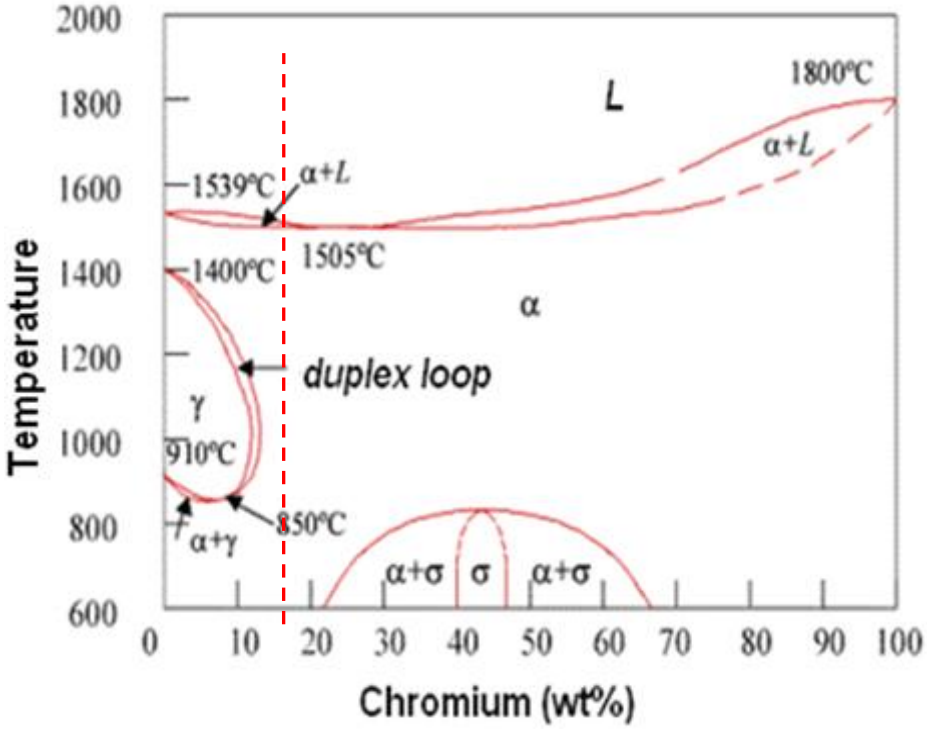

Figure 2.1: Fe-Cr phase diagram, the red dotted line represents the Cr content in the steels used for the studies [10, 13]

In the presence of carbon and nitrogen the gamma loop limit is shifted to a higher chromium content and finally a widening of the duplex (α + γ) phase area [12, 14]. When the interstitial content level is low enough, the grain boundary precipitates are suppressed if quenching is from above the solution treatment temperature [12, 15].

2.3.1 Solidification-phase relationships in the Fe–Cr–C system

The addition of carbon (an austenite former) to the Fe-Cr system leads to an increase of the gamma loop. To present the Fe-Cr-C ternary system, a pseudo binary diagram representing a two-dimensional projection of a three-dimensional diagram has been used (see figure 2.2) [15].

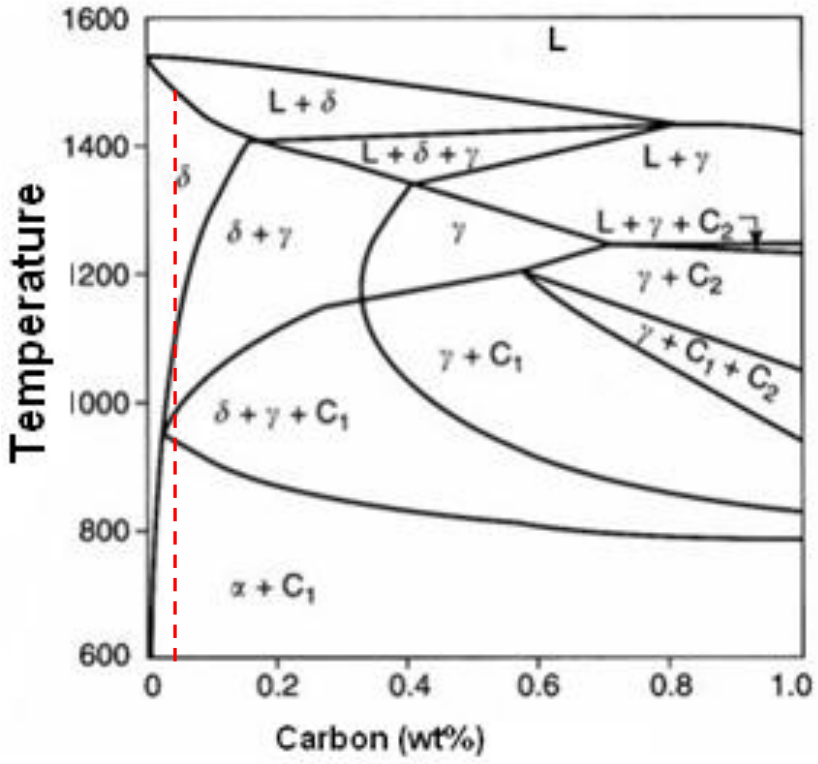

Figure 2.2: Fe-Cr-C pseudo-binary diagrams at 17 % Cr, Dotted red line shows the approximate Carbon content of AISI 430 and AISI 433 stainless steel [15].

This is a pseudo binary diagram based on 17 wt% Cr plotted with temperature as a function of varied carbon content. The carbides found in this type of steel as indicated on the diagram are $M_{23}C_6$ which is a Chromium-rich {$(Cr, Fe)_{23}C_6$} represented by C_1 on the diagram, M_7C_3 which is a {$Cr, Fe)_7C_3$} carbide represented on the diagram by C_2.

The alpha ferrite phase is a BCC solid solution of carbon in iron which usually exists in the low temperature range whereas the delta ferrite phase is the BCC solid solution that exists at high temperatures. The delta ferrite is formed during hot deformation at temperatures above 1100 °C and often is retained in the structure at room temperature. Heat treating the steels by holding at 1040 – 1100 ºC for at least 10 minutes, will dissolve up to 7-8 % delta ferrite but beyond that level, some delta ferrite remains in the structure as a second ferrite in phase. It is reported that, for hot-deformed steel, the presence of delta-ferrite in the structure sharply retards the growth of austenite grains with increasing quenching temperature [16, 17]. At these high temperature conditions, the phenomenon of precipitation of hard intermetallic compounds (such as Laves' phases, Sigma phase but not the

carbides) is found in the case of highly alloyed ferritic stainless steels stabilized with titanium, molybdenum and or niobium [17, 18,19]. However for the unstabilised AISI 430 and 433, after fast cooling to room temperature from the high temperature region where the structure of the steel is a mixture of austenite/ferrite, the microstructure of the alloy may transform into a mixed ferrite/martensite microstructure [18, 19].

2.4 Rolling schedule

2.4.1 Reheating temperature and undissolved particles

The reheating is done with the sole aim of achieving a uniformly heated slab in which the alloy carbides and carbo-nitrides $(Cr)_x(C,N)_y$ are fully dissolved. A suitable reheating temperature is chosen depending on the alloying elements present in the steel. The reheating temperature for AISI 430 and AISI 433 is between 1050 ^oC and 1150 ^oC [10]. At this temperature most of the carbides present in these steels would have been dissolved. A good compromise between the benefits of high and low reheating temperatures is needed. This is because high reheating temperatures will allow considerable grain growth to occur whilst at lower reheating temperatures; a larger proportion of alloying element precipitates will remain undissolved [18, 19].

2.4.2 Hot rolling of AISI 430 and AISI 433 ferritic stainless steels

AISI 430 and AISI 433 ferritic stainless steels are uniformly heated in the range of 1000 ^oC – 1100 ^oC for hot working. Their finish rolling temperature is usually kept below 750 ^oC and rapidly cooled through the temperature range 550 ^oC to 400 ^oC to avoid 475 °C embrittlement. Within the hot working range good hot ductility is achieved since no embrittling phase is formed. High diffusion rates inherent in the ferritic structures in the hot working temperature range makes homogenization easy [12, 20, 21 and 22]. During this stage the slabs are rolled on a reversing four high rolling mill to gauges between 65 and 25 mm. Thinner gauges are rolled down further on the Steckel mill to a predetermined gauge where the material can either be coiled (also known as hot band) or cut into plate (black plate) with thicknesses between 3 mm and 65 mm. The hot rolling operations are normally followed by annealing and then pickling to restore the mechanical properties and corrosion resistance [10, 22].

2.4.3 Rough rolling

The objective behind rough rolling of AISI 430 and AISI 433 is to achieve the optimal recrystallized austenite grain size before the dynamic recrystallization to dynamic recovery transition temperature (D_{RTT}) is reached [2]. The rough rolling phase is completed above the non–recrystallization temperature (D_{RTT}). Specially developed reduction schedules together with carbide precipitates that restrain growth of recrystallized austenite grains, are employed for this purpose [24]. For most flat ferritic stainless steel products the rough rolling temperature is within the temperature range of 850 ^{o}C to 1100 ^{o}C [10, 24 - 27].

2.4.4 Finish hot rolling

The objective of the finishing rolling stage in a Steckel rolling mill is to accumulate rolling strain within the austenite grains so that on subsequent ferrite transformation, ferrite nucleation sites are greatly multiplied in number and a very fine ferrite grain size can be generated during controlled cooling [10, 28]. This stage takes place within the non-recrystallized austenite region in the lower temperature range above Ar_3 [12, 21]. The starting temperature for this stage is in the region of 1050 ^{o}C to 950 ^{o}C and the finish rolling temperature is in the region of 750 ^{o}C to 850 ^{o}C [2, 19, and 10]. The total finishing reduction is usually about 64 to 80 % when the initial slab thickness and finishing thicknesses are 200 and 18 mm respectively [10].

2.4.5 Deformation stages during hot rolling process

Three stages of deformation during hot rolling are identified as:

- Deformation in the austenite recrystallization temperature region.
- Deformation in the ferrite recrystallization temperature region
- Deformation in the two-phase austenite-ferrite region

The major hot rolling variables during thermomechanical processing of AISI 430 and AISI 433 are the entry and exit temperatures, the strain per pass, its strain rate and the inter-pass time. During the austenite's recrystallization the reheating temperature and the solubility of alloying elements have a strong influence on the grain size of the initial austenite at the onset of hot working after reheating and the grain size of the recrystallized austenite [27-30]. The effect of the alloying elements depends on the reheating temperature.

The recrystallized grain size decreases rapidly as both are a function of an increase in reduction per pass and a decrease in the deformation temperature. The smallest austenite grain size can be attained by using deformations above the critical amount required for initiation of dynamic recrystallization during hot rolling [32-36].

2.5 Annealing and pickling of AISI 430 and AISI 433

The annealing process consists of heating the steel to a precise temperature for a preset period of time. The purpose of this is to reduce or relieve residual stresses induced by prior processing and to soften the steel for improved machinability or formability. The hot rolled products of AISI 430 and AISI 433 are softened (annealed) and descaled (pickled with HNO_3 acids) to produce the first semi-finished product. Annealing within the temperature range of 705 ^{o}C -790 ^{o}C for 90 minutes per 25 mm thickness (3.5 min/mm) is followed by air cooling. Controlled atmospheres are usually employed in the annealing furnace in order to avoid excessive oxidation of the surface [29, 31, 32-34]. Table 2-1 shows the temperature of annealing for various grades of ferritic stainless steels.

Table 2-1 Annealing temperatures for ferritic stainless steels [36]

Alloy Grade	Annealing temperature, (^{O}C)
Stabilized, Cr + Mo < 20 *409, *439, *18SR	870 – 925
Unstabilized, Cr + Mo < 20 *405, *430, *434, *436	705 – 790
Stabilized, Cr + Mo > 20 29-4C, Monit, Seacure, *444	1010 – 1065
Unstabilized, Cr + Mo > 20 *446	760 – 830

*the propriety trade name.

The driving force for recrystallization in ferritic stainless steels is limited by the lesser stored energy from deformation built into the BCC crystal structure. The prominent texture formed during deformation leads to annealing responses that are more precisely

characterized as recovery and grain growth with reduced recrystallization [37, 38]. The ability of ferritic stainless steels to retain their texture after annealing characterizes their anisotropic property exploited for good drawability. It is important to avoid excessive annealed grain size, which significantly reduces toughness. AISI 430 and AISI 433 which are interstitial bearing ferritic stainless steels need to be annealed subcritically to avoid the formation of austenite at higher temperatures that would lead to the formation of martensite on cooling. Characteristically, crucial batch annealing cycle for AISI 430 and AISI 433 alloys would be about 24 hours at 750 ^{o}C, the bulk time which represents time to achieve thermal equilibrium of the large coil mass. Practically, continuous annealing of ferritic stainless steel is not possible because the diffusion of carbon is too slow to occur in the short dwell time at the relatively low temperatures typical for ferritic stainless steels in continuous annealing lines. The batch annealing cycle with its much longer times precipitates basically all of the carbon and nitrogen as mixed Fe/Cr carbides and nitrides as well as promotion of homogenization of the chromium content [10, 38-43]

2.6 Softening mechanisms in AISI 430 and AISI 433

Softening mechanisms in AISI 430 and AISI 433 are either by recovery or recrystallization. These mechanisms reduce the energy added by deformation and occur either during the deformation (dynamic / DRX) or after the deformation (static / SRX) [42- 44].

2.6.1 Dynamic recovery of AISI 430 and AISI 433

Dynamic recovery is the process whereby dislocations are re-arranged into a lower energy configuration and the occurrence of this process is by numerous mechanisms which depend on the hot rolling parameters as well as the material composition [45, 46]. Dislocations of opposite signs either annihilate each other by combination or re-arrange themselves into a subgrain or cell structure consisting of a low dislocation density core surrounded by a higher dislocation density boundary region. The phenomenon is aided by cross-slip and dislocation climb at deformation temperatures. In a single pass, dynamic recovery will occur in the early stages of deformation in that pass and continues throughout the pass deformation. For BCC metals like AISI 430 and AISI 433, cross slip and climb of dislocations occurs with relative ease which leads to a decrease in dislocation density when dislocations encounter each other and diminish at new slip. This results in a

low dislocation density during hot working and eventually the occurrence of only dynamic recovery [41, 46-47]. This leads to a steady state, balancing work hardening with softening occurring due to rapid re-arrangement of these dislocations. The steady state subgrain size depends upon the strain rate and temperature [44-46].

2.6.2 Dynamic recrystallization of AISI 430 and AISI 433

The occurrence of dynamic recrystallization depends on the amount of remaining stored energy after the dynamic recovery has reached a steady state level which is usually lower than the amount of energy input by deformation. Numerical approaches have been used to show that the steady state stress is dependent upon the Zener-Hollomon parameter (equation 2.1) [46, 47].

$$\sigma_{ss} = 0.5361(Z)^{0.1122} \quad (2.1)$$

In most steel systems that are deformed in the austenitic region, the energy input is higher than that dissipated by dynamic recovery. Eventually the system reaches a critical point whereby new “strain-free” grains are formed during the deformation [39-42]. This phenomenon is known as dynamic recrystallization or DRX. The point after which the DRX is initiated when the dislocation density exceeds the critical value and the misorientation between neighbouring grains exceeds 15^{o}, is known as the critical stress σ_{cr}. This critical stress associated with various thermomechanical conditions can be expressed by the Zener-Hollomon parameter (equation 2.2) (figure 2.3) [47].

$$\sigma_{c} = 0.52(Z)^{0.1206} \quad (2.2)$$

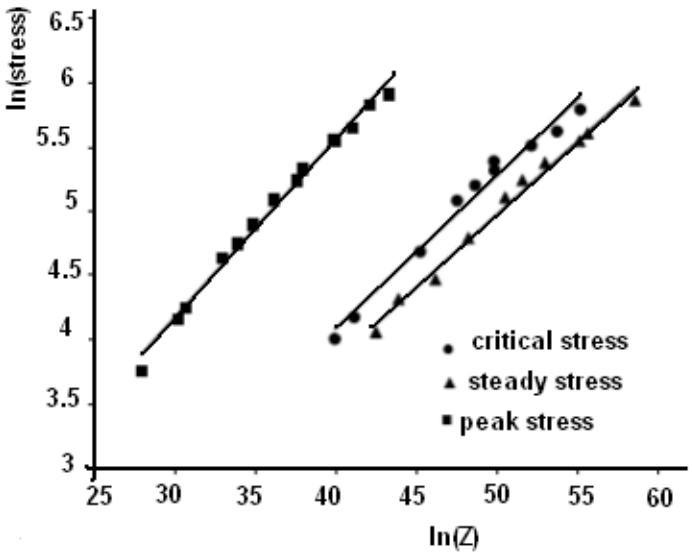

Figure 2.3: Dependence of critical, peak and steady state stresses on the Zener-Hollomon parameter for AISI 409 ($Q_{def.}$ = 400 kJ/mol K) [47]

However, in some BCC metals and under some hot rolling conditions, the softening achieved by dynamic recovery is so high as to prevent the critical energy level for DRX from being reached. One common measure through which the occurrence of dynamic recrystallization can be determined is by examining the shape of the true stress-true strain flow curve [47]. The decrease in flow stress during hot rolling after a peak has been reached is an indication of the occurrence of dynamic recrystallization [47]. The point on the flow curve whereby generation of new dislocations (due to deformation) is equal to the dislocation annihilation (due to recovery and recrystallization) is the steady state stress which has also been expressed through the Zener-Hollomon parameter as well in equation 2.3 [44- 47].

$$\sigma_{ss} = 1.31(2)^{0.13} \qquad (2.3)$$

Therefore the flow curve will follow a flat route (in DRV) or will drop to a steady state (in DRX) as shown in figure 2.4 [47].

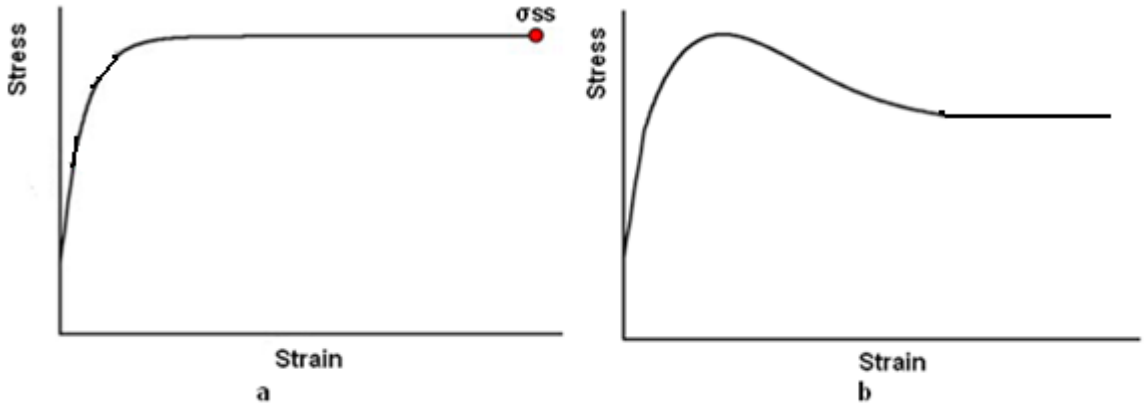

Figure 2.4: a) Schematic dynamic recovery curve, b) Schematic dynamic recrystallization curve [47]

One significant point applicable to the alloy of stainless steel being studied here is the effect that its crystal structure and the stacking fault energy have on the dynamic recrystallization behaviour. Body centred cubic crystal metals tend to recover to a high degree due to a higher mobility of dislocations in its loose packed lattice. This tendency limits the possibility of dynamic recrystallization in a BCC lattice by removing most of the driving force and making it difficult for the critical level of accumulated strain for DRX to be reached [47-50]. On the other hand, dislocations in an austenitic stainless steel with a FCC lattice and with mostly a low stacking fault energy have low mobility due to their difficulty to cross slip and they tend to retain their strain energy until DRX can take place. For instance, it has been observed that a localized occurrence of dynamic recrystallization near γ -particles in a ferritic microstructure takes place at temperatures above 1100 °C and at a strain rate of 1.0 s^{-1} [49, 50]**.** This dynamic recrystallization was evidenced by the formation of a substructure of smaller grains within the larger grains. TEM investigations have also confirmed the presence of high angle boundaries (>15°) between the observed dynamically recrystallized grains. The γ-particles, therefore, had the effect of strengthening the material and were found to be surrounded by a high dislocation density region due to incomplete recovery near the α-γ interface [50]. The dislocation (hence, energy) concentrations can then exceed the critical energy barrier for the nucleation of recrystallization. At temperatures below 1100 ^{o}C dynamic recrystallization initiated by these γ particles was generally not evident, except in some very isolated areas.

Generally, various studies seem to support the widely held view that widespread dynamic recrystallization is not very likely in ferritic stainless steels [47-52]. From the need for grain

boundary migration during recrystallization, steels with a higher interstitial content exhibit no dynamic recrystallization except under certain hot rolling conditions whereas steels with lower interstitial content display dynamic recrystallization behaviour more readily [46-49]. The presence of small particles or solute atoms slows down or stops the migration of the grain boundary, also known as Zener-pinning and Zener-drag respectively. Thus**,** a pure matrix would allow the grain boundaries to move more easily, thereby promoting recrystallization.

2.6.3 Nucleation of dynamic recrystallization

Nucleation is usually observed to occur at a critical strain, ε_c ($\varepsilon_c \approx 0.8\varepsilon_p$,) where ε_p is the peak strain on the true stress - true strain curve [47-51]. This critical strain value gives an indication of the amount of energy (stored from deformation) needed to overcome the activation energy barrier for nucleation to take place [47, 50, and 53]. The required dislocation density for nucleation depends on factors such as strain rate, temperature, inter-pass time and chemical composition. Low strain rates lead to the start of dynamic recrystallization through the bulging of pre-existing grain boundaries [49, 50] by the Strain Induced Boundary Migration (SIBM) mechanism whereas at higher strain rates dynamic recrystallization often occurs by growth of subgrains to form a high angle grain boundary (> 15^o) through annihilation of dislocations when they encounter each other on new slip systems [51, 52]**.** The difference in dislocation density between the highly deformed matrix ahead and the less deformed matrix behind such moving interfaces serves as the driving force (from the stored energy) for the migration of the grain boundaries [51-55]. The preferential site for nucleation is usually along the existing grain boundaries. This behaviour is described as 'necklacing' (see figure 2.5) which refers to the band of fine, new grains surrounding an early deformed grain [47, 52-55]. These new grains grow into the older grain until impingement with other growing grains takes place. Once all of the grain boundary sites are occupied, new grains are formed at the boundary between the unrecrystallized and the recrystallized ones. Characteristically the initiation of DRX is preceded by growing fluctuations of the grain boundary's shape. Dynamic recovery serves as an important forerunner to dynamic recrystallization in this instance. The substructures formed during dynamic recovery then become the basis for the nucleation sites in recrystallization [46-55].

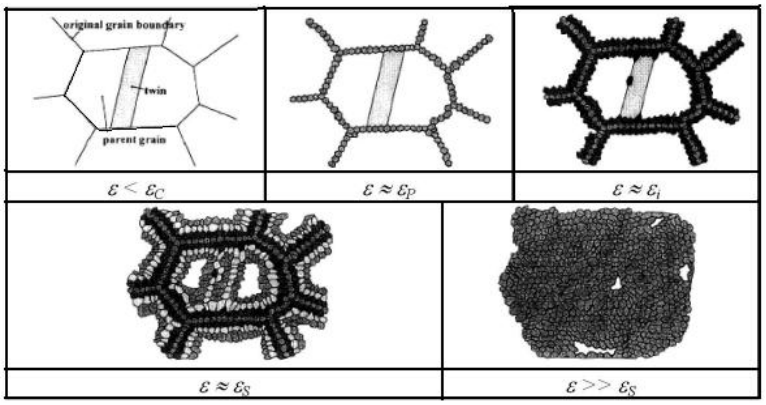

Figure 2.5: DRX evolutions by the necklace mechanism in stainless steels [55].

The recrystallization texture of ferritic stainless steels (BCC metals) may be attributed to the preferred orientation of recrystallized nuclei at the pre-existing high-angle grain boundaries between the deformed grains, where the optimum nucleation conditions exist [57]. Due to the nucleation within the as-deformed microstructure, the new grains will inherit the orientations of the former rolling texture [54-57].

3 CHAPTER 3: TEXTURE DESCRIPTION AND MEASUREMENT

Texture determination and interpretation are of fundamental importance in materials technology. The texture evolution analysis during the thermomechanical processing of materials yields valuable information about metallurgical processes such as deformation, recrystallization and phase transformations [55-57].

3.1 The Orientation Coordinate systems

Two reference frames forming a coordinate system usually in Cartesian form, are chosen to specify orientations [57-59]. The first of these two frames relates to the sample and the second one relates to the crystal. The ordinates of the sample or specimen coordinate system S = {$S_1S_2S_3$} are chosen according to significant rolling directions associated with the external form or shape of the sample. The directions associated with the external shape are the rolling direction (RD); the direction normal to the rolling plane (ND); and the transverse direction (TD) (See Figure 3.1) [56-61].

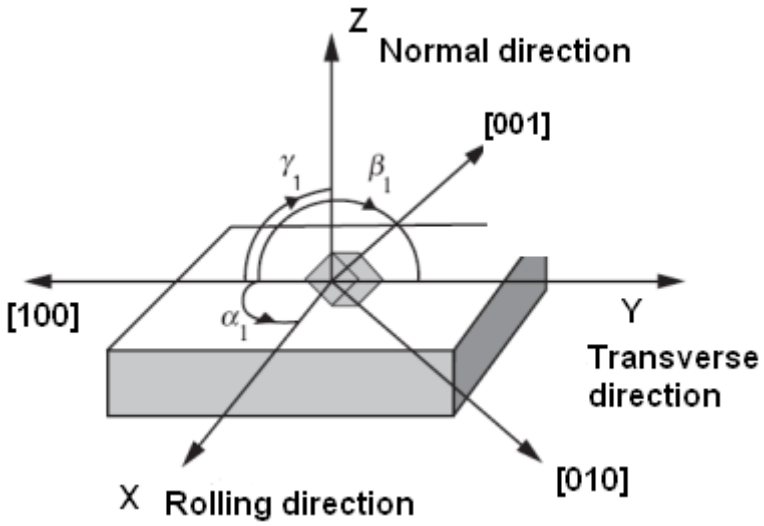

Figure 3.1: Relationship between the sample coordinates system XYZ (or RD, TD, ND for a rolled product) and the crystal coordinate system [100], [010], [001] [59].

The second coordinate system which constitutes the crystal coordinate system *C* = {$C_1C_2C_3$} is specific with respect to directions in the crystal. For cubic crystals, the axes [100], [010], [001] already form an orthogonal frame (see figure 3.2). Hence the crystal axes are made orthonormal, meaning all normalized to be of the same length [57-60].

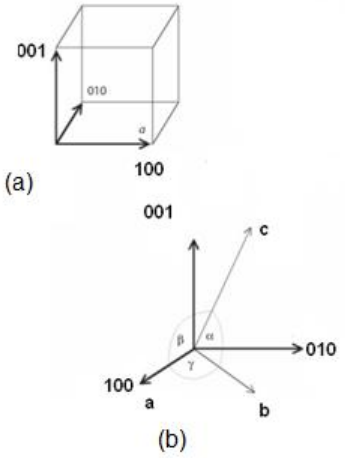

Figure 3.2 Ortho-normalized crystal coordinate systems for (a) cubic (b) general (triclinic) symmetries [57]

Generally by pre-multiplying a zone axis referenced to the crystal coordinate system, by a matrix L with the following entries [59], the following relationships are found:

$L_{11} = a$, $L_{12} = b\cos\gamma$, $L_{13} = c\cos\beta$, $L_{21} = 0$, $L22 = b\sin\gamma$, then

$$L_{23} = \frac{c(\cos\alpha - \cos\beta\cos\gamma)}{\sin\gamma}$$

$L_{31} = 0$, $L_{32} = 0$ and

$$L_{33} = \frac{c(1 + 2\cos\alpha\cos\beta\cos\gamma - \cos\beta - \cos\gamma)}{\sin\gamma} \qquad (3.1)$$

where a, b and c are the lattice parameters and α, β, γ are the inter-zone angles, see figure 3.2 (b). In this way all crystal systems have the same kind of crystal coordinate system (orthonormal). The general matrix in equation 3.1 can be solved in the triclinic form. Since in orthorhombic crystals all angles are 90°, the transformation matrix L will then become:

$$L = \begin{pmatrix} a & 0 & 0 \\ 0 & b & 0 \\ 0 & 0 & c \end{pmatrix} \qquad (3.2)$$

To transform from orthonormal coordinates to the crystal reference coordinate system, it is necessary to pre-multiply by the inverse of the crystal matrix L^{-1} [56-61].

3.2 The rotation or orientation matrix

An orientation can be defined as “the position of the crystal coordinate system with respect to the sample coordinate system,” (as shown in figure 3.2). This can be expressed mathematically as in equation 3.3 below:

$$C_c = g \,.C_s \qquad (3.3)$$

where C_C and C_S are the crystal and sample coordinate systems, respectively, and g is the orientation matrix which is a 3 x 3 square matrix. The first row of the matrix is given by the cosines of the angles α_1, β_1, γ_1 between the first crystal axis [100] and each of the three sample axes X, Y, Z, in turn (see Figure 3-2). The middle row of the orientation matrix is given by the cosines of the angles α_2, β_2, γ_2 between [010] and X, Y, Z in turn. Correspondingly, the last row of the matrix is comprised of the cosines of the angles α_3, β_3, γ_3 between [001] and X, Y, Z. This leads to derivation of the complete matrix in equation 3.4 below:

$$g = \begin{pmatrix} \cos\alpha_1 & \cos\beta_1 & \cos\gamma_1 \\ \cos\alpha_2 & \cos\beta_2 & \cos\gamma_2 \\ \cos\alpha_3 & \cos\beta_3 & \cos\gamma_3 \end{pmatrix} = \begin{pmatrix} g_{11} & g_{12} & g_{13} \\ g_{21} & g_{22} & g_{23} \\ g_{31} & g_{32} & g_{33} \end{pmatrix} \equiv \begin{pmatrix} 0.768 & -0.582 & 0.267 \\ 0.384 & 0.753 & 0.535 \\ -0.512 & -0.308 & 0.802 \end{pmatrix} \qquad (3.4)$$

Equation 3.4 is a representation of the orientation matrix in terms of the direction cosines, elements and a numerical example for a specific orientation and can enable a crystal direction to be expressed in terms of the sample direction to which it is parallel and vice versa [59-61]. An orientation matrix is a mathematical tool for the calculation of all the other descriptors of orientation in a cubic crystal structure.

3.3 Crystallographic solutions of a cubic material

A cubic crystal can be arranged in 24 different ways. This implies that, there are 24 solutions for an orientation matrix of a material having cubic symmetry. These matrices which describe the symmetry operations are the total sum of two rotations of 120° about each of the four ⟨111⟩, three rotations of 90° about each of the three ⟨100⟩, and one rotation of 180° about each of the six ⟨110⟩ and the identity matrix. Depending on what method is chosen to represent an orientation (Miller indices, angle/axis pair, Rodriguez vector, Euler angles) or misorientation, the selection of a particular crystallographic related

solution may both facilitate representation and allow insight into the physical meaning of the data [59].

3.4 The reference sphere

Representation of the 3-D orientation information on the unit sphere in a two-dimensional (2-D) plane requires a projection of the sphere onto that plane. In crystallography and metallurgy, most commonly the stereographic projection is used (See figure 3.3).

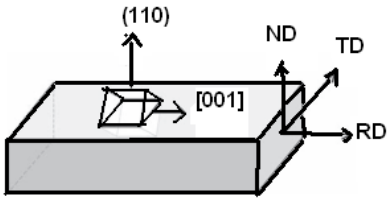

Figure 3.3: Schematic illustration of the relationship between the crystal and specimen axes [59].

These are simple stereographic projections which show the distribution of particular crystallographic directions in an assembly of grains making up the microstructure. Pole figures and inverse pole figures must also contain directions to have a meaning [58-61].

3.4.1 The pole figures

Poles are projected from the reference sphere whereby the position of a given pole on the sphere is normally characterized in terms of Φ and ψ angles [59-61]. The azimuth of the pole is described by Φ, where Φ = 0° is the north pole of the unit sphere and the angle ψ characterizes the rotation of the pole around the polar axis. In order to characterize the crystallographic orientation of the crystal, the spatial arrangement of the corresponding poles in terms of the angles Φ and ψ has to be determined with respect to an external reference frame (sample coordinate system S). For rolling symmetry, the sheet normal direction ND is typically chosen to be in the north pole of the sphere, so that Φ = 0° for ND, and the rotation angle ψ = 0° for the rolling direction RD. For other deformation modes or sample geometries an appropriate 3-D, preferably right-handed, coordinate system has to be established [58].

Suppose K is a vector parallel to the pole of interest (XYZ), then it can be expressed in the two frames S and C according to equation 3. 5 (a) and 3.5 (b)

$$K = s_1 \sin\alpha\cos\beta + s_2 \sin\alpha\sin\beta + s_3 \cos\alpha \quad (3.5a)$$

and

$$K = \frac{1}{M}(c_1X + c_2Y + c_3Z) \quad (3.5b)$$

Where (XYZ) are the coordinates of the pole in the crystal frame, for example, (111), and M is a constant being given by the relation: $M = \sqrt{X^2 + Y^2 + Z^2}$ to normalize K to unity.

$$\begin{pmatrix} \sin\alpha\cos\beta \\ \sin\alpha\sin\beta \\ \cos\alpha \end{pmatrix} = \frac{1}{M}\begin{pmatrix} g_{11} & g_{21} & g_{31} \\ g_{12} & g_{22} & g_{32} \\ g_{13} & g_{23} & g_{33} \end{pmatrix} \bullet \begin{pmatrix} X \\ Y \\ Z \end{pmatrix} \quad (3.6)$$

Out of equation 3.6 nine equivalent expressions are developed to derive the pole figure angles α and β for a given pole (XYZ) from the orientation matrix g [59]. Orientation within a cubic crystal, is described by the three {100}, four {111}, six {110}, twelve {012}, {112}, {113}, etc., and in the most general case twenty-four {hkl} poles. This implies that all pole figures of cubic crystals have enough poles to describe clearly its orientation [59- 61].

3.4.2 The inverse pole figures

The representation whereby the orientation of the sample coordinate system can be projected onto the crystal coordinate system is known as the inverse pole figure. Thus, making the crystal coordinates system C the reference system of the inverse pole figure and the “orientation” is defined by the axes of the sample coordinate system S, for example RD, TD, and ND. In this case;

$$S_i = c_1 \sin\gamma_i\cos\delta_i + c_2 \sin\gamma_i\sin\delta_i + c_3 \cos\delta_i \quad (3.7)$$

Where γ_i and δ_i are angles of a vector parallel to the specimen axis in the coordinate system.

Scalar multiplication now leads to (equation 3.8)

$$\begin{pmatrix} \sin\gamma\cos\delta \\ \sin\gamma\sin\delta \\ \cos\delta \end{pmatrix} = \begin{pmatrix} g_{11} & g_{12} & g_{13} \\ g_{21} & g_{22} & g_{23} \\ g_{31} & g_{32} & g_{33} \end{pmatrix} \bullet \begin{pmatrix} Xs \\ Ys \\ Zs \end{pmatrix} \quad (3.8)$$

Inverse pole figures are often used for axial symmetric specimens where only one of the axes is prescribed. In the case of cubic crystal symmetry the well-known unit triangle ⟨100⟩, ⟨110⟩, and ⟨111⟩ are used [56-59].

3.4.3 The Euler angles

The Euler angles refer to three rotations when performed in the correct sequence, to transform the sample coordinate system onto the crystal coordinate system, in other words, it specifies the orientation g ,see figure 3.4. The most popularly used conventions are those formulated by Bunge [58, 59].The rotations based on the Bunge notation are:

1. φ_1 about the normal direction ND, transforming TD into TD' and RD into RD'.
2. Φ about the axis RD′ (in its new orientation)
3. φ_2 about ND″ (in its new orientation)

where φ_1, Φ, φ_2 are the Euler angles (Bunge definition) [59]. Analytically, the three rotations expressed in matrix form are given by equations 3.9

$$g\varphi 1 = \begin{pmatrix} \cos\varphi_1 & \sin\varphi_1 & 0 \\ -\sin\varphi_1 & \cos\varphi_1 & 0 \\ 0 & 0 & 1 \end{pmatrix} \quad (3.9a)$$

$$g_{\Phi} = \begin{pmatrix} 1 & 0 & 0 \\ 0 & \cos\Phi & \sin\Phi \\ 0 & -\sin\Phi & \cos\Phi \end{pmatrix} \quad (3.9b)$$

$$g_{\varphi_2} = \begin{pmatrix} \cos\varphi_2 & \sin\varphi_2 & 0 \\ -\sin\varphi_2 & \cos\varphi_2 & 0 \\ 0 & 0 & 1 \end{pmatrix} \quad (3.9c)$$

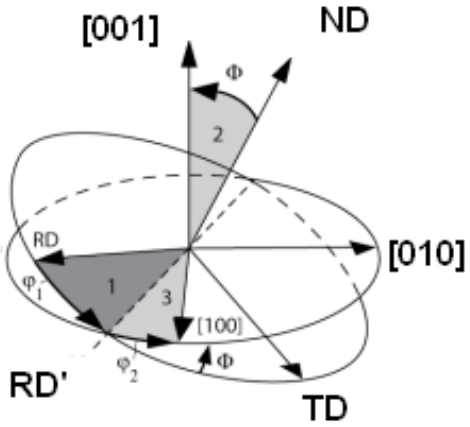

Figure 3.4: Rotation through the Euler angles φ_1, Φ, φ_2, in order 1, 2, 3 describing the rotation between the sample and crystal axes [59]

By multiplication of these three matrices in order, an expression linking the rotation matrix g to the three Euler angles is obtained.

$$g = g\varphi_2 \cdot g\Phi \cdot g\varphi_1 \tag{3.10}$$

The ideal orientation for specific orientation given by equation 3.4 is (123)[634] and this can equivalently be expressed as Euler angles φ_1 = 59.0°, Φ = 36.7°, φ_2 = 51.2°. From the definition of the Euler angles, it follows that they are periodic with period 2π, hence:

$$g\{\varphi_1 + 2\pi, \Phi + 2\pi, \varphi_2 + 2\pi\} = g\{\varphi_1, \Phi, \varphi_2\} \tag{3.11}$$

$$g\{\varphi_1 + \pi, 2\pi - \Phi, \varphi_2 + \pi\} = g\{\varphi_1, \Phi, \varphi_2\} \tag{3.12}$$

This means that there is a glide plane in the Euler angle space. Thus, in the most general case, the Euler angles are defined in the range 0° ≤ φ_1, φ_2 ≤ 360°, and 0° ≤ Φ ≤ 180°. It is noted, however, that the sine and cosine functions are only defined in the range –90° ≤ φ_1, Φ, φ_2 ≤ 90°. Other notations (conventions) used to describe Euler angles are those proposed by Roe and Kocks [59, 61].

The relationships between Roe, Kocks sets and the Bunge angles are as Follows:

Bunge-Roe $\varphi_1 = \psi + \pi/2$ $\Phi = \Theta$ $\varphi_2 = \Phi - \pi/2$ (3.13(a))

Bunge-Kocks: $\varphi_1 = \psi + \pi/2$ $\Phi = \Theta$ $\varphi_2 = \pi/2 - \Phi$ (3.13(b))

3.5 Texture analysis techniques

Texture analysis techniques can be grouped into macrotexture techniques (based on x-ray or neutron diffraction) and microtexture techniques (based usually on electron diffraction). With macrotexture techniques, the primary output is a profile of diffracted intensities, which is characteristic of a large neighbouring sample volume, whereas with microtexture techniques, the primary output is a diffraction pattern from individual grains [56-61].

3.5.1 The Kikuchi patterns

A Kikuchi diffraction pattern is obtained through the following electron diffraction techniques [59]:

• Selected Area Channelling (SAC) in SEM
• EBSD (Electron Back Scatter Diffraction) in SEM
• Microdiffraction or convergent beam electron diffraction (CBED) in TEM.

With regard to EBSD in SEM, diffraction occurs from the interaction of primary "backscattered" electrons with lattice planes close to the sample surface [59-61].

3.6 EBSD based microtexture technique

EBSD in SEM is undoubtedly the most widely used technique for the determination of microtexture [57, 58]. The steps necessary to produce an EBSD pattern in a SEM are as follows:

- Tilting of the sample so that its surface makes an angle ~>60° with the horizontal;
- Turning off the scan coils to obtain a stationary electron beam;
- Placing a recording medium in front of the tilted sample to capture the diffraction pattern.

The major reason for tilting the sample is to reduce the path length of electrons that have been backscattered by lattice planes as they enter the sample and this allows a far greater percentage of these electrons to undergo diffraction and escape from the sample, without losing any of their energy before being absorbed (see figure 3.5) [56-62].

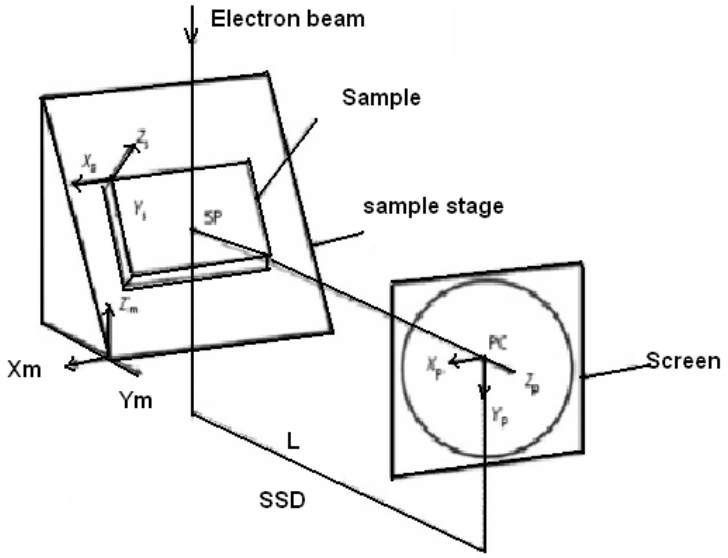

Figure 3.5: Parameters required for EBSD orientation measurements [59].

To determine orientation measurements from EBSD patterns, it is essential to identify the following parameters [62]:

• The coordinates of the pattern center, PC

• The specimen-to-screen distance L

• The relationship between reference directions in the microscope $X_mY_mZ_m$, sample $X_sY_sZ_s$, and screen/pattern XYZ.

These parameters depend on the relative positions of the camera and sample within the microscope [59]. Inadequate or inappropriate sample preparation could lead to misleading data interpretation. For instance, the diffuseness of an EBSD pattern is a guide to the amount of plastic strain in the lattice; however, if a sample contained diamond polish damage prior to etching, the pattern might be interpreted inaccurately as arising from a deformed sample. Interpretations are only valid after proper sample preparation [59-62].

3.6.1 Determination of sample position for EBSD analysis

In the use of EBSD to gain a representation of the overall texture, consideration must be given to the location and sample population size of the constituent orientations. A rolled product sample may be mounted so as to extract microtexture data from the “side” of the sheet (see Figure 3.6) [48, 50, 59].

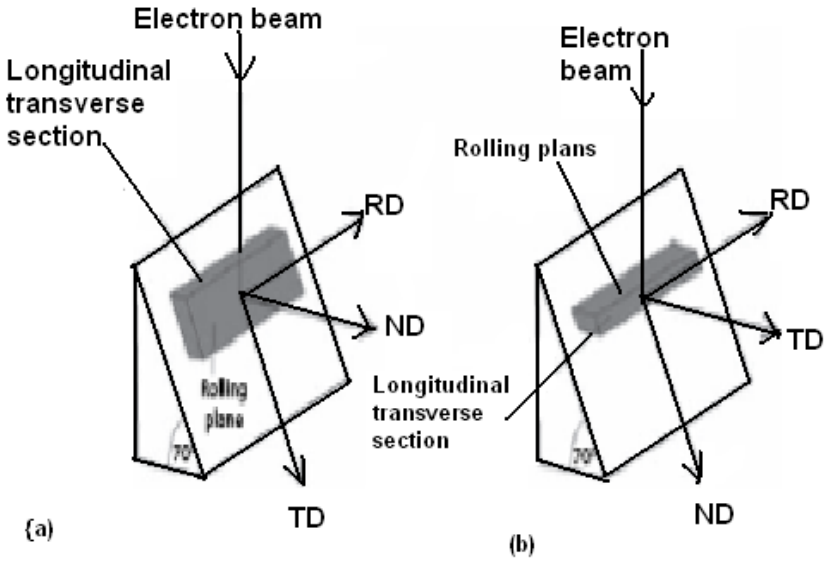

Figure 3.6: Examples of choices for mounting an EBSD sample either on (a) the rolling plane (RD-ND) or (b) the longitudinal–transverse section (RD-TD)[59, 61].

A step size of one tenth of the average grain size is chosen as a starting point for microtexture and grain misorientation measurements. EBSD's accuracy for orientation measurement has been found experimentally to be approximately within the range of 0.5°–1.0° [59].

3.7 Experimental Considerations for EBSD

To reflect the EBSDs versatility, many methodology options and operating conditions of microscope used in microtexture analysis are available these days.

3.7.1 Hardware

An EBSD system can be added as an accessory to virtually any SEM, See figure 3.7 which shows the state-of-the-art components of an EBSD.

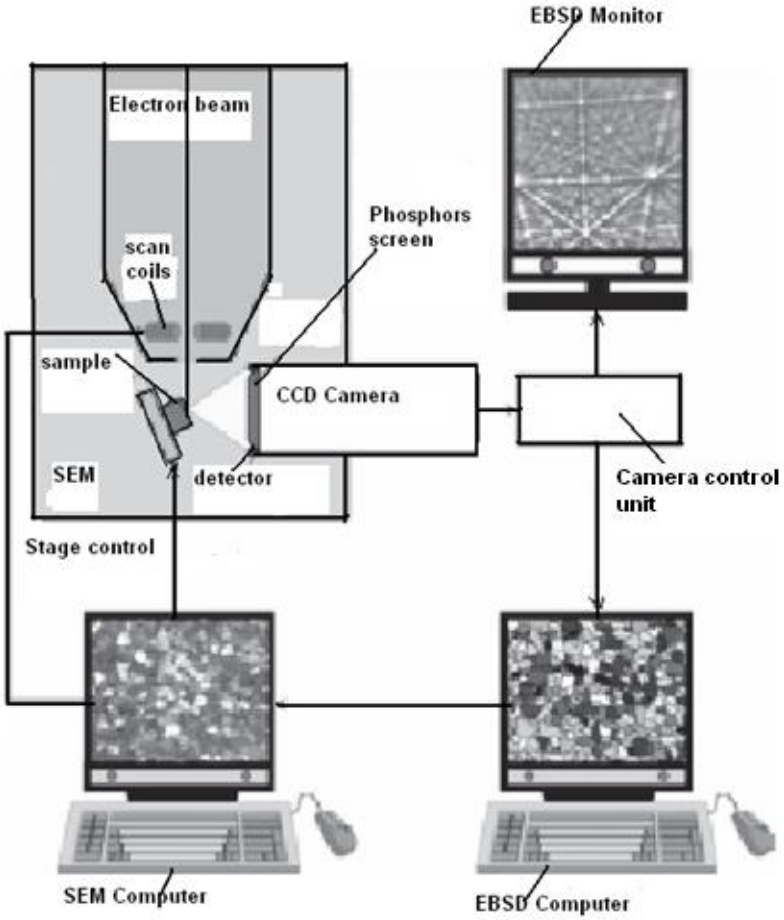

Figure 3.7: Components of a state-of–the-art EBSD system [59]

Field emission gun SEMs (FEGSEMs) have undoubtedly become gradually more popular for EBSD due to their increase in spatial resolution, which is about two to three times that of a tungsten filament SEM. [59, 60]. A slow-scan charge-coupled device (SSCCD) video camera with solid state sensors has replaced the first generation of silicon intensified target (SIT) cameras used for EBSD. In microtexture, rapid data acquisition is a prime consideration where a television (TV) camera rate combines adequate speed with enough pattern contrast and definition. The most important hardware component of EBSD is the camera. The other most important components of an EBSD system are a computer and dedicated software to control the camera, data processing, pattern indexing, analysis, and output [59-62].

3.7.2 Microscope Parameters

The kind of SEM has a major effect on the interaction volume and consequently on the spatial resolution. A FEGSEM is capable of some threefold improvement in spatial resolution compared to a tungsten-filament SEM, with a LaB6 SEM performance in between the two. This has been confirmed in many investigations including deformed materials, nanocrystals and measurements close to grain boundaries. The use of a FEGSEM has therefore extended the range of EBSD applications, especially into areas that were originally reserved for TEM [59, 61-63].

3.7.3 Data Collection Efficiency

Proficient data collection is an advantage in EBSD analysis. The total time required per map pixel is the sum of the time taken to move to the map coordinates and to site the electron probe, the time taken to collect a diffraction pattern, and the time taken to analyze the pattern. Most gains made in data collection speed are due to the improvements in camera technology [60-63]. However, it is important that gains in speed do not incur any loss in indexing accuracy or spatial resolution [57, 59, 62]. Factors determining the data collection speeds in individual cases are: the type of SEM, EBSD camera, operating parameters, and sample type. A low-resolution Hough transform and few Kikuchi bands can however increase the pattern-indexing rate [59, 63].

3.7.4 Sample/Microscope Geometry

Parameters that can be altered in the microscope/EBSD setup are the sample-to-screen distance, the sample tilt, and the sample height (working distance) in the microscope. These parameters' values are essential in calibrating the system in order to index the diffraction pattern. Normally for EBSD data collection, the sample-to-screen distance remains fixed. EBSD patterns have been observed for sample tilt of angles greater than 45°. Tilt angles greater than 80° are not viable because of the excessive anisotropy of the sampled volume and distortion in the uncorrected image, see figure 3.8 below [57, 59, 63].

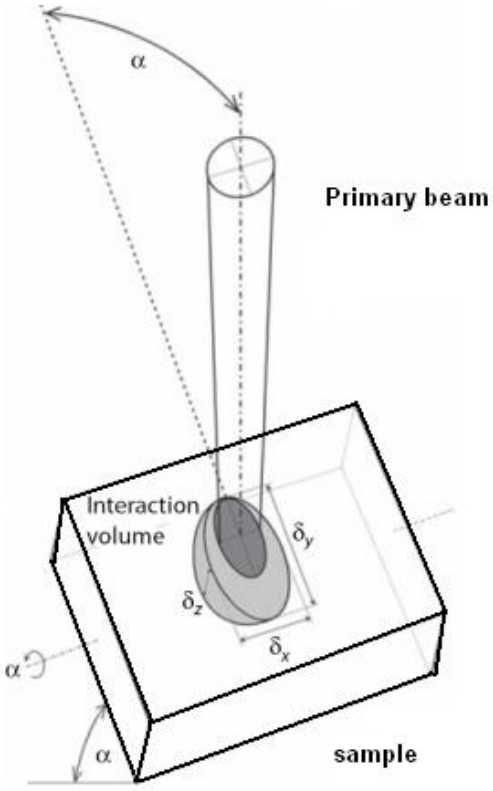

Figure 3.8: The sample – beam interaction volume in a sample tilted for EBSD [59]

A tilt angle of 70° is mandatory for one calibration routine. This value represents a good compromise between convenience and pattern contrast; it is therefore used as a standard angle for EBSD [57, 59, and 62]. The best possible working distance is often in the range 15–25 mm. Some calibration routines dictate a fixed working distance. Accelerating voltage is typically 20 kV. The latest FEGSEMs provide sufficient beam current at typically 5–10 kV, hence allowing further gains in resolution.

3.8 Representation of Microtexture Data

A microtexture is essentially a population of individual orientations that can be linked to their location in a sample and is usually obtained by an electron diffraction technique. Two factors to consider are the discrete nature of the orientation data and their direct link to the microstructure. These introduce a much broader and more complex scenario for data evaluation and representation than that for macrotextures. The nature of microtexture gives rise to two lines of inquiries: statistical distribution of the orientation data and orientation data relation to the microstructure. Two ways in which orientation and

misorientation microtexture data can be displayed in a space are firstly, as discrete data points and secondly as a continuous density distribution function (ODF) [56-62].

3.8.1 Statistical Distribution of Orientation and Misorientation Data

The principal aim of microtexture representation is basically to represent and quantify the orientation distribution in a region of interest in the microstructure, either by sampling every orientation present or by statistically sampling throughout a large region of the sample. Since automated EBSD is sometimes very rapid and able to measure directly the “true” grain orientation, the statistical analysis mode is used advantageously in place of a traditional macrotexture technique to generate a measure of the overall texture. In EBSD, depending on the size of the sample, the grain size and the mapping speed, the number of grains encountered may be smaller than the number of grains contributing to x-ray or neutron pole figure measurements [59-64]. For instance, in a sampling area of 10 × 10 mm^2 and an average penetration depth of approximately 0.05 mm, an x-ray macrotexture of a sample with an average grain size of 25 μm will represent the orientation information of roughly 300,000 grains. This number is even higher by two orders of magnitude in the case of neutron diffraction, due to the much higher penetration depth to the order of 10 mm. In EBSD, despite the large number of orientation data that can nowadays be obtained by fully automated EBSD systems, the number of grains encountered is usually much smaller, which raises the question of the statistical relevance of the data with regard to the description of the orientation distribution of the volume of interest [59, 61- 62]. The success of using EBSD for overall texture estimation, therefore, depends on the ability to assess how many orientation measurements are required and an appropriate sampling schedule [59, 61].

3.8.2 Orientation and Misorientation Data Related to the Microstructure

The direct link provided between a sample’s orientation and microstructure is the most valuable aspect of microtexture. Reflection of the statistical orientation distribution of the sampled region(s) is usually only part of the total microtexture study. An orientation distribution is always derived from an orientation map or a selected subset of the map. The access EBSD provides to interfacial parameters, orientation relationships, and orientation

connectivity in the microstructure is another advantage of microtexture. This area gives rise to a further range of data processing and representation options [57-61].

3.9 Representation of Orientations in Pole Figure or Inverse Pole Figure

The most obvious method of representing a microtexture is in a pole figure. This is suitable since only a single graphic is required to represent the entire texture information. Local orientation data can be marked in the pole figure (or inverse pole figure) with different symbols or numbers with respect to their location in the microstructure, and the corresponding symbols/numbers are marked on a depiction of the microstructure [56, 58 -62].

3.10 Density Distributions (Pole figures and inverse pole figures)

It is useful to represent the density distribution from single grain orientation data as density levels in the pole figure whether to get more quantitative information on the relative density of microtexture data or to relieve a congestion of individual data points. By subdividing the pole figures into a grid with distinct angular cells, density distributions resulting from a given set of single orientations can readily be determined, for instance, $\Phi \times \psi = 5° \times 5°$. For each matrix orientation g between the sample and the crystal coordinate system, the pole figures have angles Φ_i and ψ_i for each pole $(h_i k_i l_i)$. For an inverse pole figure, the inverse orientation matrix g^{-1} is replaced by the orientation matrix g, and the vector $(h_i k_i l_i)$ is replaced by a vector $(X_S Y_S Z_S)$ of the sample coordinate system, for example, X_S = RD = (100), Y_S= TD = (010), Z_S = ND = (001) [57, 59]. The angles α and β now define the positions of the orientation matrix g in the inverse pole figure, after calculation of the angles Φ_i and ψ_i, the value of the corresponding cell (Φ_i, ψi) is incremented by one. In the end, the data are normalized with the total number of orientations M and the number of poles i. The data can then be plotted in a pole figure or inverse pole figure. A comparison of microtexture (Figure 3.9(b)) and macrotexture (Figure 3.9(c)) shows very good correspondence in the positions of the main peaks [58-64].

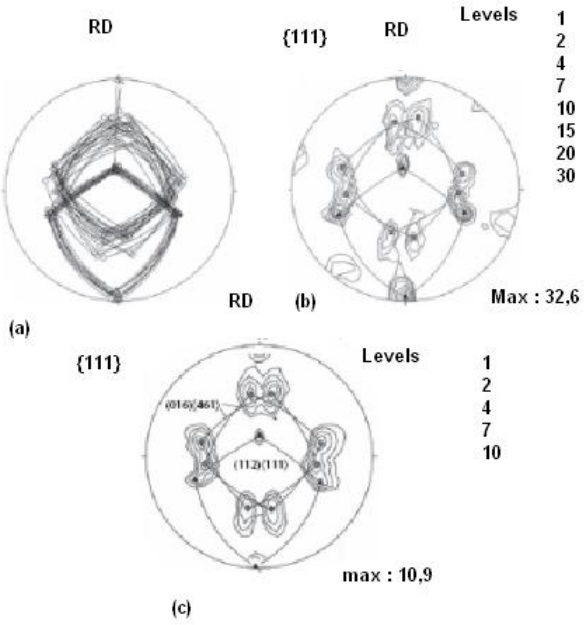

Figure 3.9: Comparison of EBSD microtexture and x-ray macrotexture pole figures EBSD single-grain orientation measurements in the as-deformed matrix and the new recrystallized grains; (b) continuous density distribution (c) x-ray macrotexture of the same sample [59].

A quantitative comparison of the orientation density, however, is not possible. This is evident from the different heights of the texture maximum intensities (32.6 in Figure 3.9(b) compared to 10.9 in Figure 3.9(c)). The intensity distribution difference is due to the different measuring procedures applied. X-ray pole figures are textures by volume [59, 61], which means that each orientation contributes to the texture according to its volume. By contrast, during the EBSD single grain orientation measurements, the orientation of large recrystallized grains is measured only once, yielding a texture by number. Comparatively to EBSD, in the x-ray texture the intensity of these large grains are underestimated. It might be appropriate to represent only the discrete data or to smooth the pole figure data by convolution of the intensity data in the pole figures with a suitable filter, see figure 3.10.

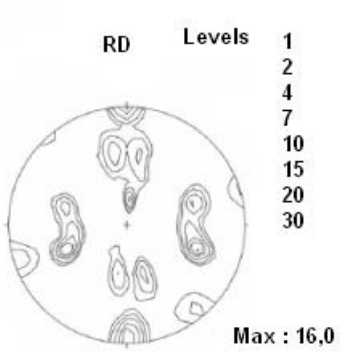

Figure 3.10: Smoothed pole figures derived from figure 3.9's pole figure data [59]

Figure 3-10 displays the pole figure of Figure 3.9 (c) after smoothing according to this process. Another way to derive continuous pole figures or inverse pole figures from single grain orientation data, is to calculate an ODF and then to recalculate the desired (inverse) pole figure. Provided the series expansion method is applied, the pole figure data will automatically be smoothed [59-63].

3.11 Statistical significance of Single-Grain Orientation Measurements

The number of grains encountered by the various techniques for single grain orientation measurements (EBSD) is still small compared to the number of grains contributing to x-ray or neutron pole figure measurements despite the relatively large number of orientation data obtained [59]. The number of single grain orientation measurements, which is necessary to represent the texture sufficiently, depends on crystal type, sample symmetry and most of all, on the texture's sharpness. It is stated that for the determination of an ODF with statistical relevance (i.e., statistical reliability of 80 %), approximately 25 points per cell must be considered [55-59]. For cubic crystal sample symmetry (i.e., ODF size 90° × 90° × 90°) and a cell size of 5°, this would require approximately 10,000 orientation measurements. It was reported in some recent studies that for cubic materials, the ODFs derived from only 100 orientations already comprise the main characteristics of the textures, whereas a statistically sound representation of the textures requires 500 – 1000 orientations (grains) [59]. Because of the strong influence of the texture sharpness on the accuracy of reproducing an ODF from single grain orientation measurements, it is necessary to develop a quantitative measurement for the minimum number of single grain

orientation measurements, which is required to represent adequately the texture of a given sample. To determine the minimum number of single grain orientation measurements necessary to reproduce appropriately the corresponding texture, ODFs are computed for an increasing number M of single grain orientation measurements [58-61].

3.12 Models on Ridging or Roping Found in Ferritic Stainless Steels

Various mechanisms to explain the ridging phenomenon in metals have been proposed. Chao's [64] model which was first to be proposed, is based on the differential strain accommodation of elongated parallel volumes of low R-value {001} <110> cube-on-face (CF) and high R-value {111} <112> cube-on-corner (CC) material. The model assumes that ridges represent differences in sheet thickness found within adjacent regions. Thus the ridges in these sheets result from through-thickness strain variations in the face of the cube, edge and corner texture components. The model, therefore, predicts the presence of a band-type distribution of texture components along the rolling direction whereby each band has a different resistance to thinning (i.e. the thickness strain). The validity of this model has been questioned, however, after it has been found that there are no measurable variations in the thickness strain in corrugated surface profiles but rather in ribbed profile. This clearly indicates that Chao's model is not quite applicable to explain ridging in ferritic stainless steels. Wright's [65] model which is a modification of Chao's model, was proposed so that the corrugated surface profile will be accounted for by duly considering a buckling mechanism. In this model, it is presumed that there are longitudinal bands of similarly oriented grains having a lower thinning resistance than the matrix under uniaxial tension in the RD (See figure 3.11 below).

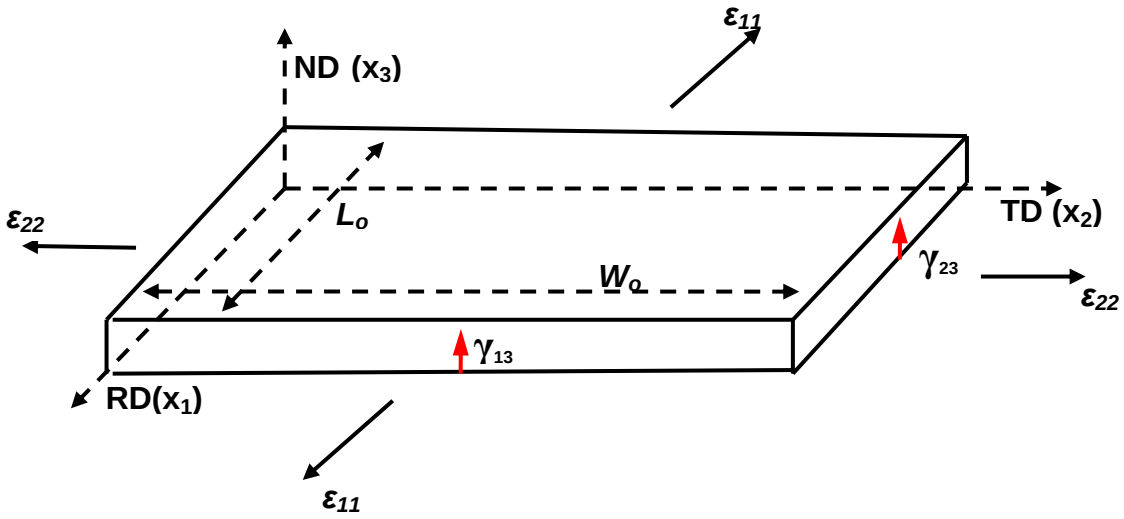

Figure 3.11: Schematic representation of a small region of a sheet and the coordinate system used [8].

Due to a low thinning resistance during loading, these bands mostly contract in the normal direction (ND) (ε_{33}) as against very little contraction in the ND by the surrounding matrix as compared to much more contraction in the transverse direction (TD) (ε_{22}) [66,67]. An incompatibility condition is, therefore, created at the band interface which generates a compressive stress (σ_{22}) across the band's width and the ultimate buckling of the band across its width that eventually leads to a series of localized buckling events which develops a corrugated surface profile [65, 68-71]. It has however been found that the Wright model is also not in full agreement with a detailed finite element study based on the crystal plasticity theory [65, 66, and 70]. What is clear about these two models is that both the Chao and Wright models, relate ridging to a banded distribution of texture components in the through–thickness direction.

Takechi et al's [69] model, which was developed independently at the same time as the first model, was built on the accommodation of shear strains γ_{23} developed by different components of a <011> fibre texture parallel to the rolling direction when the sheet is strained in the RD (as shown in Figure 3-11). This model has not been well recognised due to the fact that the necessary existence of a texture band with <011> parallel to the RD has not been well established [66, 69-71]. Nevertheless, the importance of the shear component is reliably correlated with some recent results [69, 72]. One common assumption, which all these three models use, is based on the fact that there are longitudinal bands in

which the bands are similarly oriented. These models give a good physical picture of ridging, but do not take interactions between adjacent grains into consideration. These interactions between grains should have been accounted for because when material deforms, the stress or strain of each grain is different from the macroscopic stress or strain, known as the Taylor factor. The operating slip systems therefore vary with the orientation of each grain [66-69].

3.13 Texture analysis in ferritic stainless steels

Many studies have been done whereby electron back scattering diffraction (EBSD) was used to show the local texture distribution in ferritic stainless steel sheets [67- 74]. It has been established in these studies that the spatial orientation distribution in the RD–ND and TD-ND sections (see Figure 3-11) exhibits inhomogeneity but no alignment. It was also shown in these studies that alignment of similarly oriented grains along the RD was found in the RD-TD plane. It was also established that the stronger the alignment, the more severe the ridging [65-67]. For this reason, it seems fitting to study ridging by analyzing the EBSD data measured in the RD-TD (or rolling plane) [66- 69]. Ridging or roping can be significantly reduced or completely removed by eliminating microstructural and textural banding which is the origin of anisotropic flow of mixed texture responsible for ridging in FSS [66, 69, and 75]. Major means by which textural and microstructural banding in commercial ferritic stainless steel sheets may be reduced or removed, includes modification of the alloy chemistry [66, 67, 69, 78], casting practice [69] and the thermomechanical processing [66, 69]. While the first method suggests elimination of the austenite phase during hot working, the second method proposes the enhancement of the equiaxed grain ratio during processing. The third one, however, makes use of faster recrystallization processes (i.e. both dynamic and static) to reduce the degree of banding. This dynamic recrystallization process is affected by the accompanying partial transformation during hot rolling of 16 wt% Cr ferritic stainless steel and, therefore, the hot rolling conditions during this processing stage [70-73].

3.14 Texture of Polycrystalline materials

Any material consisting of an assembly of individual grains of which a significant proportion of their orientations cluster to a certain degree in relation to some particular orientation in

relation to some selected reference frame, is perceived to have a preferred orientation or simply a given texture [73-76]. Almost all industrial metals have a polycrystalline aggregate. The exact nature of the texture is a complex function of the thermal treatments, mechanical deformation and the chemical composition or the alloy. Unique textures may arise during various metallurgical processing steps such as during solidification, deformation (wire drawing, cold or warm rolling, extrusion, forging etc), during recrystallization after cold work or even during the grain growth stage [76, 78]. Deformation texture has its origin in the crystallographic nature of the common deformation processes of slip and twinning while transformation textures have their origin in the orientation relationships between the parent and product phase of the transformation [74-76]. Typically these are confirmed in the Kurdjumov-Sachs relationship (111) γ // (110) $_{\alpha}$: [110] γ // [111] $_{\alpha}$ that relates the orientations of the ferrite (α) and austenite (γ) phases in stainless steel. These precise relationships ensure that where a texture existed originally, the phase transformation will necessarily create a new and different texture in the product structure [75-78].

In sheet metals, the texture can be specified by defining the crystallographic planes and directions with respect to a certain reference, such as the rolling direction. Forming operations such as forging, deep drawing etc., lead to the formation of inhomogeous textures. In cases such as these, the nature of the stress and the magnitude of the strain vary from point to point within the product and the texture is indescribable in a simple manner. In practice nearly all textures are inhomogeneous to some extent. In rolled sheets there is always a texture transition from the centre to the surface that is a consequence of the friction during rolling between the sheet surface and the rolls. The texture developed at the surface is a shear or reverse shear texture while that at the centre more closely reflects the plane strain condition that is typically used to describe rolling. The transition from one stage to another through the metal thickness follows the pattern of variation in the operating stress [77, 78]. The most important orientations and fibres found in stainless steels (ferritic and austenitic) after rolling are shown in Table 3-1.

Table 3-1: Important orientation fibres found in ferritic and austenitic stainless steels [83].

Material	Fibre name	Fibre axis	Components
BCC phase	a_{bcc}–fibre	<110> parallel to RD	{001}<110>, {112}<110>, {111}<110>
	g–fibre	<111> parallel to ND	{111}<110>, {111}<112>
	h–fibre	<001> parallel to RD	{001}<100>, {011}<100>
	z–fibre	<011> parallel to ND	{011}<100>, {011}<211>, {011}<111>, {011}<011>
	e–fibre	<011> parallel to TD	{001}<110>, {112}<111>, {4 4 11} <11 11 8>, {111}<112>, {11 11 8}<4 4 11>, {011}<100>
	q–fibre	<001> parallel to ND	{001}<100>, {001}<110>
	b_{bcc}– skeleton line	≈ <111> close to ND	{111}<110>, {557}<583>, {111}<112>
FCC phase	a_{fcc}–fibre	<011> parallel to ND	{011}<100>, {011}<211>, {011}<111>, {011}<011>
	b_{fcc}– skeleton line	less symmetric fiber following local texture maxima rather than fixed coordinates	{211}<111>, {123}<634>, {011}<211>

3.15 Hot band texture in stainless Steels

In the last few years, a complete picture on the evolution of hot rolling textures of BCC and FCC steels and related alloys has become available through the application of quantitative texture analysis in terms of the orientation distribution function (ODF) [82-84]. The main parameters leading to categorization of hot band steel textures can be grouped into four processes, Table 3-2 [82- 83].

Table 3-2: Main parameters which lead to different classes of hot band steel textures [83].

Main groups	Factors in each parameter group
Processing	• casting conditions (e.g. continuous, thick or thin slab) • slab treatment (temperature, soaking time) • rough or pre-rolling • hot rolling schedule (ferritic rolling, austenitic) • reduction schedule (macroscopic through-thickness strain rate profiles inter-pass times, strain per pass)
Thermodynamics	• amount and kind of alloying elements • impurities • stored deformation energy • transformation behavior • stacking fault energy (austenite)
Microstructure	• grain size and shape • recrystallization temperature and time • shear banding • precipitations
Crystallography	• active slip systems • inherited textures • orientation relationships during transformation (e.g. Bain or Nishiyama-Wassermann or Kurdjumov-Sachs)

During hot rolling, the parent austenite phase develops a deformation crystallographic texture, which is later inherited by the ferrite upon transformation. At relatively high temperatures of rolling, (i.e. above the DR_{TT} or austenite no-recrystallization temperature), a weak recrystallization texture is formed. The austenite in this case displays the cube {001} <100> texture, which transforms primarily into the rotated cube {001} <110> in the ferrite [81, 82, 83,]. If, on the other hand, the austenite is not able to recrystallize during or after rolling, it develops a sharper texture through DRV.

3.16 Texture and Properties of ferritic stainless steels

Many material properties are texture specific and this underscores the importance of texture to the engineering use of materials. With the full range of texture techniques now available, insights can be gained into material processing, corrosion, cracking, fatigue, grain boundary properties and other phenomena with a crystallographic component. It is reported that the direct impact of texture on a material's properties most of the time is between 20 % - 50 % [59, 68-71]. Properties of materials that are texture dependant include: Young's modulus, Poison's ratio, strength, ductility, drawability, toughness, magnetic permeability and electrical conductivity [59]. The texture mostly determines the plastic anisotropy of a metal which is of significance for practical applications such as deep drawing [59, 85]. Compared to plain carbon steels, annealed ferritic stainless steels present a yield point followed by a stress drop on the stress/strain curves. Breakaway pinned dislocations which enable a "true yield stress" to be defined are responsible for this behaviour. It then leads to the formation of localized deformation bands known as "Piobert-Lüders" bands. Consequently, surface effects may be observed after plastic deformation [67, 73-75]. In the case of deep drawing, they are called "stretcher strains" or "worms". This can be partially avoided by stabilisation or by a skin pass operation which introduce "fresh" dislocations into the structure. There is evidence of non-uniform texture in ferritic stainless steels which leads to heterogeneous mechanical behaviour. Earing as well as ridging is then observed. Ridging (see Figure 3.12) which occurs during deep drawing, involves the formation of small undulations elongated in the tensile direction.

Figure 3.12: Deep drawn cup of AISI 430 grade showing the "ridging" phenomenon [73]

These defects can be eliminated during polishing but at extra costs to the production. Stabilized ferritic stainless steels are less sensitive to ridging than the basic AISI 430

grade. In practice, optimization of thermomechanical conditions makes it possible to significantly ease this phenomenon in AISI 430. Most 16-18 wt% Cr ferritic grades' corrosion resistance is mainly linked to the alloy's chemistry while their mechanical properties such as drawability may be improved by appropriate thermomechanical process conditions [71-75].

3.17 Texture and anisotropy in AISI 430 and AISI 433

Dislocations in ferritic stainless steels tend not to dissociate as dislocations in FCC structures do [85]. This lack of dissociation encourages cross slip [86]. In deformed ferritic stainless steels, certain crystallographic slip systems predominate. Large deformations mechanically cause individual grains into closer crystallographic alignment through rotation. This preferred deformation along easier slip planes results macroscopically in overall mechanical properties that vary with direction with respect to the prior deformation. This indicates that pronounced mechanical anisotropy is found in ferritic stainless steel which is revealed in their deep drawing characteristics. AISI 430 and AISI 433 ferritic stainless steels do contract in their width directions while keeping virtually the same thickness when elongated. Thus AISI 430 and AISI 433 do resist thinning during deep drawing [87-91]. The Lankford ratio expressed in equation 3.14 is used to measure anisotropy in ferritic stainless steels.

$$R_m = \frac{r_0 + 2r_{45} + r_{90}}{4} \qquad (3.14)$$

where the subscripts 0, 45, and 90 refer to inclinations in degrees of the longitudinal axes of tensile test pieces to the rolling direction, transverse direction, and the normal direction of the sheet respectively. The individual R_m-value (mean r-value) is the ratio of width strain to thickness strain, as measured in a simple tensile test. An increase in drawability is found with an increase in the R_m - value as measured by the limiting drawing ratio (LDR) defined by the largest blank D_o that can be drawn through a die with a punch of diameter D_p without tearing as express in equation 3.15 [66]

$$LDR \approx {D_o}/{D_p} = \exp\ \eta \qquad (3.15)$$

where η is an efficiency term which allows for frictional losses. Most ferritic stainless steel sheets have a LDR of about 2.2 [81-83]. The major setback of the good formability of AISI

430 and AISI 433, however, is the ridging phenomenon associated with these steels. Most ferritic stainless steels carry some inherited preferred grain orientation that comes from the initial solidification when growth of dendrites is along preferred crystallographic directions. Hot rolling reorients these similarly oriented grains [86-88]. There is no full recrystallization and randomness of grain orientation in AISI 430 and 433 because there is no phase transformation or only a limited phase change or not enough stored energy during their hot rolling (deformation) to initiate full DRX.

3.18 The R-value and texture in ferritic stainless steel

Drawability of a material determines to a large extent the ability of sheets of a material to attain a high degree of plastic flow in the plane of the sheet while giving enough resistance to the flow in the thickness direction [88-90]. It has been demonstrated that high normal anisotropies or R_m - values are displayed by materials having a high proportion of grains oriented with their {111} planes parallel to the normal direction ({111}//ND) of the sheet. This type of texture is described as gamma (γ) fibre texture [89, 90]. On the other hand material which exhibits a texture component with the {110} planes parallel to the rolling direction ({110}//RD) are said to have a low R_m-value. This type of texture is described as alpha (α) fibre and it is found that such textures in materials are detrimental to their drawability. It is reported that by careful choice and control of hot rolling parameters a more prominent gamma fibre texture can be obtained from the hot rolling which will be inherited on cold rolling and annealing and will appear finally in the finished product.

3.19 Inherited texture from austenite transformation

Due to accumulation of sufficient strain in the austenite phase during hot rolling, a sharp rolling texture is obtained [87-89] which is usually inherited by the transformed product. Hot rolling of AISI 430 and AISI 433 at relatively high temperatures leads to formation of a recrystallization texture consisting mainly of {001}<110> and {110}<110>. These are derived from rotated cube components {100} <001>. The retained {100}<001> in the final product has detrimental effects on the drawability and earing which leads to sub-optimal behavior of ferritic stainless steels [87-90] and this must be avoided. Hot rolling parameters must therefore be carefully chosen to minimize the formation of these rotated cube

components since they transform into the {100}<011> texture if retained after cold rolling and annealing, which is detrimental to achieving good drawability. Table 3-3 shows major transformation texture components and their related orientations.

Table 3-3 Major transformation texture components and their related orientations [85]

Texture components	Source	Δr	R_m
{100}<011>	T	-0.8	0.4
{113}<110>	T	-1.7	1.0
{332}<113>	T	1.9	2.7
{112}<110>	R	-2.7	2.1
{223}<113>	R	-2.0	2.5
{554}<225>	A	1.1	2.6
{111}<112>	A	0.0	2.6
{111}<123>	A	0.1	2.4
{111}<110>	A	0.0	2.6

NB: T = Transformation texture, R= Recrystallization texture, A = Annealing texture

Δr = change in the R- value, R_m = Mean R- value

By maximizing the gamma fibre texture components such as {554} <225>, {111} <112>, and {111} <123> during hot rolling, ridging will be greatly minimized in AISI 430 and AISI 433 steels [87-90].

3.20 Deformation texture

During deformation of a metal, its grains are reoriented with a certain orientation being the preferred orientation over others. The observed preferred orientation or texture from hot rolling, is influenced by factors such as strain rate, the type of deformation, amount of deformation, temperature of deformation, the mechanism of slip in the metal and the inter-pass time [79,89,90]. The unique deformation textures generally observed after hot rolling and heavy cold work reductions of more than 50 %, are pre-dominantly of a fibre-like texture {001}<110>, although other texture components are usually also present. The following crystal rotations occur in polycrystalline materials along the following paths during the processing stages:

I. {001}<100> → {001}<110> → {112}<110> → {223}<110>

II. {110}<001> → {554}<225> → {111}<112> → {223}<110>

The preferred orientation resulting from deformation is strongly dependent on the slip and twinning systems available for deformation [87-89]. The formation of strong preferred orientation results in anisotropic properties of the stainless steel. Figure 3.13 shows some major deformation, transformation and recrystallization textures found in ferritic stainless steels.

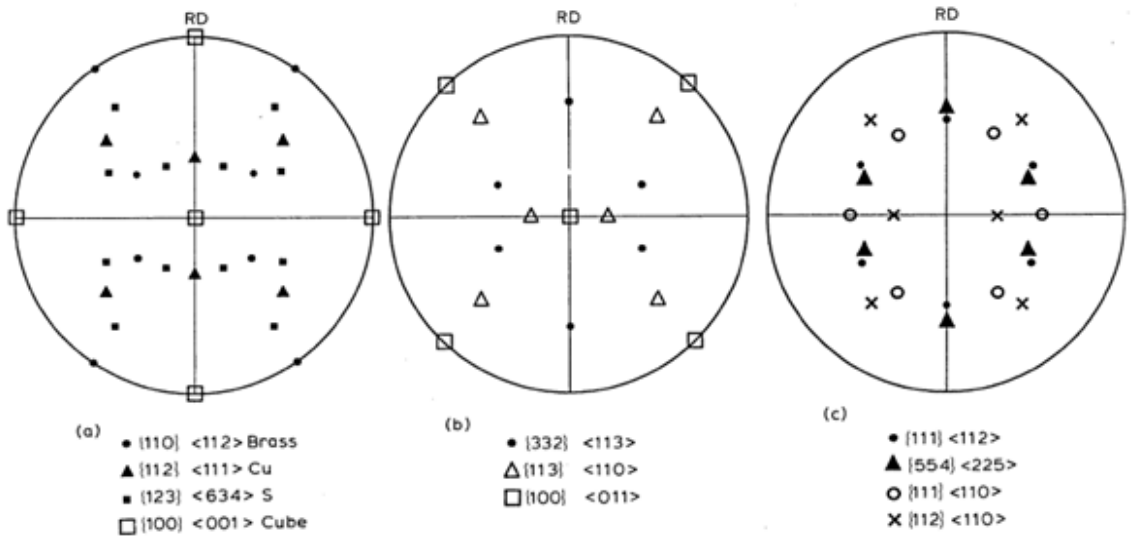

Figure 3.13 : Major texture changes during processing. (a) Major deformation and recrystallization texture component in the austenitic phase (b) major transformation texture component in the ferritic phase (c) some important orientations in transformed ferrite [92]

3.21 Annealing texture

The microstructure of ferritic stainless steels undergoes a sequence of changes during annealing, comprised of recovery, recrystallization and grain growth. There is no significant change in the texture of these stainless steels during recovery [92]. Recrystallization of the deformed steel, however, usually occurs by formation of new undeformed grains and their subsequent growth into the deformed matrix by the Strain Induced Boundary Migration (SIBM) mechanism. In austenitic materials with a low stacking fault energy, new orientations due to twinning occurs during recrystallization whereas in high stacking fault materials, twinning is not common during recrystallization. Recrystallization is generally responsible for a change in the distribution of the

crystallographic orientation of the grains and consequently in the crystallographic texture of the materials. Many industrial materials including AISI 430 and AISI 433, receive their final forming operation in an annealed condition. Thus the understanding of recrystallization texture is very important in material processing to achieve the desired results. The formation of annealing texture in ferritic stainless steels depends on a number of processing parameters, consisting of the amount and type of deformation preceding annealing, the composition of the alloy, grain size, annealing temperature and time as well as the inherited hot rolling texture [87-89].

Two theories which explain the occurrence of recrystallization texture in materials are the *orientation growth theory* and the *orientation nucleation theory* of recrystallization texture.

- The *orientation growth theory* of recrystallization states that the formation of nuclei with much the same orientation is possible but the grain growth rate of any given nucleus depends on the orientation difference between the matrix and growing crystal. The implication of this is that the recrystallization texture will be formed from those nuclei that have the highest growth rate in the cold rolled condition. This may be expressed mathematically by equation 3.16a

$$\frac{G_T}{G_R} = \beta = \frac{d^3{}_T}{d^3{}_R} \qquad \text{.....(3.16a)}$$

  where G_T is the growth rate of nuclei with a given texture orientation and G_R is the growth rate of nuclei with a random orientation. Whereas â<<1 indicates the absence of preferred orientation â>>1 indicates a preferred orientation that will develop out of a large number of nuclei with a particular texture orientation.
- *Orientation nucleation theory* of recrystallization texture presumes that grain boundaries or special grains act as preferred sites for nucleation. Mathematically, this may be expressed by equation 3.16b

$$\frac{N_T}{N_R} = \alpha \qquad \text{.....(3.16b)}$$

  where N_T is the number of recrystallization nuclei with a preferred orientation and N_R is the number of nuclei with a random orientation. Where á << 1, no preferred texture is observed and where á >> 1, a preferred texture will develop out of the larger number of nuclei with a particular texture orientation.

Ferritic stainless steels exhibit recrystallization textures of the elongated fibrous grains which appear to be of overriding importance in obtaining good drawability properties [88-91]. It appears in particular that a γ-fibre texture of <111> // ND influences positively on drawability of the stainless steels although α-fibre texture of <110> // RD is usually also present in significant quantities and may have a harmful effect on the drawability and subsequently the ridging.

3.22 Texture of ferritic stainless steel and ridging

It has been found that the lower plastic strain ratio of the {001} <110>colonies and difference in shear deformation between the {111} <110> and {112} <110> colonies results in ridging [87, 89, 90]. The development of recrystallization texture in ferritic stainless steel and its relationship to formability as well as the relationship between the limiting drawing ratio (LDR), the R-value and texture parameter involves the ratio of the {111}:{100} component in the texture [86-92]. Both the R-value and the LDR increases as the intensity of the {111} structural component parallel to the normal plane increases, indicating the beneficial effect of a strong {111} component in deep drawing or elimination or minimization of ridging. [87-89]. Therefore it is necessary to reduce or minimise the {100} texture and maximise the {111} texture to obtain high R_m-values as depicted in figure 3.14.

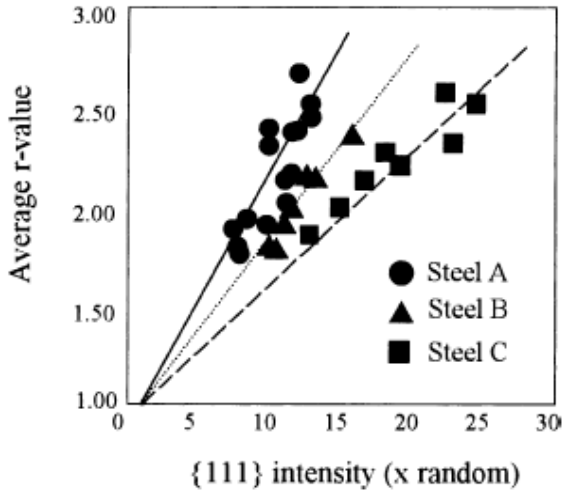

Figure 3.14 : A plot of R_m – value as a function of {111} plane intensities for AISI 409 ferritic stainless steel [87].

It is therefore generally proven that the gamma fibre texture is more beneficial in minimising ridging than an alpha fibre texture. In view of this it is essential to optimize the hot rolling conditions that will improve the gamma fibre texture present in AISI 430 and AISI 433 steels in order to eliminate or reduce ridging in these steels. This is, therefore, the main objective of this study, which is to promote the occurrence of dynamic recrystallization in order to obtain a desired γ-fibre texture in these steel grades through optimization of the hot rolling conditions.

4 CHAPTER 4: EXPERIMENTAL PROCEDURE

4.1 Mill Log Calculations

The industrial mill log provided by Columbus Stainless Steels gave useful information in predicting the metallurgical processes such as dynamic recrystallization or dynamic recovery during the hot rolling process which affects the characteristics of the steels.

4.1.1 The Mean Flow Stress

A plot of the calculated Mean Flow Stresses as a function of the deformation temperature per pass provides two regions with different slopes which distinguishes the softening mechanisms occurring in the steel (occurrence of DRX from DRV) during the hot rolling process. The mean flow stress which is actually the average of the flow stress during the hot rolling was calculated using the Sims equation [36], (see equation 4.1 below). The Mean Flow Stress per pass was calculated from mill load data obtained from the mill logs.

$$\bar{\sigma} = \frac{\sqrt{3}}{2}\frac{P}{WQ\sqrt{R'(\Delta h)}} \tag{4.1}$$

where

W = width of strip in mm,

Q = geometric flow stress factor which is dimensionless,

R`= flattened work roll radius in mm,

h_i = initial or input gauge in mm,

h_f = final or output gauge in mm,

P = roll force in Newton

For the full details of the equations used in the mill log analysis see appendix C.

4.1.2 Strain

Two strains that were considered in these calculations were effective nominal strain ε_n and the redundant strain ε_r.

$$\varepsilon_n = \frac{2}{\sqrt{3}}\ln\left[\frac{h_f}{h_i}\right] \tag{4.2}$$

$$\varepsilon_r = \frac{\Delta h}{4\sqrt{4R'^2 \sin^2 \alpha/2 - \frac{\Delta h^2}{4}}} \quad (4.3)$$

where α = arc cos [1-{Δh / 2R'}]

The total strain per pass was therefore accounted for by the summation of these two (nominal and redundant). Thus,

$$\varepsilon = \varepsilon_n + \varepsilon_r \quad (4.4)$$

4.1.3 Strain Rate

The average strain rate was calculated using the relation,

$$\dot{\varepsilon} = \frac{\varepsilon}{t} \quad (4.5)$$

where t is the time, given by:

$$t = \alpha / \left(\frac{2\pi U}{60} \right) \quad (4.6)$$

with U = angular speed in rpm and α being the contact angle in radians.

The calculated strain rate was found to be increasing with increasing number of deformation passes.

4.1.4 Inter-pass Time

The time between passes which denotes the restoration time between consecutive deformations was determined by taking the mean roll time of the consecutive passes and reverse time plus about 5 s added for adjustment of the roll gap. Thus, the time represents only the central point along the length of the coil whereby the head which enters this section will have a shorter inter-pass time and the tail which leaves this section last having a longer inter-pass time before entering the Steckel mill but on the reverse pass the situation reverses itself with the former tail now becoming the head and the former head now becoming the tail. This points to somewhat of a dilemma in the Steckel mill should it be found that the inter-pass time affects the resulting texture as different textures may then occur along the length of the coil.

4.1.5 Temperature

The entry and exit temperature during the seven pass schedule on the Steckel mill was determined from the mill log. This helped to identify the phases of the steel during the deformation stages and subsequently used in designing the simulation of the rolling mill.

4.2 The use of Thermo-calc® Software to determine the phases in the steels

The modelling of the phase transformations in AISI 430 and AISI 433 ferritic stainless steels during hot rolling requires knowledge of thermodynamic and kinetic parameters for a variety of possible phases. To obtain these parameters the computer package Thermo-calc® version 5 (TCFE6 database) [93, 94] thermodynamic software was used to make these calculations. The powerful and flexible nature of the Thermo-calc® software package allowed various thermodynamic equilibrium and phase diagram calculations to be done through minimising of the total Gibbs free energy of the system specified. The software package which is specifically designed for systems and phases that exhibit highly non-ideal behaviour made it possible to determine complex phases in AISI 430 and AISI 433 due to their many alloying elements [94] through an accurate and validated database. This database involving these steels was the TCFE6 TCS steels/Fe-alloys database which covers a complete and critical assessment of binary and even ternary systems as well as iron rich corners of higher order systems. The recommended temperature range for TCFE6 within which the calculations were done was between 700 ^{o}C to 2000 ^{o}C. Table 4-1 shows the phase identifications used in the database. The symbol # is being used to denote different composition sets of the same phase.

Table 4-1 The Phase identifications used in the TCFE6 steel/ Fe-alloy [94]

Phase	Database
Austenite	FCC_A1#1
Ferrite	BCC_A2
M(C,Al)	FCC_A1#2

These calculations assisted in the design of the hot rolling schedule for the studies covered by this study. Thermocalc was also used to calculate the Ac_1 temperatures of AISI

430 and AISI 433. These calculations and the phase transformations were validated on the Baehr dilatometer. Within the temperature range of 800 ^{o}C to 1200 ^{o}C, used in the Thermocalc calculations (which addresses only equilibrium phases), no delta ferrite nor a mixed ferrite/martensite structure is predicted in any of the steels used for the studies but depending on the heating and quenching rates that will be used during the thermomechanical simulation on the Gleeble, non-equilibrium conditions will exist and delta ferrite or ferrite/martensite could be retained in the final ferrite structure.

4.3 Experimental Materials

AISI 430 and AISI 433 are plain chromium non-stabilized standard ferritic stainless steels. The chemical compositions of the steels used for the studies are specified in wt % in Table 4-2. The basic difference between the two materials used in this study is the content of aluminium (Al). The AISI 430 contains 0.008 wt% Al and AISI 433 contains 0.172 wt% Al [10]. These steels are dual phase during hot rolling within a temperature range of 850 to 1000 ^{o}C, and this was confirmed by the Thermo-calc® software used to model the rolling process.

Table 4-2: Compositions of AISI 430 and AISI 433 used for the study [10].

Type	%C	%Si	%Mn	%Co	%P	%S	%Cr	Ti	%Al
430	0.050	0.39	0.60	0.03	0.019	0.0005	16.20	0.001	0.008
433	0.046	0.40	0.49	0.02	0.021	0.0005	16.18	0.005	0.172
Type	**%V**	**%Ni**	**%Cu**	**%Mo**	**%Nb**	**%O**	**%Sn**	**N**	**%B**
430	0.12	0.23	0.08	0.025	0.001	0.0080	0.005	0.0465	0.0005
433	0.12	0.15	0.08	0.010	0.001	0.0043	0.006	0.0352	0.0005

4.4 Characterisation of the as received samples' texture

In order to determine the stage of processing where the texture changes, textures of as received products from the roughing mill (30 mm thickness, also called the Transfer Bar) and product from the Steckel mill (down to 3 mm thickness, also called Hot Band) as well

as their final (finished) products after cold rolling and annealing were determined by both XRD and EBSD techniques of texture measurements. A change in texture was found between the transfer bar and the Hot Band (see chapter 5) and therefore, it was concluded that the change in texture on the Steckel mill indicates that, there is some form of dynamic recrystallisation (DRX) taking place during the Steckel mill hot rolling [45]. This assisted in choosing the schedule of the hot rolling stage where the parameters need to be optimised to obtain a desired texture in the steel.

4.5 Hot Compression Test Procedure

Machined cylindrical specimens for the compression tests on the two Gleeble simulators were 10 mm in diameter and 15 mm in length. A practical limit of initial diameter (D_o) to initial height (h_o) (i.e. D_o/h_o) of 0.66 was chosen to minimize the barrelling (non-uniform deformation) and ensure that no buckling occurred [35, 37]. To decrease the friction and allow uniform deformation, that is to prevent or minimize barrelling, thin tantalum sheets were placed between the compression specimen and the isothermal sintered tungsten carbide anvils. The single hit tests were performed to determine the occurrence of DRV and DRX while multi-pass tests were carried out to simulate the Steckel mill hot rolling process.

4.5.1 The single hit compression test

Single hit compression tests were carried out on the Gleeble-1500D® and Gleeble-3800™ thermomechanical simulators with a pass strain of 0.92 at strain rates of $0.1s^{-1}$ -5 s^{-1} (on Gleeble-1500D®) and 25 s^{-1} and 50 s^{-1} (on Gleeble-3800™). The samples were heated to 1150 ^oC at a rate of 10 ^oC s^{-1} and soaked for 5 mins to ensure elimination of thermal gradients. It was then cooled to 1100 ^oC at 10 ^oC s^{-1} where a single hit compression was applied. Oxidation of the specimens during testing was prevented by passing a continuous flow of high-purity argon through the system in the case of the Gleeble-1500D® and vacuum in the case of the Gleeble-3800™. The as-deformed specimens were immediately helium quenched to 100 ^oC and then air cooled to room temperature. A friction coefficient of 0.2 [35] was used as a correction factor in calculating the Von Mises flow stress. The equations used for the flow stress calculations were as follows:

$$\sigma_o = \frac{0.0625 P_x \mu^2 h_x^{-2}}{e^{\mu\sqrt{d_i^2 h_i / h_x}\,/h_x} - \mu\sqrt{d_i^2\, h_i / h_x}\,/h_x - 1} \tag{4.7a}$$

$$\sigma_o = -0.0981 P_x \frac{\Delta h + h_i}{h_i d_i^2 \;\; \pi/4} \tag{4.7b}$$

where: P_x is the Gleeble force, h_x is the Gleeble stroke, h_i is the initial height of the specimen, d_i is the initial diameter of the specimen and σ_o is the calculated flow stress. The subscript *x* stands for an instantaneous value and $\Delta h = h_x - h_i$, which makes it negative at all times. Equation [4.7a] was used when friction was considered and it is derived from the Von Mises stress analysis for plastic flow while equation (4.7b) was used when no friction was considered [35]. As for the Von Mises strain, the following equation; based on the Von Mises yielding criteria was used:

$$\varepsilon = \frac{2}{\sqrt{3}} \ln\left(\frac{h_x}{h_i}\right) \tag{4.8}$$

where the $2/\sqrt{3}$ is the Von Mises correction for plane strain compression.

4.5.2 The multi-pass compression test

Multi-pass hot compression tests were performed on both of the Gleeble thermo-mechanical simulators with pass strains ranging from 0.11 to 0.15 together with strain rates from 0.1 s^{-1} to 5 s^{-1} on the Gleeble-1500D® and 25 s^{-1} and 50 S^{-1} on the Gleeble-3800™ and inter-pass times of 2, 10, 20 and 30 seconds.

The samples were heated to 1150 ^oC at a rate of 10 $^oC/s$ and homogenized for 5 minutes to eliminate thermal gradients, then cooled to the selected deformation temperature at 10 $^oC/s$ where multi-step compression was applied. Figure 4.1 shows the deformation process of samples in the Gleeble-3800™.

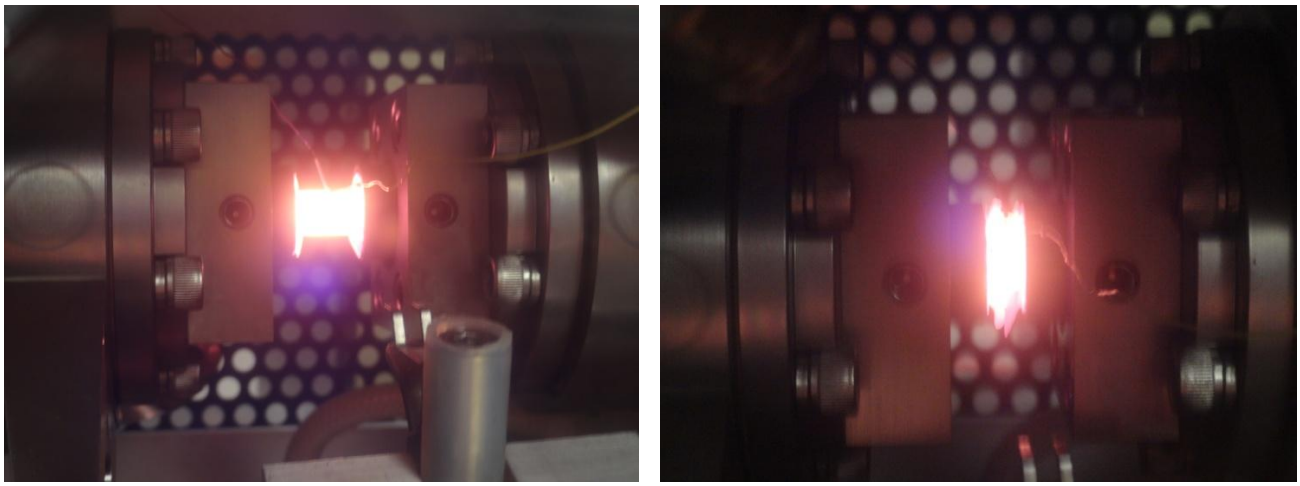

a b

Figure 4.1**:** Deformation of AISI 430 sample in the Gleeble 3800^{TM} at strain rate of 50 s (a) holding at 11500 ^{o}C for homogenization (b) after compression from 15 mm to 6 mm

The multi-pass testing schedule and plan used are illustrated schematically in Figure 4.2 and Table 4-3 respectively. In addition, in order to be as close as possible to the industrial process and for validation purposes, multi-pass plane strain condition hot rolling tests were also carried out on a laboratory hot rolling mill at a high strain rate close to 50 s^{-1} to simulate the industrial Steckel mill hot rolling process using the same strain per pass and inter-pass time employed in the Gleeble tests

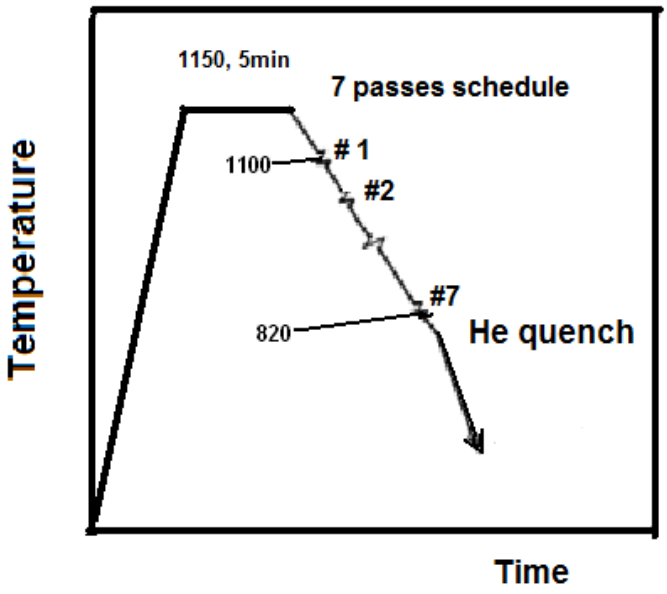

Figure 4.2: Schematic representation of the schedule employed in the Gleeble hot compression tests.

Seven compression passes were applied in each test and the temperature was decreased by 30 ^{o}C between passes. The maximum height reduction of all the specimens was kept at 40 %. This ensured that the maximum barrelling factor was kept below 0.9 in all the tests**.**

Table 4-3: Experimental schedule for simulating the Steckel mill hot rolling process. RT= reheat temperature, P = Rolling pass.

Simulation of Steckel mill's hot rolling on the Gleeble 1500D® and 3800™								
Sample size: length 15 mm; diameter 10 mm								
RT to 1150 °C at 10 °C/s, homogenize at 1150 °C for 5 mins before lowering the temperature at 10 °C/s to the entry temperature of the first pass								
Parameters	**Units**	**P1**	**P2**	**P3**	**P4**	**P5**	**P6**	**P7**
Initial height H	(mm)	15.00	13.00	11.20	9.80	8.60	7.20	6.80
Final Height H		13.00	11.20	9.80	8.60	7.20	6.80	6.00
Strain per pass		0.14	0.15	0.13	0.13	0.13	0.11	0.13
Deformation Temperatures	(^{o}C)	1100	1070	1040	1010	980	950	920
		1030	1000	970	940	910	880	850
		1000	970	940	910	880	850	820
Strain rates	(s^{-1})	0.1	0.1	0.1	0.1	0.1	0.1	0.1
		0.5	0.5	0.5	0.5	0.5	0.5	0.5
		1.0	1.0	1.0	1.0	1.0	1.0	1.0
		2.0	2.0	2.0	2.0	2.0	2.0	2.0
		3.0	3.0	3.0	3.0	3.0	3.0	3.0
		4.0	4.0	4.0	4.0	4.0	4.0	4.0
		5.0	5.0	5.0	5.0	5.0	5.0	5.0
		25	25	25	25	25	25	25
		50	50	50	50	50	50	50
Inter-pass time at the end of pass	(s)	2	2	2	2	2	2	NA
		10	10	10	10	10	10	NA
		20	20	20	20	20	20	NA
		30	30	30	30	30	30	NA
Quenching	Immediately after last pass quench in Helium down to 100°C, and air cool to room temperature							

4.5.3 Plane strain test

Rectangular samples of dimensions 150 mm in length, 60 mm width and thickness of 15 mm were machined out of the transfer bars of both steels and used for this test. Multi-pass hot rolling tests were carried out on a laboratory hot rolling mill, see Figure .4-3. Pass strains ranging from 0.11 to 0.15 at a strain rate of 50 s^{-1} (similar to the Steckel mill) and inter-pass times of 30 seconds used. The samples were heated in a furnace to 1150 ^{o}C and homogenized for 5 minutes to eliminate thermal gradients. The sample was then cooled to the selected deformation temperature as monitored by an optical pyrometer where after multiple pass compression was applied. The sample was immediately air quenched after the final compression.

Figure 4.3 : AISI 430 sample being hot rolled under Plane strain condition at a high strain rate of 50 s^{-1} temperature of 1100 ^{o}C on a laboratory hot rolling mill

4.5.4 Cold rolling and Isothermal Annealing

The plane strain samples were cold worked using a laboratory cold rolling machine. The percentage reductions were 80 % and 66 %. The cold rolling was done in small reductions of 5 % per pass in order to achieve a final uniformly deformed structure. The isothermal annealing was carried out at two different annealing temperatures of 750 ^{o}C and 780 ^{o}C. After annealing, the samples were immediately quenched in a water bath.

4.6 Tensile Test

From each sheet of plate (hot band and the final annealed samples), tensile test samples were machined from three different directions i.e 0^o to the rolling direction, 45^o to the rolling direction and 90^o to the rolling direction. Tensile tests were performed at a cross-head speed of 5 mm/min at room temperature using standard specimens prepared in accordance with the ASTM E8* standard. The specifications and detailed measurements of the specimen are shown in Figure 4.4 and Table 4-4 respectively.

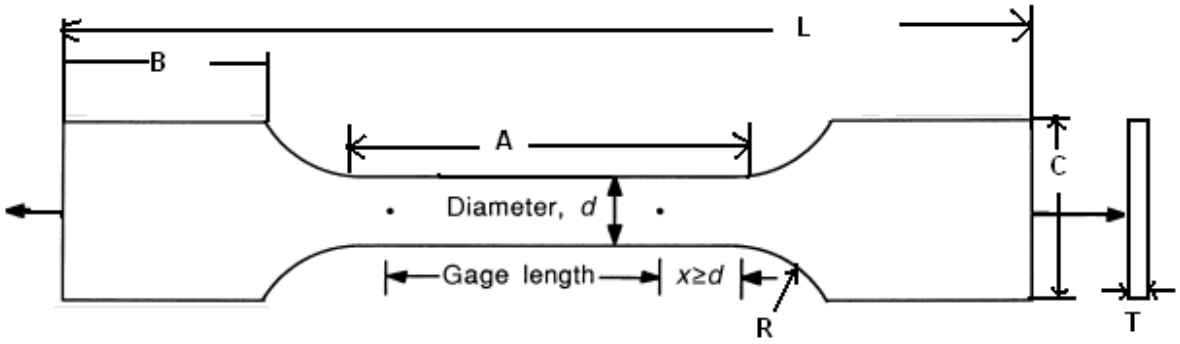

Figure 4.4 : Schematic diagram of the tensile test specimen, showing a reduced gage section and enlarged shoulders.

Table 4-4: The actual dimensions for the subsize tensile specimen

Symbol	Parameter name	Dimensions (mm)
A	Length of reduced section	32
B	Length of grip section	32
C	Width of grip section	10
D	Width	6
G	Gage length	25
L	Overall length	100
R	Radius of fillet	6
T	Thickness	5

The Lankford value (r-value) was calculated by measuring the widths at these three different points of the tensile specimen measured at 15 % strain. The mean r value, R_m was calculated by the following equation, $R_m = \frac{r_0 + 2r_{45} + r_{90}}{4}$ (4.9)

Here, r_0, r_{45} and r_{90} correspond to the r-values in the directions of 0^o, 45^o, and 90^o to the rolling direction respectively.

4.7 Metallographic analysis

The two different microscopy techniques employed were optical and SEM or scanning electron microscopy, the latter equipped with EDS facilities. This micro analysis technique was used to characterise the microstructure of the ferritic stainless steels for the purposes of identifying the structure of these steels and study the occurrence of dynamic recrystallization and dynamic recovery that takes place during the processing of the steels. Products from all the stages of processing ranging from the roughing mill product (30 mm in thickness) to the finished cold rolled and annealed product (0.8 mm thickness) as well as the simulated samples were analysed. The combination of these different techniques made it possible to gain a reasonable understanding of the microstructural development of the steels. The Gleeble deformed specimens were cut symmetrically into two parts parallel to the compression axis. EBSD scans showed that only the central regions of the deformed specimen were well recrystallized. These central regions of the specimens where they had the largest deformation were, therefore, chosen as the investigation area of interest.

4.7.1 Optical Microscopy

In order to assess the evolution of the microstructure as well as the effect of hot rolling conditions on the AISI 430 and AISI 433 stainless steels microstructure, both industrially hot rolled samples and simulated samples were optically observed under a conventional optical microscope. The samples were mounted in a plastic resin, adequately ground and mechanically polished to a 1 µm diamond finish. The samples were then etched with Ralph's reagent (50 ml H_2O, 50 ml ethanol, 50 ml methanol, 50 ml HCl, 2.5 ml HNO_3, 3.5 g $FeCl_3$ and 1.0 g $CuCl_2$) by swabbing for 20 seconds and observed in an Olympus BX51M microscope.

4.7.2 Electron microscopy

In order to identify the structure and assess the occurrence of DRX and DRV through microstructural analysis, industrially hot rolled samples as well as simulated samples were observed in a scanning electron microscope. The samples were prepared as above and were then observed in a Joel JSM 6300 scanning electron microscope.

4.8 EBSD Texture measurement sample preparation

A systematic range of orientation distribution functions (ODFs), from electron back scattered diffraction (EBSD) determined across the sectioned specimen showed the clearest recrystallization texture in the central areas. The samples were mounted in a plastic resin, adequately ground and mechanically polished to a 3 μm diamond finish. This was done to ensure that the surface finish was suitable for diffraction [59]. The samples were then removed from the resin and electro-polished at 0.2 A and 20 V for 20 s in 95 % ethanol and 5 % perchloric acid to remove the mechanically disturbed layer.

4.9 XRD Sample Preparation

The samples were mounted in a plastic resin, adequately ground and mechanically polished to a 3 μm diamond finish to ensure that the surface finish was suitable for diffraction [59]. The rolling direction of each sample was identified and used as a point of reference in the texture measurement in the goniometer.

4.10 Determination of DRX to DRV Transition Temperature (DR_{TT})

The force-stroke curves obtained from the compression tests were converted into true stress-true strain curves through equations 4.7a and 4.7b described earlier. For full details of the template used of the analysis see Appendix B. [35]. A plot of the obtained true stress as a function of the true strain is shown in Figure 4.5 below.

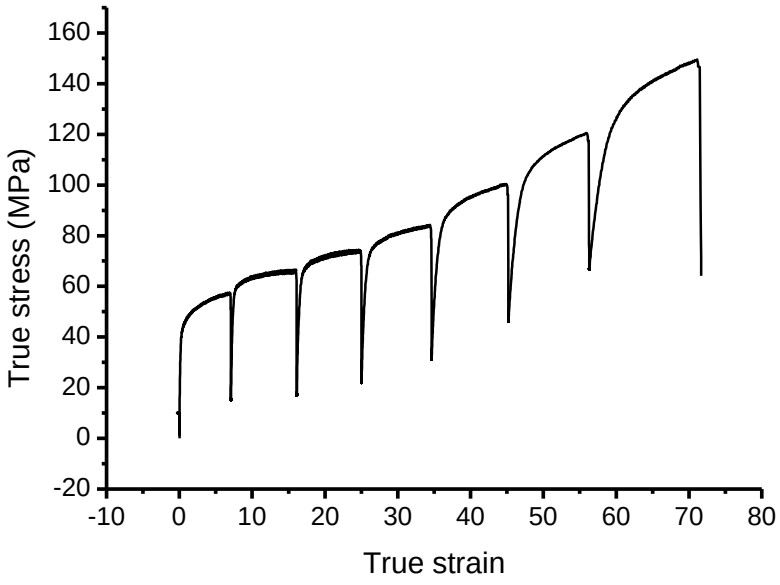

Figure 4.5: True stress–strain curves for an AISI 430 stainless steel deformed at a strain rate of 1 s^{-1} using a 7 pass schedule, starting at 1100 ^{o}C and ending at 920 ^{o}C. The inter-pass time in this instance was kept constant at 20 s

The mean flow stress (MFS) per pass was calculated from the flow curves (Figure 4-5) by using the equation:

$$MFS = \frac{1}{\varepsilon_b - \varepsilon_a} \int_{\varepsilon_a}^{\varepsilon_b} \sigma \, d\varepsilon \qquad (4.10)$$

where ε_a is the initial strain, ε_b is the final strain and σ is the Von Mises stress. A typical dependence of mean flow stress on the deformation temperature is shown in Figure 4.6.

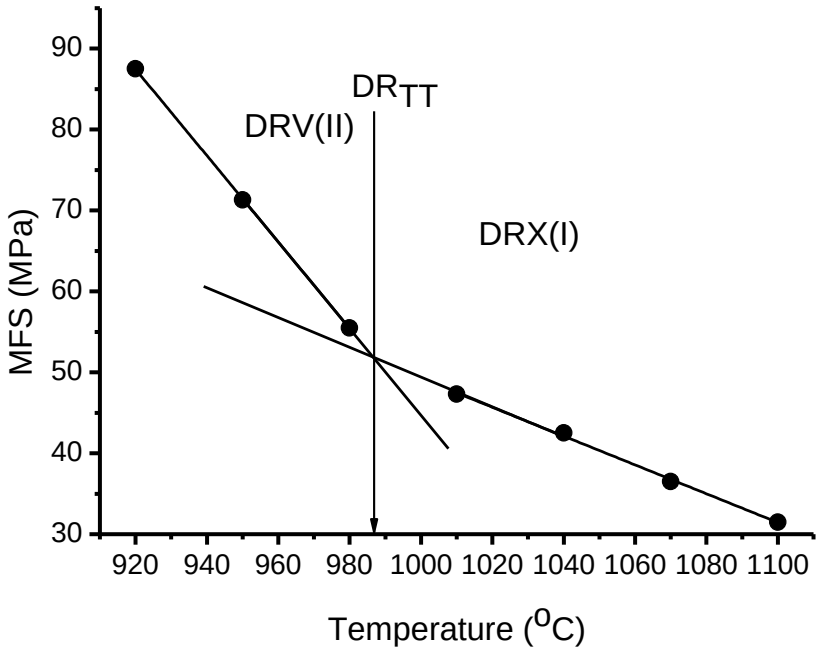

Figure 4.6 Dependence of the mean flow stress (MFS) on the deformation temperature during the multi-pass compression testing. AISI 430 stainless steel deformed at a strain rate of 0.1 s^{-1}, inter-pass time of 20 s and testing temperature from 1100 ^{o}C – 920 ^{o}C

The change in linear slope in Figure 4-5 defines two regions, namely dynamic recrystallization or the DRX region (I) and the dynamic recovery region or the DRV (II). In region I (high temperature deformation), dynamic recrystallization takes place as there is no accumulation of strain from pass to pass and therefore the increase in mean flow stress is solely due to the decrease in temperature. In region II (low temperature deformation), dynamic recovery takes place. Strain is accumulated from pass to pass within this region and hence the increase in the mean flow stress occurs more rapidly with decreasing temperature (see DRV and DRX curves in chapter 5).

4.11 Texture measurement

EBSD and XRD texture measurement techniques were applied in this study. The XRD and EBSD techniques were applied on the industrially hot rolled as well as the laboratory hot rolled plane strain condition test samples whereas the Gleeble hot compressed samples had only EBSD applied to them due to the limitation of the Gleeble's small sample size. The primary aim of the XRD technique used was to obtain a profile of diffracted intensities,

which will characterise a large neighbouring sample volume, whereas with the EBSD, the primary output was to obtain a diffraction pattern from the individual grains [56-61].

4.11.1 Texture Measurement and Analysis by EBSD technique

Electron backscattered diffraction (EBSD) measurements, with a step size of 10 % of the grain size, was performed on a region of the deformed sample equivalent to the rolling plane of the sheet (RD x TD). This area was carefully chosen with respect to the grain size so that at least 1000 or more grains were scanned to have a statistical representation of the orientation of the grains. The samples were tilted at an angle of 70^{o} to the horizontal which allowed more electrons to be diffracted towards the detector [59, 60]. EBSD patterns from a field emission in-lens SEM (FEI Nova Nano® SEM 200) equipped with an EDAX Digiview EBSD Camera was used to determine the crystallographic textures from the mid-thickness regions of the hot compressed samples, see figure 4.7.

Figure **4.7** : FEI Nova Nano® SEM 200 used for the EBSD texture measurement

A minimum number of seven Kikuchi bands were used to index a pattern during the data collection in order to ensure good reliability of information [13, 59]. An average confidence index of the patterns of more than 0.1 was used which led to more than 97 % of each patterns being indexed correctly. To make accurate measurements, misorientations of less than 1.5^{o} were excluded from the data [59]. From these results, orientation distribution functions (ODFs) were obtained using the EDAX OIM Software Suite® for data capture

and analysis and Φ_2= 45^o sections (Bunge notation). The ODFs were calculated with a 15^o Gaussian spread around the ideal orientations.

4.11.2 Texture measurement and Analysis by XRD technique

X-ray diffraction measurements were carried out in a goniometer equipped with a sample stage with 6 degrees of freedom (see figure 4.8): an Eulerian cradle with φ, χ and ω-rotation in combination with a translation sample holder with x-, y- and z-movement. At every pole figure measurement position the sample was moved in the x- and y-directions in order to cover a maximum area of the measured sample. For detection, an area detector with a high measurement speed (200 counts/pixels) was used. The setup further consisted of a cobalt X-ray tube and a collimator for the generation of a parallel beam with 1 mm spot size. Macrotexture measurements were performed using a PANalytical X'Pert Pro diffractometer with X'Celerator detector and variable divergence.

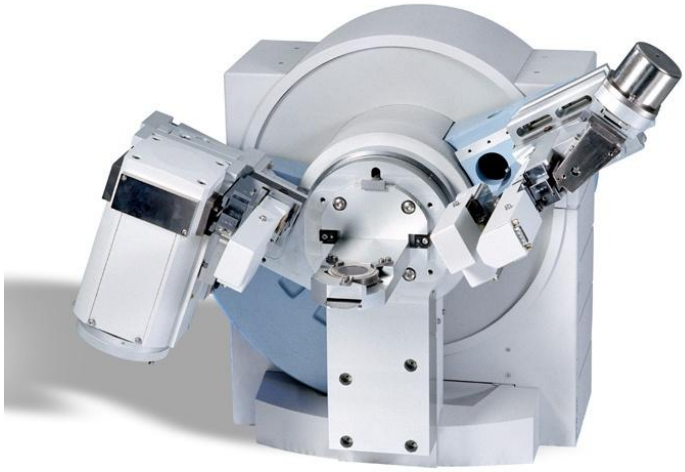

Figure 4.8 : The goniometer used for the macrotexture measurement.

Textures were quantified via incomplete pole figures measured from an area of approximately 14 mm^2 using Co-radiation in the back reflection mode. Orientation distribution functions (ODF) were calculated from the three incomplete pole figures {200}, {211} and {110} using the series expansion method (I_{max} = 22). The MTEX software was then used to analyse the obtained data. The ODFs were plotted using constant sections of

Φ_2 at intervals of 5^o, placing texture density contours within each section at 15 % levels of maximum intensity.

5 CHAPTER 5: RESULTS AND DISCUSSION

5.1 The Mill Log Analysis

The Mean Flow Stress of AISI 430 and AISI 433 FSS at each deformation pass was calculated using the Sims equations described earlier (see appendix C for full details of the equations used) from mill logs recorded data taken from mill logs provided by Columbus Stainless Steels. A plot of the calculated MFS as a function of the pass temperature is shown in figure 5.1.

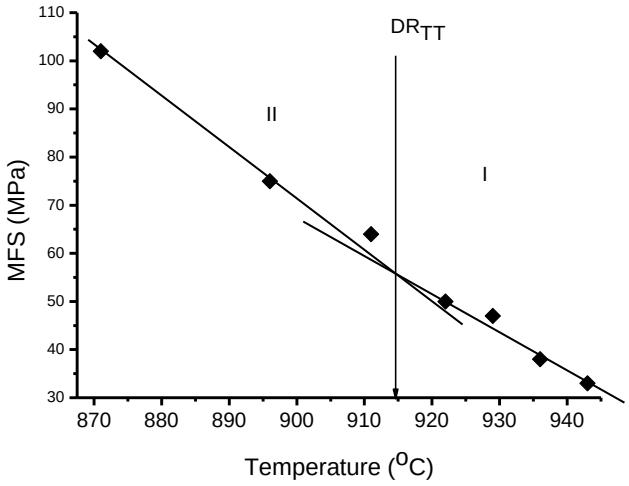

a

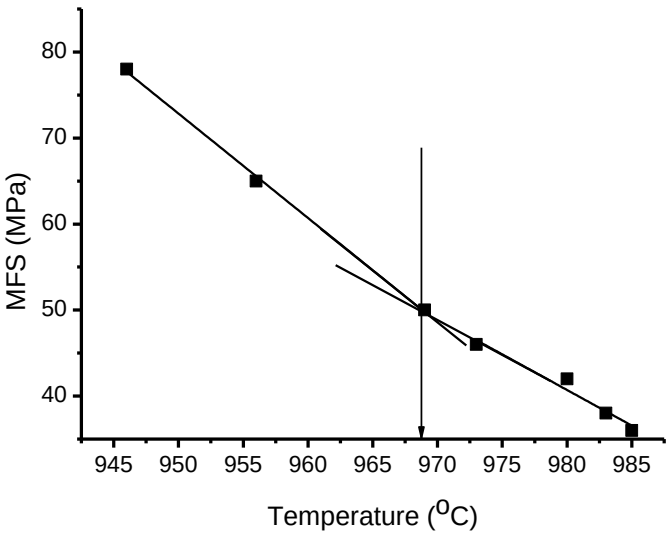

b

Figure 5.1 : The Mean Flow Stress (in MPa) from mill logs as a function of the temperature of (a) AISI 430 (b) AISI 433 received from Columbus Stainless Steel

It was noted from these calculations that the AISI 430 has a slightly higher MFS compared to that of AISI 433. The plotted data was however scattered in the case of both AISI 430 and AISI 433 and therefore lines of best fit had to be used in obtaining the graphs presented in figure 5.1. One significant observation about the two graphs is the presence of two stage behaviour regions with different slopes which describes the softening mechanisms occurring in the steels during hot deformations. The regions suggest that the softening mechanism operating at higher temperatures (DRX) is different from the mechanisms at lower temperatures (DRV).

5.2 Thermo-calc® Software Prediction

The Thermo-calc® software was used to study the phases that existed during the Steckel hot rolling as well as the phases during transformation. In both AISI 430 and AISI 433 a dual phase was observed within the temperature range of 850 ^{o}C and 1000 ^{o}C at a chromium composition of 16.2 wt% and 16.18 wt% for AISI 430 and AISI 433 respectively, see figure 5.2 and figure 5.3 below.

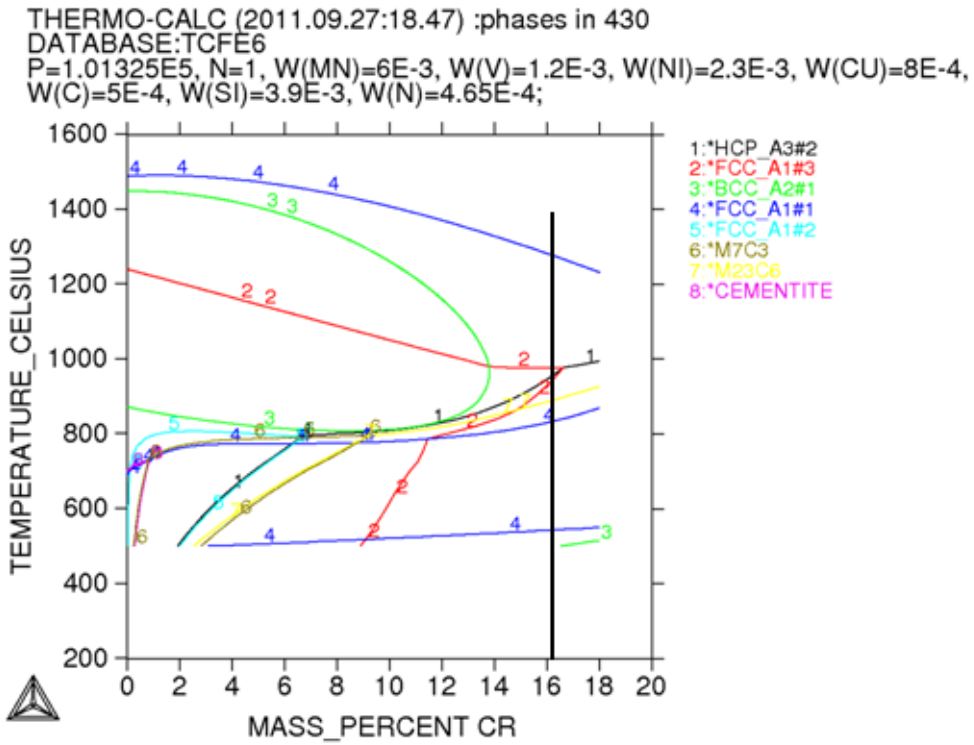

Figure 5.2: Thermo-calc® predicted phases of AISI 430 ferritic stainless steels.

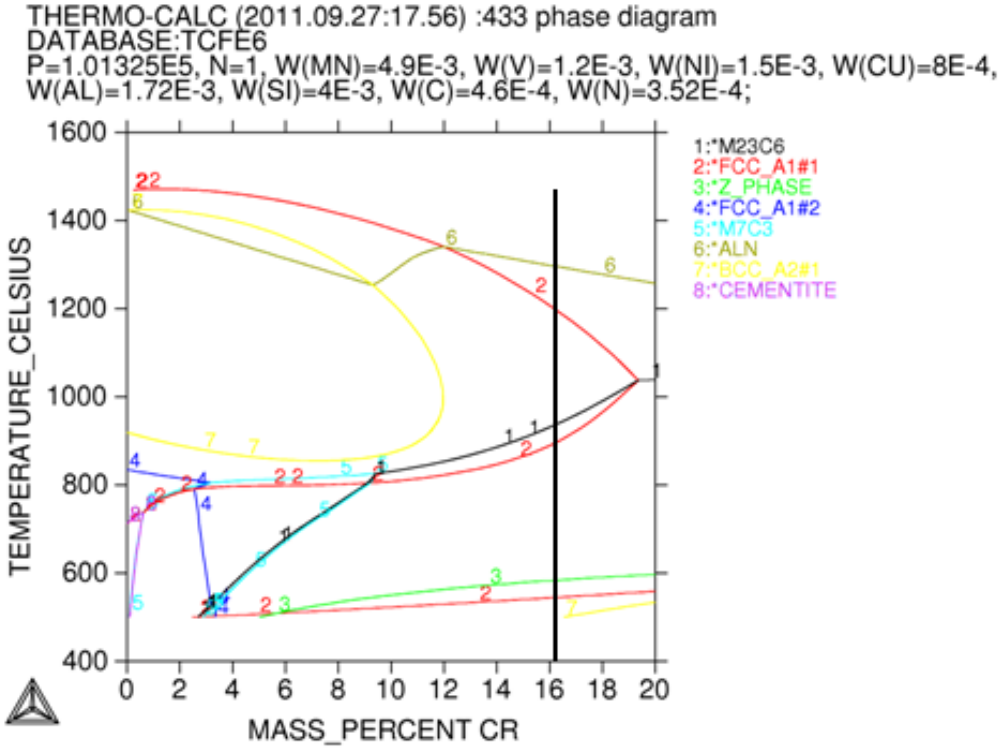

Figure 5.3: Thermo-calc® predicted phases of AISI 433 ferritic stainless steels.

The carbides M_3C_7 and $M_{23}C_6$ represented as number 6 and 1 on figure 5.2 and 5.3 is in agreement with the carbides presented on figure 2.2 as C1 and C2 respectively. The industrial hot rolling of AISI 430 and AISI 433 is done within a temperature range of 950 and 770 ^{o}C and 997 and 800 ^{o}C for AISI 430 and AISI 433 respectively. This clearly shows that the hot rolling (Steckel) of these steels is done basically within the dual phase region.Thermocalc was also used to calculate the A_{c1} temperatures of AISI 430 and AISI 433 to be 890 ^{o}C and 1035 ^{o}C respectively. These calculations and the phase transformations were validated through Baehr dilatometer work which confirms these results, see Appendix A for details of these results.

5.3 The Tensile Test

It is well known that there is a linear relationship between the R-value and the drawability or the formability of a material [98]. The R-mean values of the hotband samples as well as the final annealed samples were done in accordance with ASTM E8 standard E8M - 11 and the R-mean calculated using the equation 4.2 described earlier. The results showed that the AISI 430 has slightly lower R- values than the AISI 433 both in the hotband as well

as in the final annealed samples but the difference is however insignificant for any meaningful comparison, particularly in the final annealed steels. The summary of the results is presented in table 5-1.

Table 5-1: Summary of the tensile test results

Material	R_m – value for	
	Hotband	Final Annealed
AISI 430	0.48	1.21
AISI 433	0.56	1.24

5.4 Characterisation of the as-received samples

The as-received samples namely transfer bars (Roughing mill product), hotband material (Steckel mill product) and final annealed samples of AISI 430 and AISI 433 were analyzed by means of macrotexture (XRD) and microtexture (EBSD) techniques. The texture analysis revealed that the desired γ-fibre texture component is not optimized in both AISI 430 and AISI 433 stainless steels. The AISI 430 has both rolling textures of α-fibre (RD//<110>) and γ-fibre (<111>//ND), which can be considered a recipe for ridging if these texture components are banded; whereas the AISI 433 has a significant content of the desired γ-fibre texture component and some amount of α-fibre components present, which will also lead to ridging when banded.

The transfer bar of AISI 430 exhibited a strong rolling texture <110>//RD which later transformed to a brass texture {110} <112> during Steckel rolling. This brass texture eventually transformed to the desired γ-fibre <111>//ND ({111} <112>) and the α-fibre <110>//RD after cold rolling and annealing. This combination of strong α- and γ-fibre texture components in AISI 430 is a recipe for the formation of ridging if these textures are banded. The transfer bar of AISI 433 exhibited a strong rotated cube texture {100} <001> after roughing mill rolling which eventually transformed to nearly a Goss texture {110} <001> and a Brass texture {110}<112> after hot rolling in the Steckel mill. After cold work and annealing these Goss and Brass textures transformed into strong γ-fibre texture and a weak α- fibre texture, see figures 5.4 and 5.5.

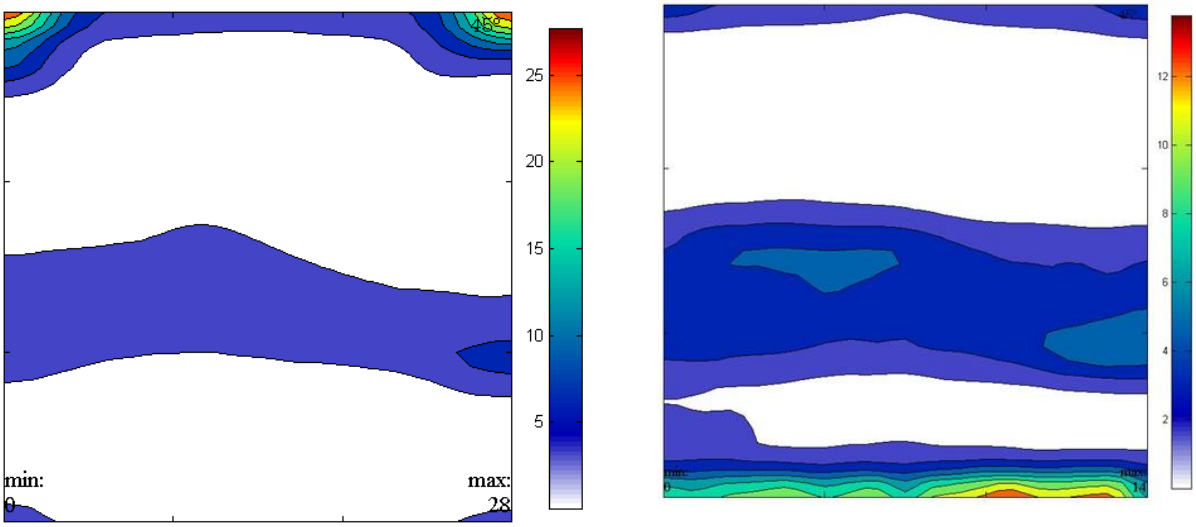

a b

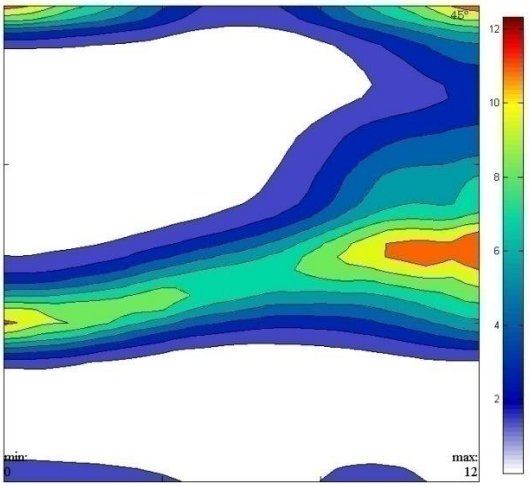

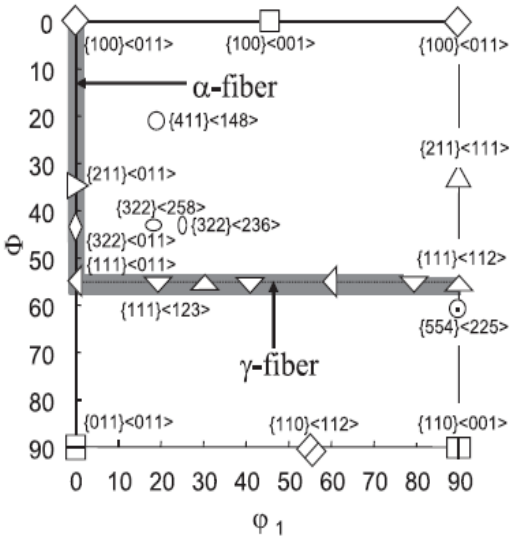

c d

Figure 5.4: XRD ODF Φ_2 = 45^o RD-TD sections of the AISI 430 samples (a) the roughing mill product (b) the Steckel mill product (c) the final annealed sample and d) the Φ_2 = 45^o section of important textures in Bunge notation used for the analysis.

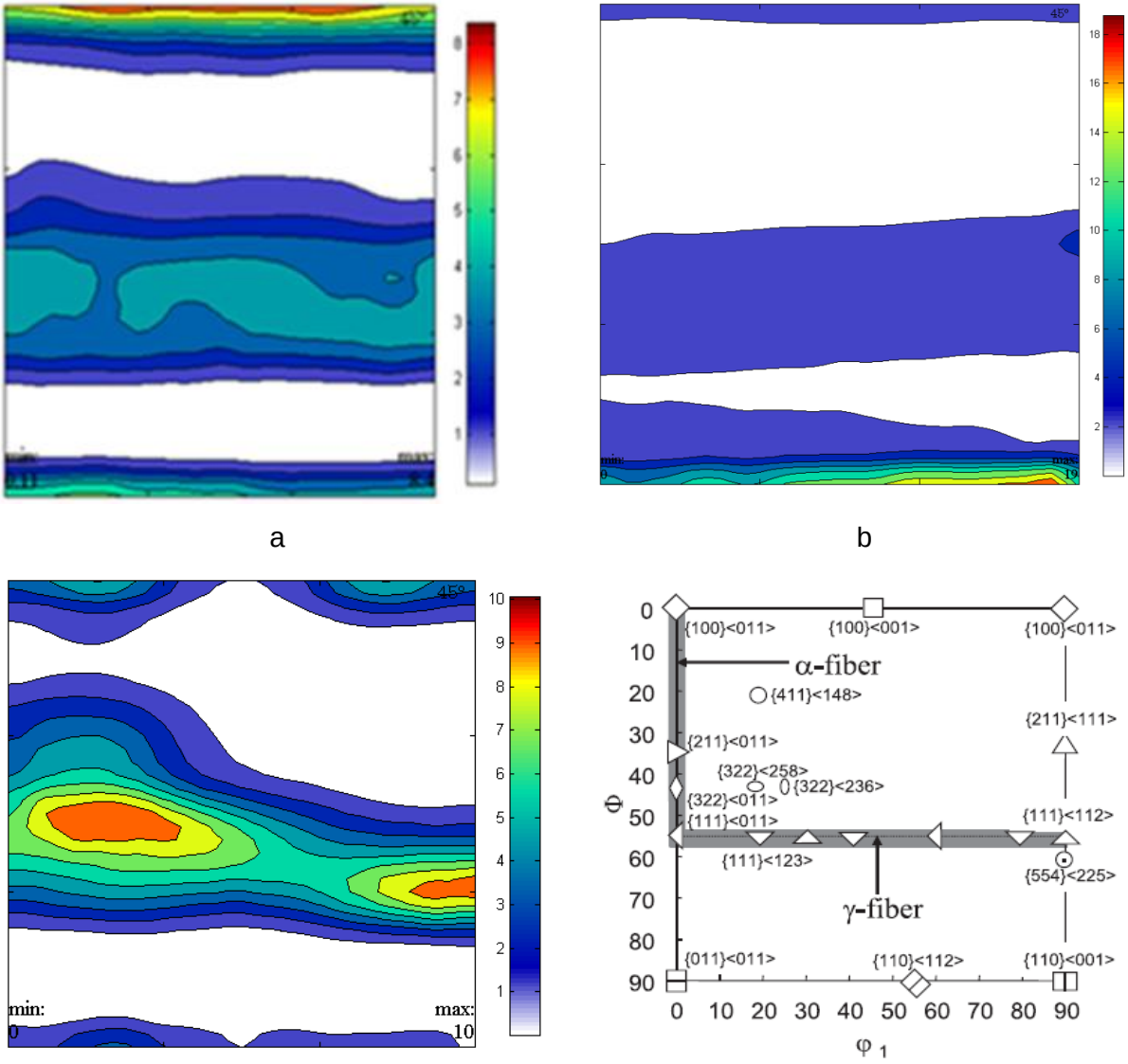

Figure 5.5: XRD ODF Φ_2 = 45° RD-TD sections of AISI 433 samples (a) the roughing mill product (b) the Steckel mill product (c) the final annealed sample and d) the Φ_2 = 45° section of important textures in Bunge notation used for the analysis.

However, the presence of α-fibre and the γ-fibre textures in the final annealed samples of the AISI 433 steel when banded, will lead to the observation of ridging in this stainless steel grade. The summary of this result is presented in table 5-2.

Table 5-2: Summary of the analysis of the texture of the as received samples

Material		Observed Textures
PRODUCTION STAGE	**TYPE**	
After Roughing (Transfer Bar)	433 R	{100}<001>, {011}<011> , {100}<011>
	430R	{100}<011>, {110}<001>, {011}<011>
After Steckel (Hotband)	433H	{110}<001>, {011}<011>, {110{<112>
	430H	{110}<001>,{011}<011>, {110}<112>
After Final Anneal	433F	{111}<011>, {554}<225>, {111}<112>, {111}<011>
	430F	{111}<112>, {100}<011>, {322}<011>, {110}<001>

The recorded or observed differences in texture between the roughing mill and the Steckel mill products is an indication that there is some form of dynamic recrystallization taking place during the Steckel mill rolling. This implied that by carefully optimising the hot rolling conditions on the Steckel mill, a desired texture may possibly be obtained due to the occurrence of DRX, since dynamic recrystallization is a form of phase transformation and will lead to a change in texture whereas dynamic recovery which is considered not to be a phase transformation, will not lead to a change in the texture of the material [45]. As shown in Figure 5.4 and 5.5, the texture in the as-received samples is a combination of α-fibre <110>//RD and γ-fibre <111>//ND textures. If these textures are retained in the subsequent cold working and annealing processes, poor drawability of this steel and subsequently ridging could occur [57, 58].

5.5 The Softening kinetics of AISI 430 and AISI 433

The hot rolling conditions used for the single hit compression tests are summarised in table 5-3 below. The shapes of the flow curves obtained from the tests were used to differentiate between the occurrences of dynamic recrystallization and dynamic recovery.

Table 5-3: The hot rolling conditions used for the single hit compression tests.

Condition	Hot rolling parameters	
	Temperature (^{o}C)	Strain rate (s^{-1})
A	11000	50
B	1100	25
C	1100	5.0
D	1100	3.0
E	1100	1.0
F	1100	0.5
G	1100	0.1
H	900	50
I	900	25
J	900	5.0
K	900	3.0
L	900	1.0
M	900	0.5
N	900	0.1

5.5.1 The flow curves from the single hit compression tests

Both AISI 430 and AISI 433 exhibited comparable flow curves when deformed at different simulated rolling conditions as described in table 5.3. The true stress - true strain curves of the steels compressed at the conditions described in table 5-3 using single hit compression, are shown in Figure 5.6.

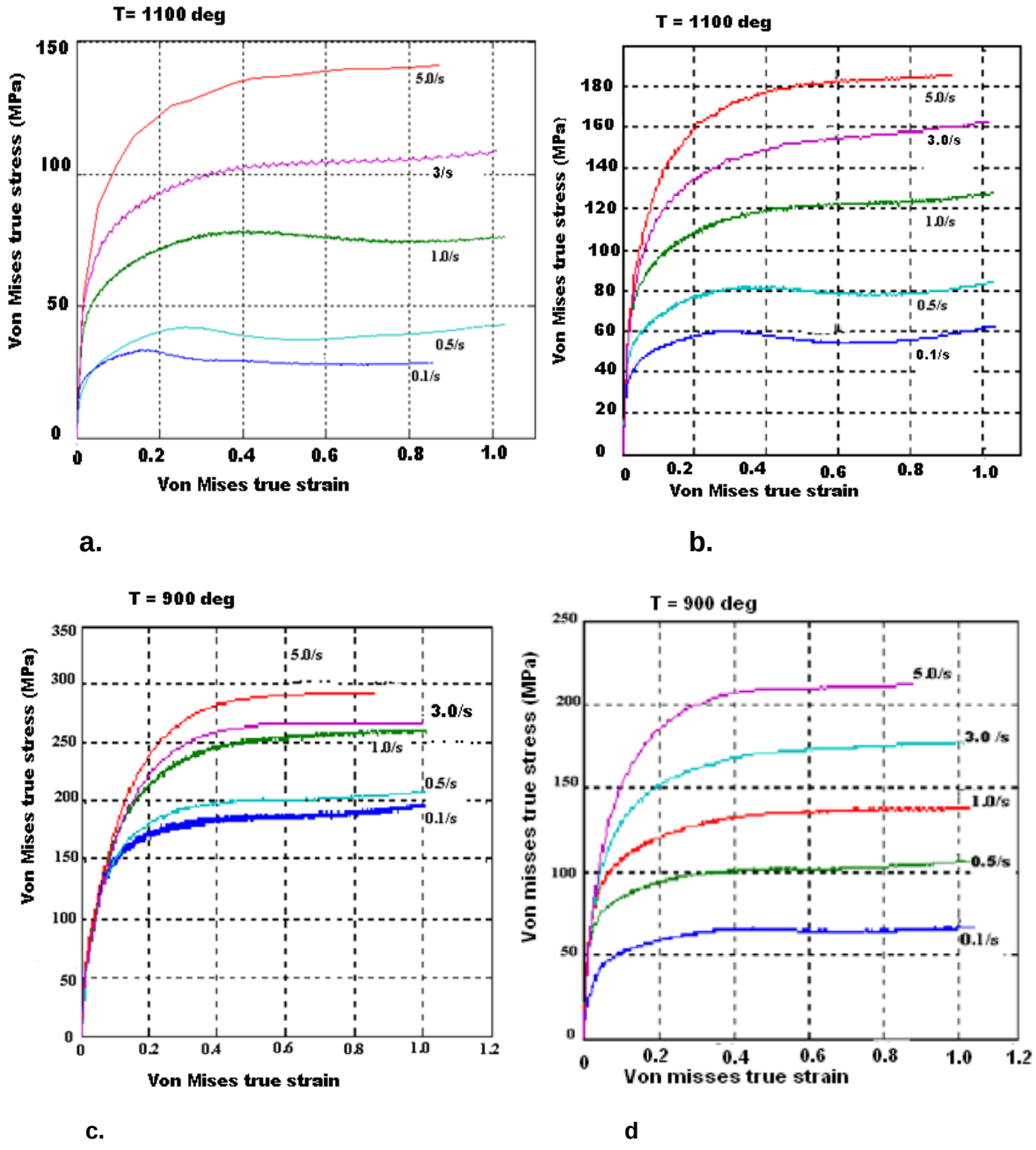

Figure 5.6: Stress – strain curves for deformation at strain rates of 0.1 s^{-1}, 0.5 s^{-1}, 1 s^{-1}, ^{1}, 3 s^{-1} and 5 s^{-1} and at different temperatures. (a) AISI 430 at 1100 ^{o}C (b) AISI 433 at 1100 ^{o}C, (c) AISI 430 at 900 ^{o}C and (d) AISI 433 at 900 ^{o}C

Characteristically, the foremost approach used here in detecting the occurrence of dynamic recrystallization is by assessment of the flow curves. The post-peak softening of the flow curves, as displayed by most materials, can be taken as indicative of dynamic recrystallization. If no post-peak softening is observed but only a steady state region as

occurs at lower temperatures or higher strain rates in this steel (BCC metals), dynamic recovery is then believed to occur. In this study, slight peaks which were higher than the steady state region were reached, (Figures.5-6 (a) & (b)). Firstly, the curves exhibit a maximum or peak stress indicating the occurrence of dynamic recrystallization in the specimens deformed at 1100 ^{o}C, and strain rates of 0.1 s^{-1}, 0.5 s^{-1}, and 1 s^{-1} (thus conditions E, F, G) for both AISI 430 and AISI 433, whereas the specimens deformed under the other conditions described in table 5-3 (A, B, C,D, H, I, J, K, L, and M) exhibited dynamic recovery, thus a steady state region is obtained at higher strain rates as the deformation temperature decreases.

There is a perceptible change in the shape of the flow curve between higher temperature and higher strain rate curves on the one hand and the higher temperature and lower strain rate curves on the other hand. The former curves show no tendency to decrease in flow stress once the peak is reached, depicting the occurrence of DRV. The higher temperature and lower strain rate curves, however, display a steady decrease in stress beyond the peak, indicating the occurrence of DRX. Even though this behaviour could be attributed to other factors than temperature and strain rate, the view is taken here that the shape change shows that a different form of softening is occurring at high temperatures and lower strain rates that is not present at the higher temperatures and higher strain rates. This interpretation is supported in the later discussion of the microstructures and the texture observations.

5.5.2 Gleeble Feedback Acquisition for the Multi-pass Compressions

Three channels of feedback recorded from the Gleeble during the compression tests helped in presentation of these multi-pass results. These channels were the measured temperature at the thermocouple, axial load and stroke distance. The temperature was recorded to make sure the test schedule was followed. The force measured by the load cell and the stroke distance were the most critical data acquired. The force acquisition showed the increased residual stress after cooling to room temperature from the deformation temperatures. The axial force measured was converted into true stress with units of MPa and the stroke distance converted to true strain by using the standard equations described in equation 4.7 and 4.8. Figure 5.7 shows a typical data acquisition plot for the flow curve obtained from such a test.

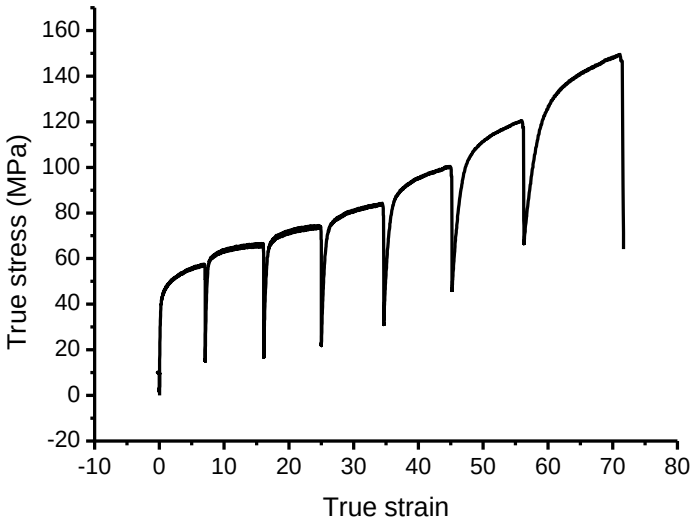

a

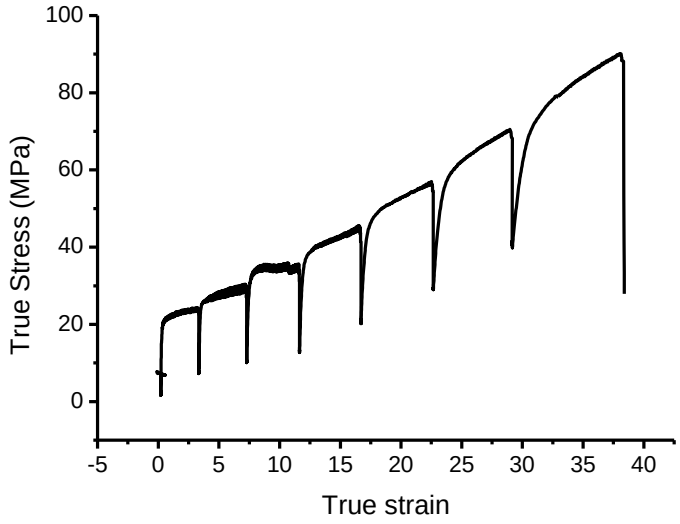

b

Figure 5.7: True stress – strain curves for (a) AISI 430 (b) AISI 433, samples deformed at a strain rate of 1 s^{-1} using a 7 pass schedule, starting at 1100 ^{o}C and ending at 920 ^{o}C and a constant inter-pass time of 20 s

5.5.3 Dynamic recrystallization to dynamic recovery transition temperature (DR_{TT})

The mean flow stress (MFS) per pass was calculated from the flow curves (Figure 5.7) obtained. A plot of the mean flow stress as a function of the temperature made it possible

for two regions of interest with different slopes shown in Figure 5.8 to be obtained and this was used in determining the dynamic recrystallization to dynamic recovery transition temperature, DR_{TT}.

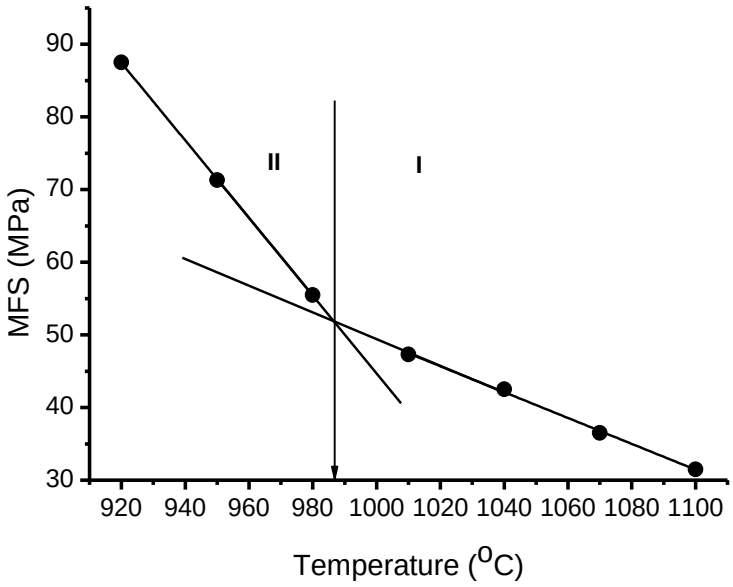

a

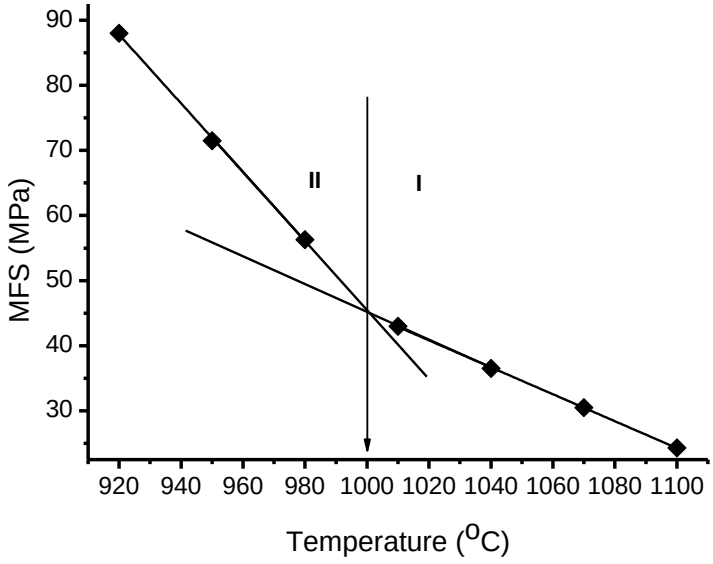

b

Figure 5.8: Dependence of the mean flow stress (MFS) on the deformation temperature during the multi-pass compression testing. (a) AISI 430 (b) AISI 433, Samples deformed at a strain rate of 1 s^{-1}, an inter-pass time of 20 s and testing temperatures from 1100 °C to 920 °C

It was noted from these plots that the DR_{TT} increases with decreasing Mean Flow Stress, thus a similar observation which was made from the mill log analysis. The two regions are DRX (I) and DRV (II).

5.5.4 Effect of Strain Rate on the DR_{TT}

The mean flow stress increases with increasing strain rate. This results from the fact that there is a greater restoration by dynamic recovery at the lower strain rates. Taking for instance a strain rate of 0.1 s^{-1}, the deformation time for a strain of 0.14 is 1.4 seconds. By contrast, at a strain rate of 5 s^{-1}, the deformation time is only 0.03 seconds over the same strain interval. Such less-restored and more highly work hardened austenite supplies more driving force for the dynamic recrystallization and therefore decreases the DR_{TT}. The results presented in Figure 5.9 demonstrate the effect of strain rate on the DR_{TT} for steels deformed over the same temperature range (1100 ^{o}C – 920 ^{o}C), the same inter-pass times (20 s) but different strain rates (0.1 s^{-1}, 0.5 s^{-1}, 1 s^{-1}, 2 s^{-1}, 3 s^{-1} and 5 s^{-1}).

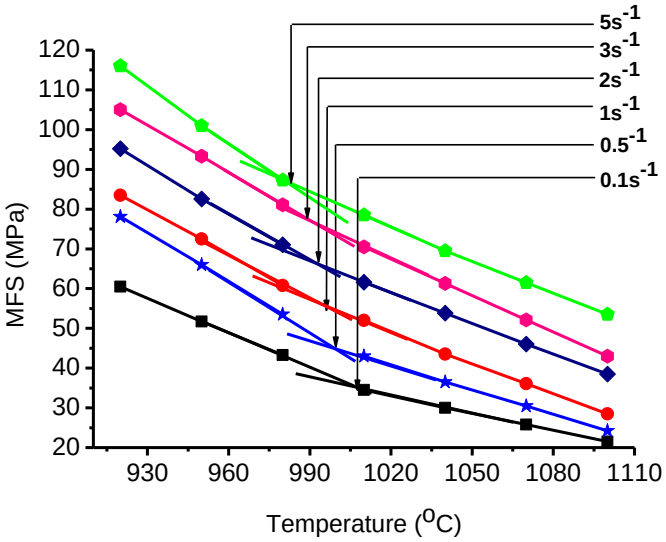

a

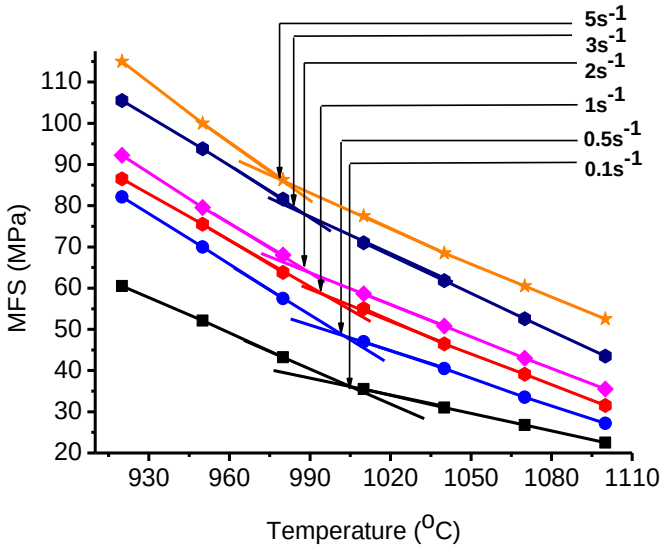

b

Figure 5.9: MFS versus the deformation temperature for (a) AISI 430 (b) AISI 433 samples deformed at an inter-pass time of 20 s, temperature range of 1100 ^{o}C to 920 ^{o}C and respective strain rates of 0.1 s^{-1}, 0.5 s^{-1}, 1 s^{-1}, 2 s^{-1}, 3 s^{-1} and 5 s^{-1}

Figure 5.10 illustrates the relationship between the strain rate and the DR_{TT} during the compression test of the samples.

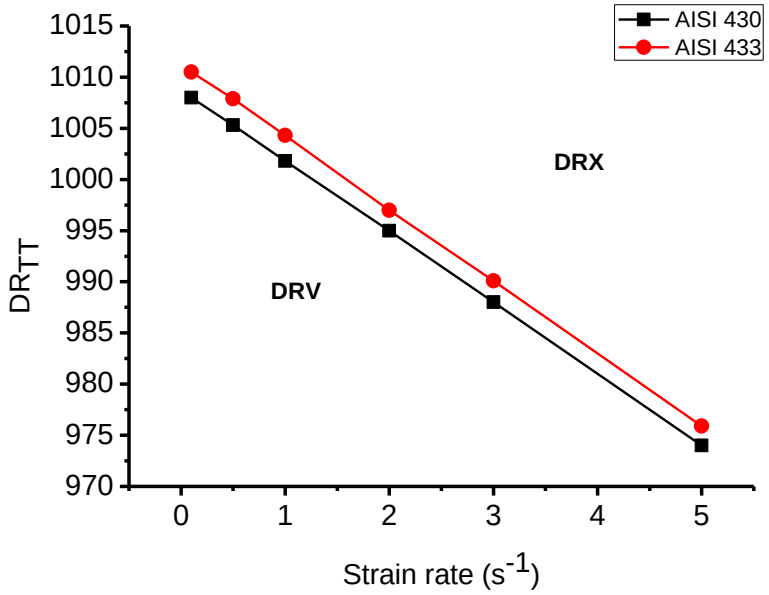

Figure 5.10: Relationship between the DR_{TT} and the strain rate for AISI 430 and AISI 433 from the deformation data of Figure 5.9

This graph clearly shows that as the strain rate increases the DR_{TT} decreases and this indicates that at a high deformation temperature and low strain rate, dynamic recrystallization occurs whereas at a low temperature and low strain rate, dynamic recovery occurs. Note also that in AISI 433 a slightly higher rolling temperature will be needed to initiate DRX for introducing a texture change than in AISI 430 although the difference is rather small.

5.5.5 Effect of Inter-pass Time on DR_{TT}

The DR_{TT} increases with increasing inter-pass times. At temperatures above the DR_{TT} the inter-pass times do not affect the mean flow stress as dynamic recrystallization takes place within the passes and hence no further softening takes place during the inter-pass time. At deformation temperatures below the DR_{TT}, however, further softening takes place during the inter-pass time largely due to dynamic recovery; hence, the increase in mean flow stress can be ascribed to the decrease in temperature and the retardation of dynamic recrystallization. The dependence of DR_{TT} on the inter-pass time is illustrated in Figure 5.11 for the steels deformed over the same temperature range (1100 ^{o}C - 920 ^{o}C), same

strain rate (0.1 s^{-1}) but different inter-pass times (2 s, 10 s, 20 s and 30 s). Figure 5.12 illustrates the relationship between the DR_{TT} and the inter-pass times.

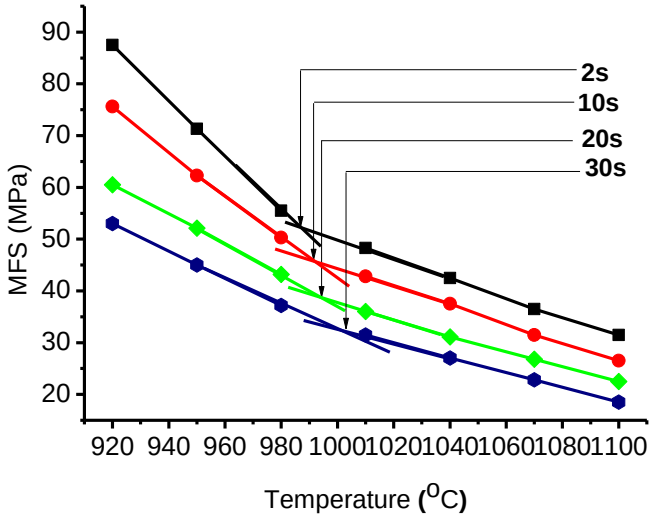

a

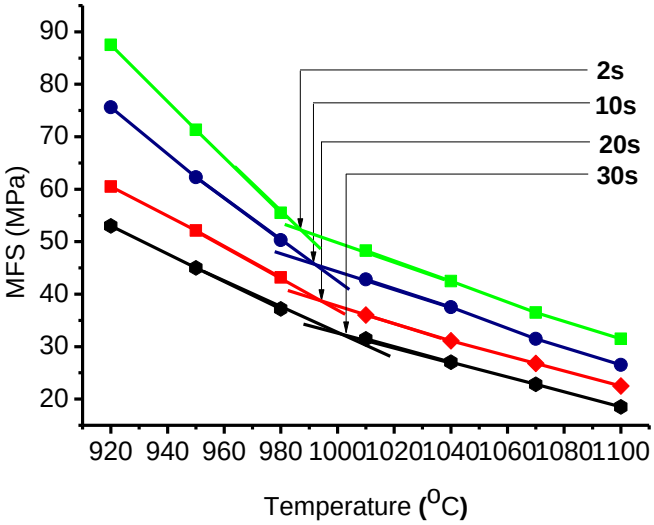

b

Figure 5.11: MFS versus the deformation temperature for (a) AISI 430 (b) AISI 433, samples deformed at different inter-pass times of 2 s, 10 s, 20 s and 30 s, the same temperature range of 1100 °C to 920 °C and at a constant strain rate of 0.1 s^{-1}

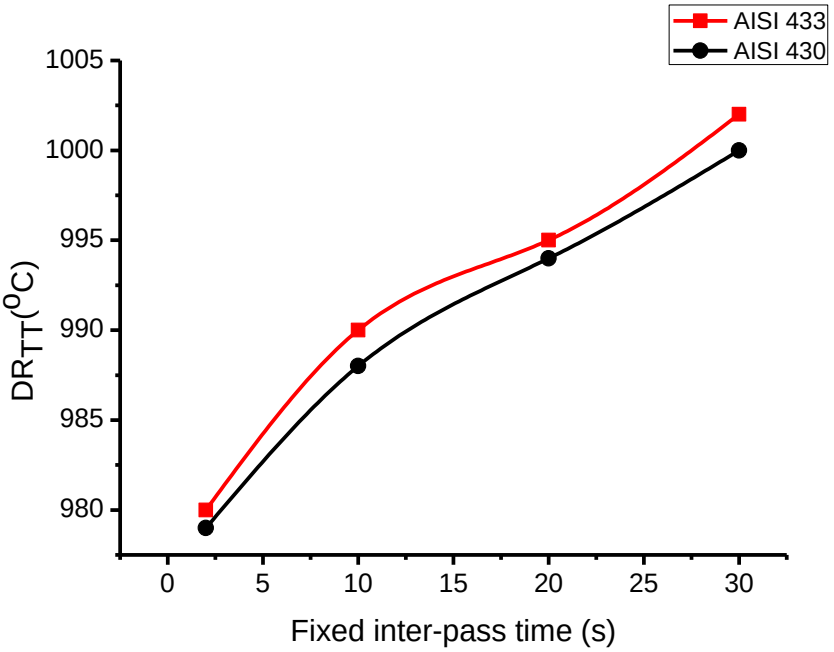

Figure 5.12: Relationship between the DR_{TT} and the fixed inter-pass time for the multi-pass deformation data of AISI 430 and AISI 433 from Figure 5.11

Note once more that for a given rolling temperature AISI 433 will require a slightly higher temperature at a fixed inter-pass time for multi-pass testing to experience DRX in order to enable any texture changes to take place than is the case in AISI 430. The difference is, however, quite small.

5.6 Microstructural Observations

Another means used in distinguishing the occurrence of dynamic recrystallization from the dynamic recovery was through microstructural analysis. The microstructures of the as received samples of both AISI 430 and AISI 433 are shown in Figure 5.13. The microstructure of samples in which dynamic recrystallization had occurred through grain refinement showed formation and growth of new strain-free grains within the deformed matrix. These newly formed grains have a smaller grain size than the original grains. During the deformation, the grains also rotate and elongate in order to accommodate the dimensional changes. These two factors helped in distinguishing the occurrence of dynamic recrystallization from dynamic recovery under different hot rolling conditions.

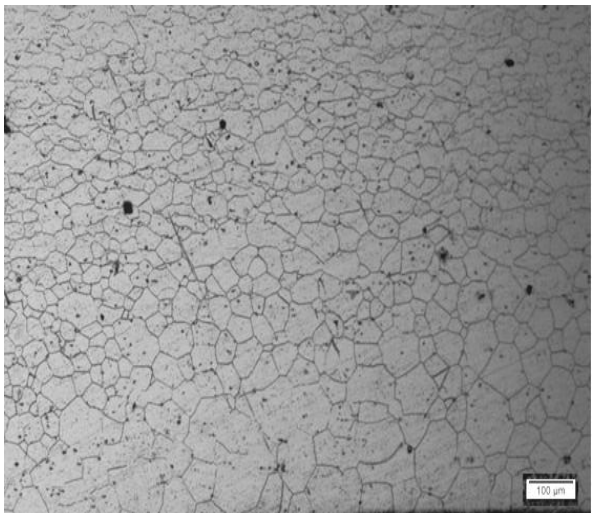

a

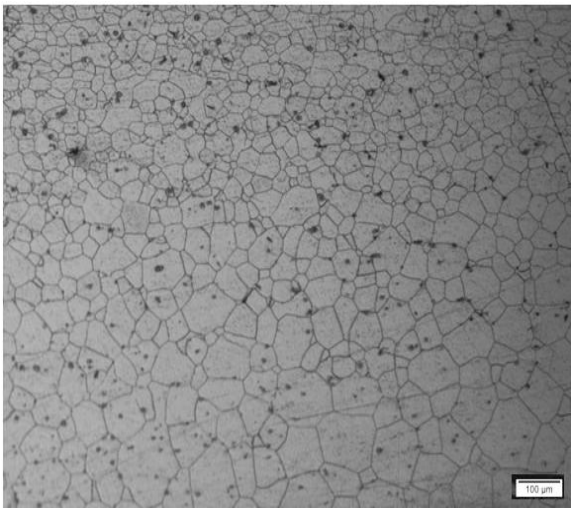

b

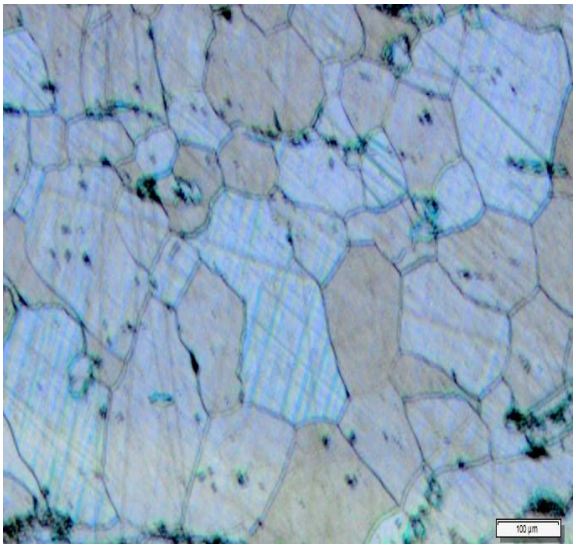

c

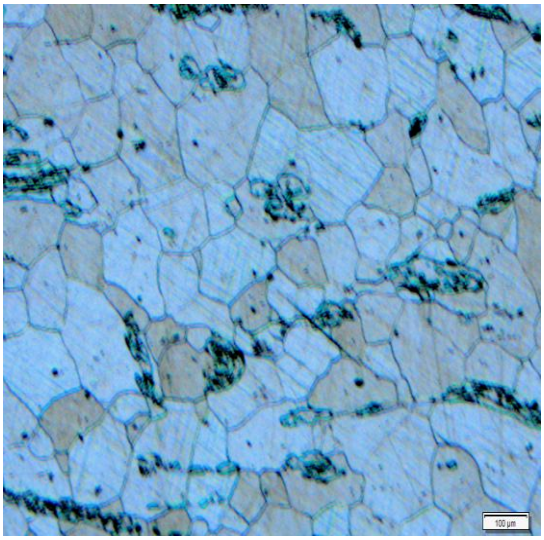

d

Figure 5.13: Optical microstructures of the as received samples etched in Ralph's reagent (a) AISI 430 final annealed (b) AISI 433 final annealed (c) AISI 430 hotband and (d) AISI 433 hotband

The hot rolling conditions used for the multiple compression tests are summarised in table 5-4 below.

Table 5-4: The hot rolling conditions used for the multiple compression tests selected for the texture analysis

Rolling Condition	**Hot rolling parameters**		
	Temperature (^{o}C)	Strain rate (s^{-1})	Inter-pass time (s)
A	1100 – 920	0.1	2
B	1100 – 920	0.1	20
C	1000 – 820	0.1	20
D	1100 – 920	5.0	20
E	1100 – 920	5.0	2
F	1000 – 820	5.0	20
G	1100 – 920	25	20
H	1000 - 820	50	20

After deformation there were changes in the microstructures of the deformed samples with respect to the different hot rolling conditions**.** Samples of both AISI 430 and AISI 433 deformed under conditions A (1100-920 ^{o}C, 0.1 s^{-1}, 2 s) and B (1100-920 ^{o}C, 0.1 $s^{-1,}$ 20 s) had the formation of a second phase (delta ferrite), see figure 5.14 and figure 5.15. The structure of the grains found under these conditions (A and B) are finer and more equiaxed due to recrystallization. In addition the degree of refinement due to recrystallization is higher under these higher temperatures than at the lower temperatures.

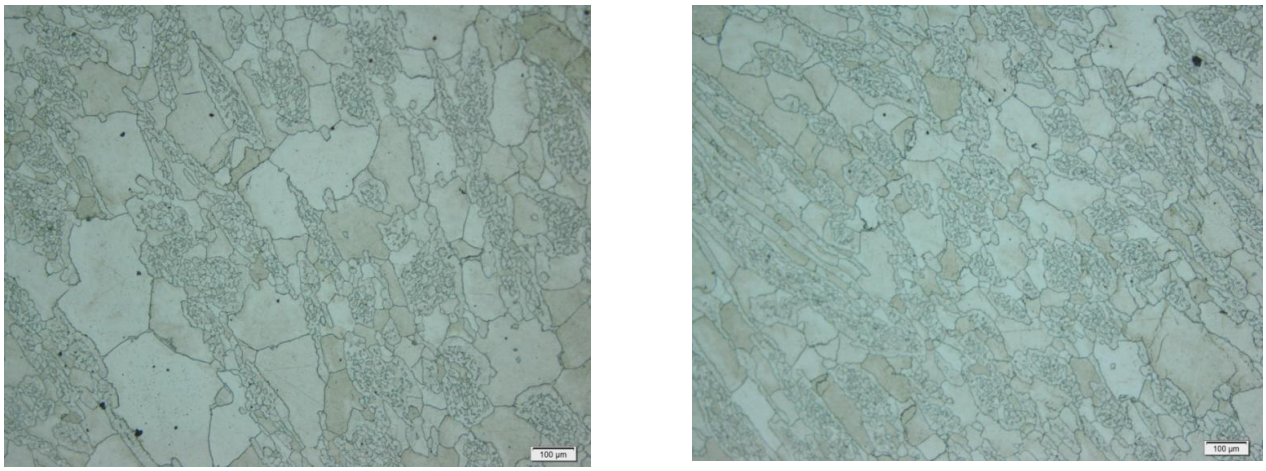

a b

Figure 5.14 : Optical microstructures of (a) AISI 430 (b) AISI 433, samples, deformed at 1100 ^{o}C, 0.1 s^{-1}, an inter-pass time of 20 s, and etched in Ralph's reagent.

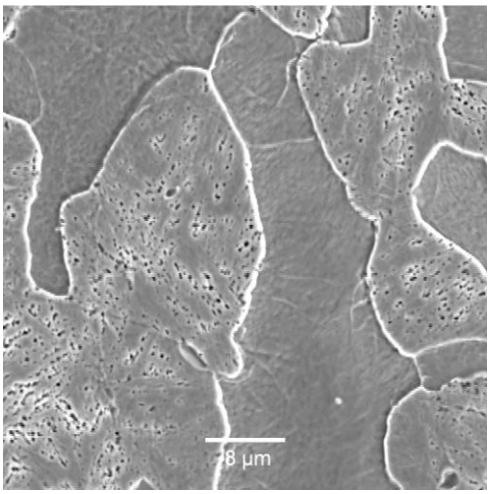

Figure 5.15: SEM Micrograph of AISI 430 sample deformed at 1100 ^{o}C-900 ^{o}C, strain rate of 0.1 s^{-1} and inter-pass time of 2 s.

The microstructures of samples deformed under conditions C (1000-820 ^{o}C, 0.1 s^{-1}, 20 s), D (1100-920 ^{o}C, 5 s^{-1}, 20 s), E (1100-920 ^{o}C, 5 s^{-1}, 2 s), F (1000-820 ^{o}C, 5 s^{-1}, 20s), G (1100-920 ^{o}C, 25 s^{-1}, 20 s) and H (1000-820 ^{o}C, 50 s^{-1}, 20 s) for both AISI 430 and AISI 433 had a mixture of grain sizes but without visible formation of new grains or a second phase as was seen in figure 5.14 for condition A and B. These microstructures are less refined due to the occurrence of dynamic recovery during hot rolling under the conditions (C, D, E, F, G and H) described earlier. These grains are not equiaxed. Whilst some of the grains are very large in size others are quite small. These observed differences in grain size in these structures characterises the occurrence of DRV in the steels at these hot rolling conditions, see figure 5.16.

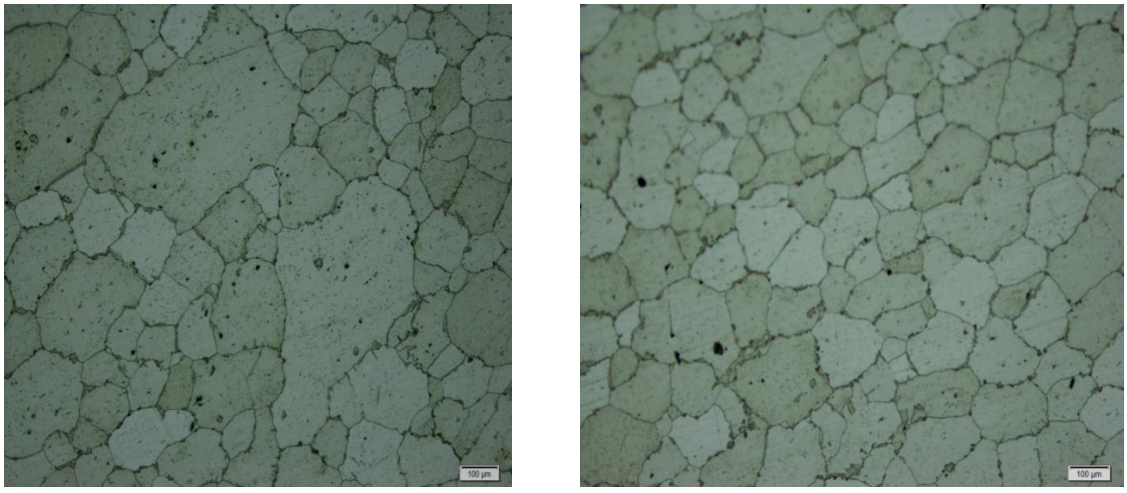

a b

Figure 5.16: Optical microstructures of (a) AISI 430 (b) AISI 433 samples deformed at 1100 ^{o}C, at a strain rate of 5 s^{-1} and an inter-pass time of 2 s and etched in Ralph's reagent

Combination of this interpretation with the flow curve analysis offers a good indication that some form of dynamic recrystallization is occurring in these steel grades during the Steckel rolling which is likely to lead to changes in the texture of these steels.

5.7 Texture Measurements

The hot rolling conditions of selected deformed samples for texture analyses presented in table 5-4 are described in details in table 5-5 and these were used for the texture analysis in the study.

Table 5-5: Description of the hot rolling conditions used for the multiple compression tests

Rolling Condition	**Hot rolling parameters**		
	Temperature (^{o}C)	Strain rate (s^{-1})	Inter-pass time (s)
A	high	Low	Short
B	high	low	long
C	low	low	long
D	high	moderate	long
E	high	moderate	Short
F	low	moderate	Long
G	high	high	long
H	low	high	long

Figure 5.17 shows important fibres and orientations on the $\Phi_2 = 45^0$ sections in ODF (Bunge notation) which was used to analyse the texture maps.

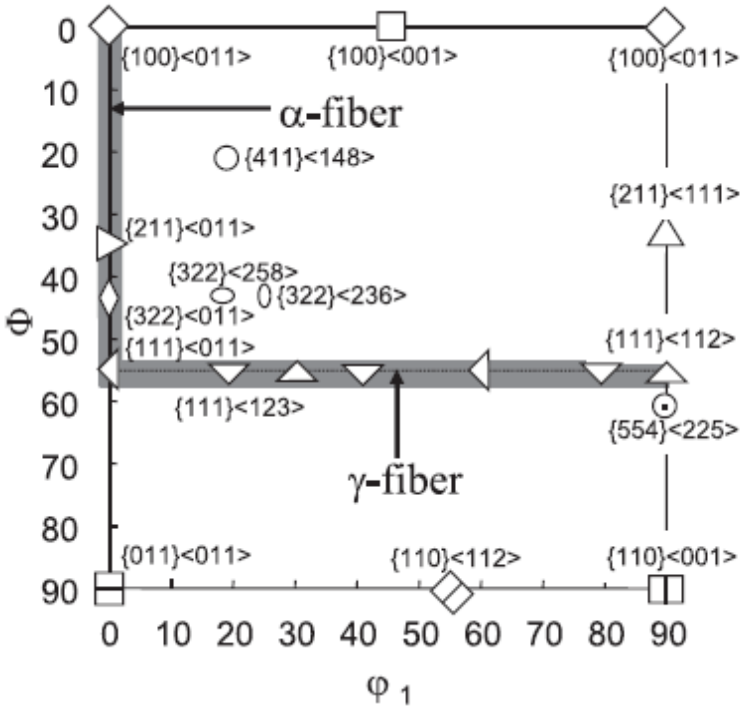

Figure 5.17: Some important textures and orientations in Euler space (Φ_2= 45^0 sections) in Bunge notation used in the texture analysis [57].

5.7.1 Texture in AISI 430

The texture of the hot-rolled steel sheet has a significant influence on the evolution of texture in the cold-rolled as well as in the annealed steel sheets [87, 89]. The texture is responsible for the Lankford ratio (R-value). The low R-value of hot rolled AISI 430 accounts for the poor drawability, which is well recognised in hot rolled steel [84-86]. The texture of the steel hot rolled using condition A (1100 -920 ^{o}C, 0.1 s^{-1}, 2 s) and B (1100-920 ^{o}C, 0.1 s$^{-1,}$ 20 s), exhibited similar textures. The texture found in these conditions consists of a strong α- fibre texture RD//<110>, ({011} <011>) and a weak γ-fibre {111} <112> as shown in Figure 5.18 (a) & (b). These conditions represent a combination of a high finishing rolling temperature (1100 ^{o}C to 920 ^{o}C) and a low strain rate (0.1 s^{-1}). The only significant difference between these conditions is the inter-pass time. With an increase in inter-pass time from 2 s in condition A to 20 s in condition B led to an increase in the intensity of the {011) <011> texture from 2.1 in A to 3.2 in B. The γ-fibre texture is however not completely uniform and shows a maximum at {111} <112> locations.

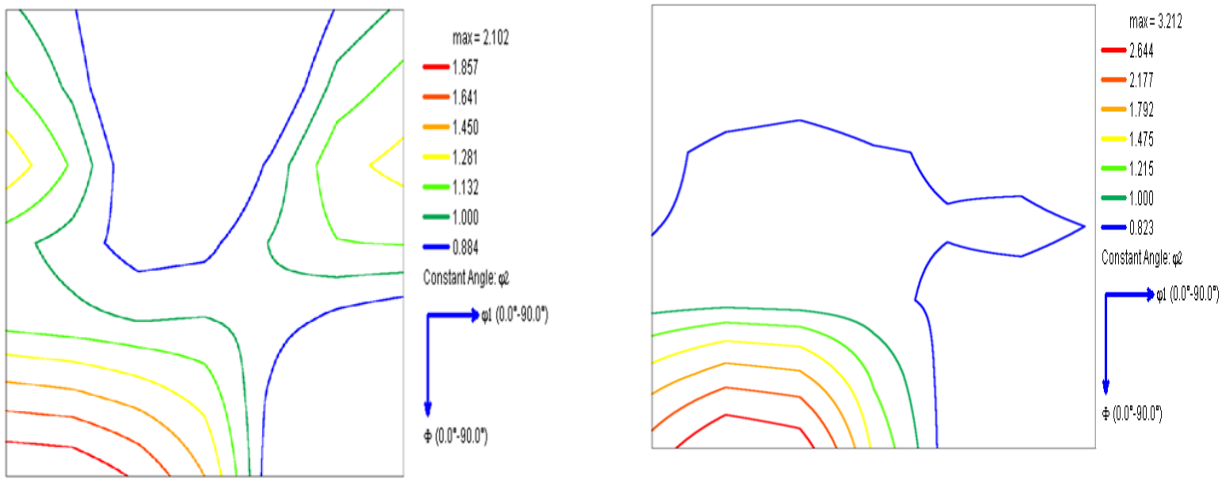

a b

Figure 5.18: EBSD ODF Φ_2 = 45^o RD-TD sections of the AISI 430 samples deformed at 1100 ^{o}C, to 920 ^{o}C, strain rate of 0.1 s^{-1} and inter-pass time of (a) 2 s (b) 20 s

Some form of change in texture seems to appear after deformation at conditions C (1000-820 ^{o}C, 0.1 s^{-1} and 20 s), D (1100-920 ^{o}C, 5 s^{-1}, and 20 s), E (1100-920 ^{o}C, 5 s^{-1} and 2s) and F (1000-820 ^{o}C, 5 s^{-1} and 20s). The Φ_2 = 45^o sections of the samples deformed under these conditions are presented in Figure 5.19 (a)–(d). The texture of the steel hot rolled under these conditions consists of weak γ- fibre textures and strong α-fibre texture along with the rotated cube component {100} <001>. The rolling conditions C and E led to the sharpening of the strongly rotated cube component {100} <001> with weaker γ-fibres {111} <112> as shown in Figure 5-19 (a) & (c). Increasing the inter-pass time from 2 s (condition E) to 20 s (condition D) led to a slight improvement in the γ-fibre, {111} <112> intensity from 1.0 in E to 1.3 in D.

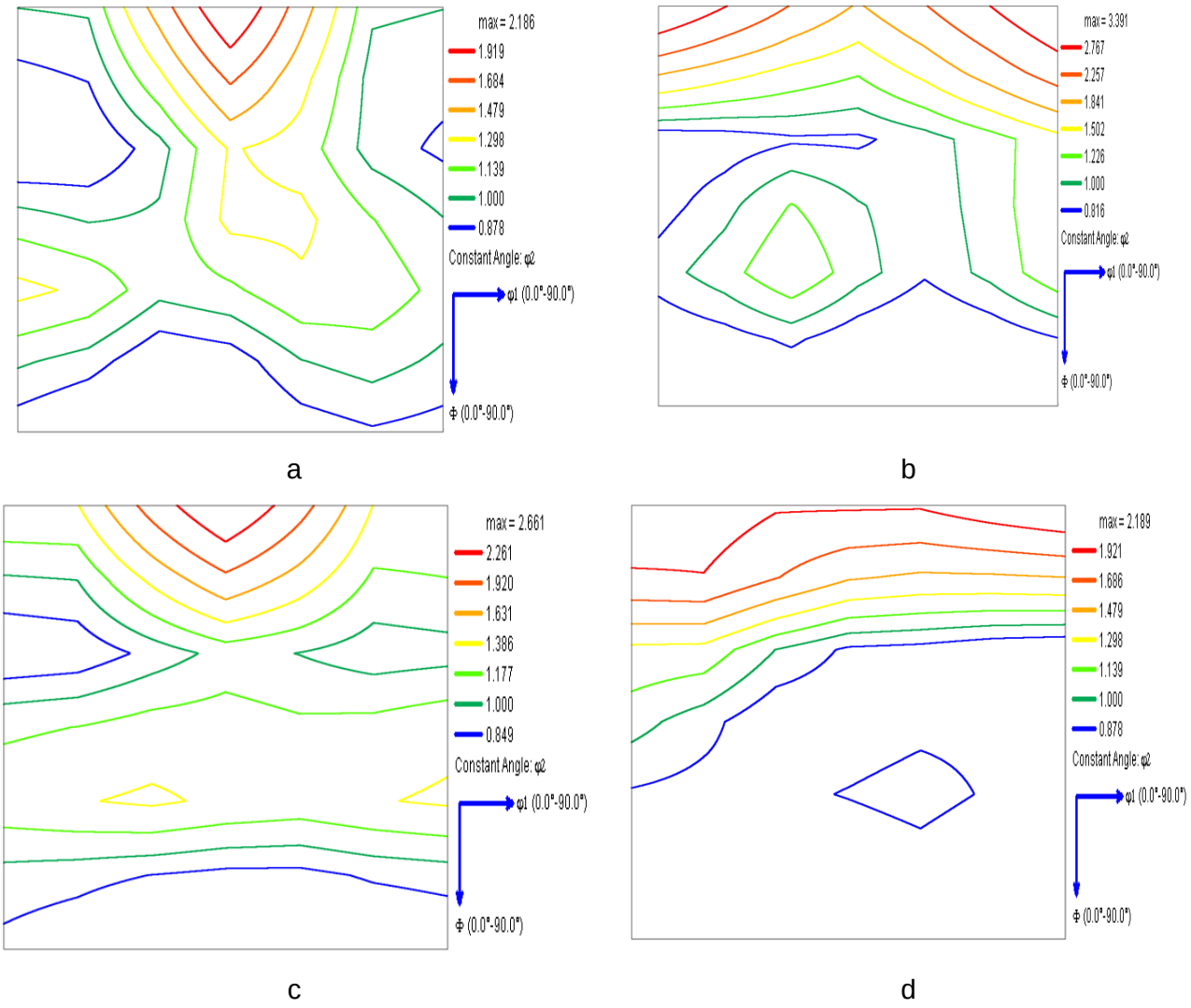

Figure 5.19: EBSD ODF Φ_2 = 45° RD-TD sections of the AISI 430 samples deformed at : (a) 0.1 s^{-1}, 1000 °C – 820 °C and 20 s (b) 5 s^{-1}, 1100 °C – 920 °C, and 20 s (c) 5 s^{-1}, 1100 °C – 920 °C and 2 s (d) 5 s^{-1}, 1000 °C – 820 °C and 20 s

Goss texture was observed in the samples deformed under conditions G (1100-920 °C, 25 s^{-1}, 20 s) and H (1000-820 °C, 50 s^{-1}, 20 s). With a decrease in deformation temperature from 1100 °C to 1000 °C and an increase in strain rate from 25 s^{-1} to 50 s^{-1} led to the weakening of the rotated cube component texture {100} <001>, see figure 5.20 (a) and (b).

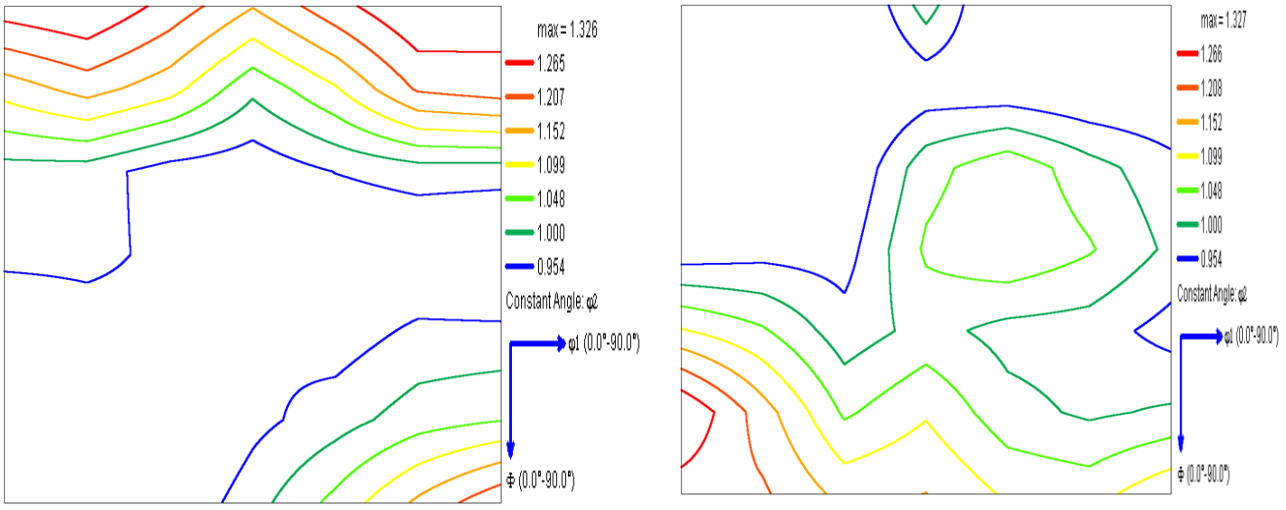

a b

Figure 5.20: EBSD ODF $\Phi_2 = 45^o$ RD-TD sections of the AISI 430 samples deformed at (a) 25 s^{-1}, 1100 ^oC – 920 ^oC and 20 s (b) 50 s^{-1}, 1000 ^oC – 820 ^oC and 20 s

The presence of the γ-fibre and α-fibre textures in all the hot rolled samples (with different volume fractions of the {111} <112>, {554} <225> and {011} <011> components) indicates that the problem of ridging during processing will be present in these steels if these textures are retained after cold rolling and annealing and if possibly banded [74–76]. However strength of the γ-fibre in the sample rolled under conditions A and B is also expected to impart positively on the deep drawing behaviour in this material.

Figure 5.21 shows the image quality maps of the AISI 430 samples deformed under conditions B (1100-920 ^oC, 0.1 $s^{-1,}$ 20 s) and E (1100-920 ^oC, 5 s^{-1}, 2s) described in Table 5-4. These two represent the two softening mechanisms observed in the steel at different hot rolling conditions. The samples deformed under conditions C (1000-820 ^oC, 0.1 s^{-1}, 20 s), D (1100-920 ^oC, 5 s^{-1}, 20 s), E (1100-920 ^oC, 5 s^{-1}, 2s), F (1000-820 ^oC, 5 s^{-1}, 20s), G (1100-920 ^oC, 25 s^{-1}, 20 s) and H (1000-820 ^oC, 50 s^{-1}, 20 s) all exhibited duplex structures consisting of large and small-sized grains similar to the observed structures of E shown in figure 5.21 (b) whereas figure 5.21 (a) presents the structure of a sample deformed under condition B consisting of equiaxed small-sized grains. A similar structure of small equiaxed grain size was also observed in samples deformed under condition A. It is clear from these quality maps that DRX occurred within conditions A and B whereas DRV occurred in the other rolling conditions C, D, E, F, G and H.

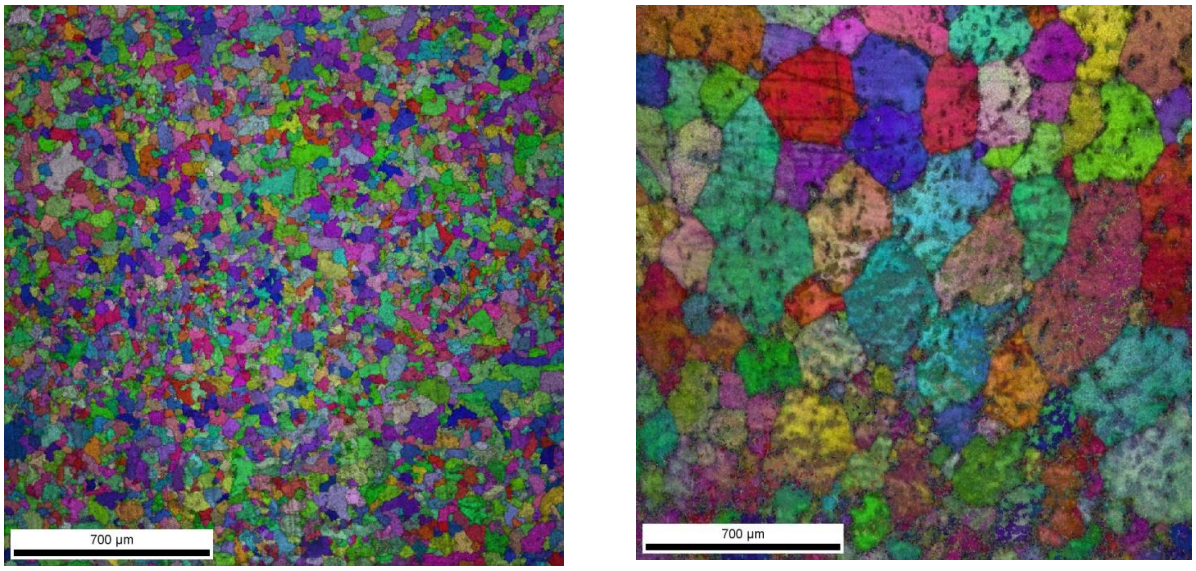

a b

Figure 5.21: Image quality maps of the AISI 430 samples deformed at (a) 1100 ^{o}C, 0.1 s^{-1}, 20 s (b) 1100 ^{o}C, 5 s^{-1}, 2 s

The grain boundary character distribution (GBCD) of the AISI 430 samples deformed under conditions A (1100 -920 ^{o}C, 0.1 s^{-1}, 2 s) and F (1000-820 ^{o}C, 5 s^{-1}, 20 s) are depicted in Figure 5.22 (a) & (b) respectively. The condition A exhibited the same GBCD as B whilst C, D, E, F, G and H showed similar GBCD conditions. The condition F sample had a number fraction of (~0.58) low angle grain boundaries (LAGBs), most probably due to arrangement of cells and subgrains [74], and also because of the development of a strong texture [57, 72]. A considerable fraction of high angle grain boundaries (HAGB) was also formed due to the accumulation of dislocations [46-59]. The fraction of high angle grain boundaries (HAGB) increased significantly from 0.38 to 0.59 after deformation under condition A. This could be attributed to the formation of recrystallized grains [46-49]. The coincident site lattice (CSL) fraction however remained similar in samples for all the rolling conditions. There is, therefore, a noteworthy dissimilarity between the GBCDs of samples after the rolling conditions A and F. This further confirms the occurrence of DRX in the samples deformed under conditions A and B and DRV in the samples under conditions C, D, E, F, G and H.

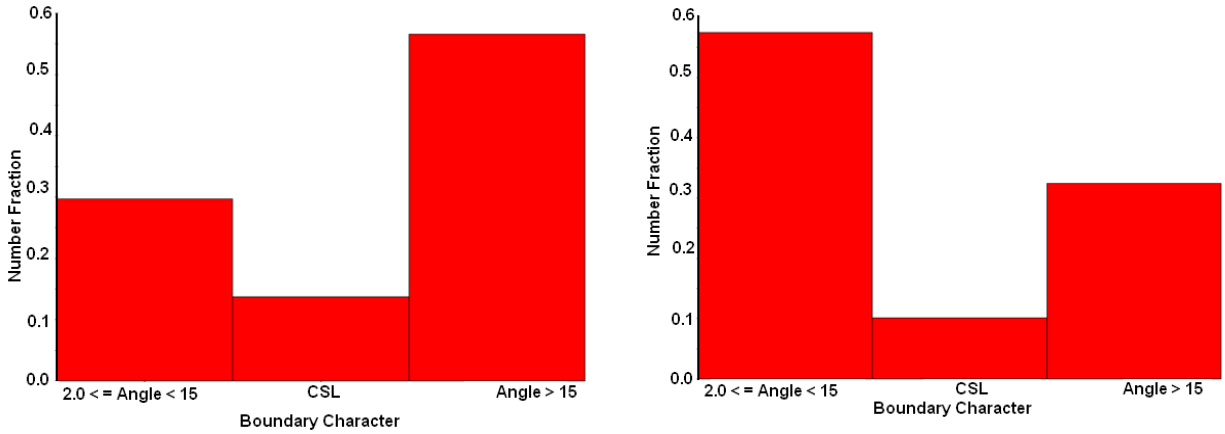

Figure 5.22: GBCD of the AISI 430 samples deformed at condition (a) 1100 – 920 ^{o}C, 0.1 s^{-1} and 20 s (b) 5 s^{-1}, 1000 ^{o}C – 920 ^{o}C and 20 s

These conditions responded to the development of different textures in the steels with the dominant texture found in all of these anisothermal simulated hot compression tests being strong α-fibre textures RD//<110> and weak γ- fibre textures ND<111>. These textures show slight differences in comparison with the as-received samples. The as-received hot rolled steel exhibited only a strong {011} <011> texture without a rotated cube texture.

5.7.2 Texture of the Plane Strain test samples from hot rolling in a laboratory mill

The hotband of the plane strain hot rolled samples exhibited a texture similar to that of the industrially as-received samples, see figure 5.23. It had a strong Goss texture and a weak rotated cube texture. The weak γ-texture found in this sample showed maximum at {111} <112> locations.

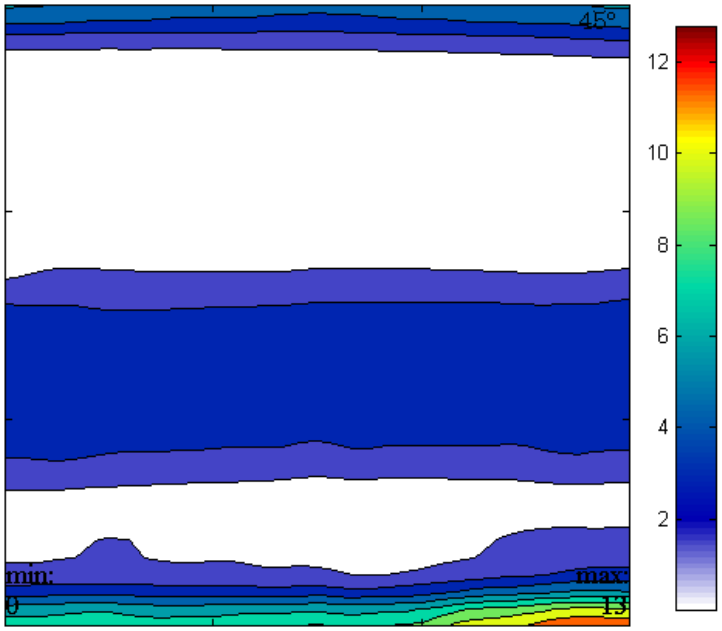

Figure 5.23: XRD ODFs of AISI 430 sample hot rolled under (plane strain condition) at a high strain rate of 50 s^{-1} and a temperature of 1100 ^{o}C-920 ^{o}C

The plane strain condition samples which had different cold rolling and annealing conditions applied to them did not show improved gamma fibre textures than the samples rolled under industrial conditions. The dominant textures found under different cold rolling and annealing conditions were strong γ- fibre textures {554}<225>, {111}<123> and strong α-fibre textures {111}<011>, {100}<011>, see figure 5.24. The presence of both α-fibre and γ- fibre textures if banded will lead to ridging in this steel. The textures obtained under these cold rolling and annealing conditions have no improvement over the industrially cold rolled and annealed samples. This suggests that optimum conditions for cold rolling and annealing are currently being used at Columbus Stainless Steels, hence the need to optimize the Steckel mill hot rolling conditions to obtain desired γ- fibre textures that will improve the ductility and formability of the steel as well as reduction or elimination of ridging in this grade of stainless steel.

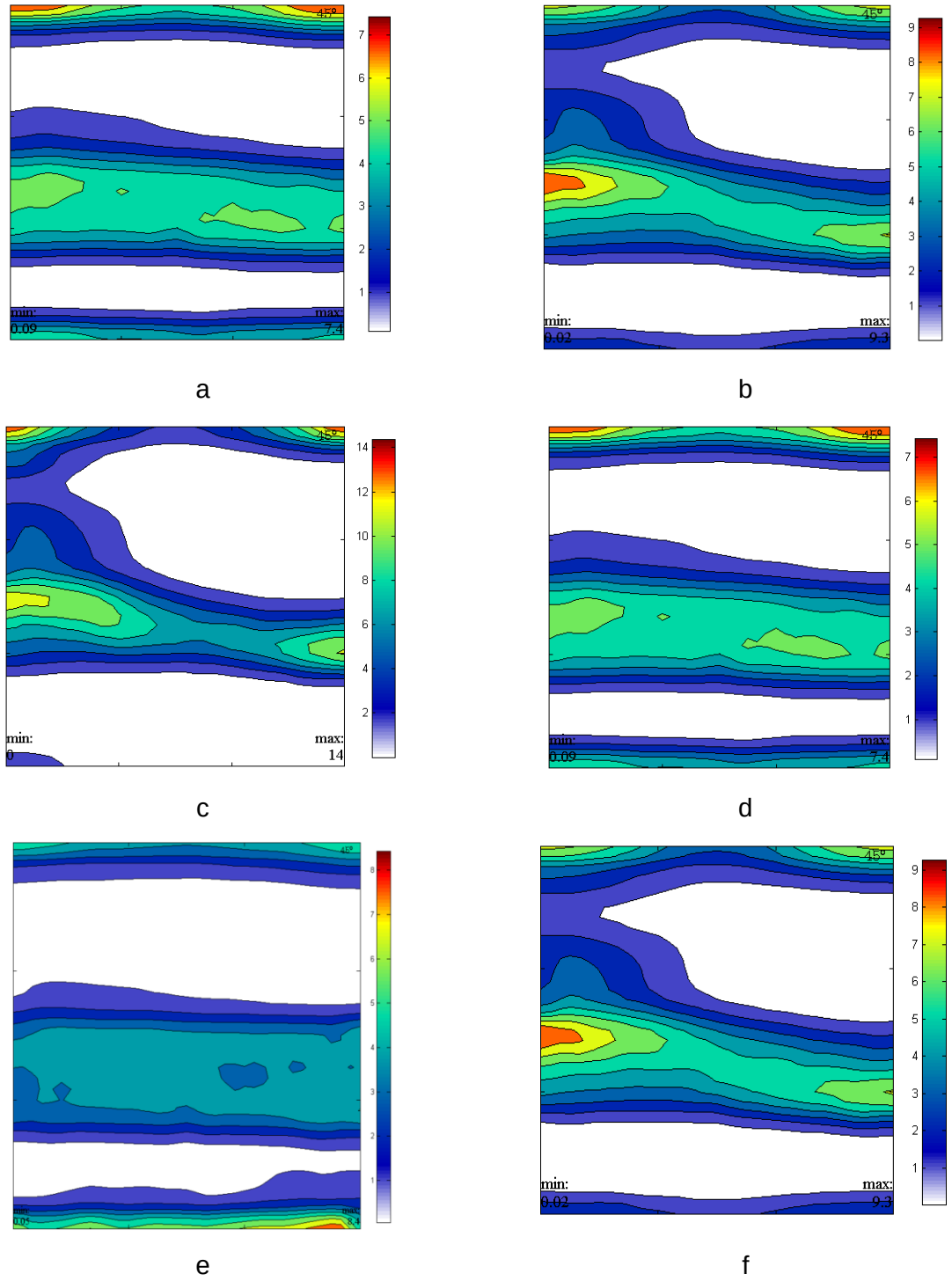

Figure 5.24: XRD ODFs of AISI 430 sample hot rolled under (plane strain condition) at strain rate of 50 s^{-1}, temperature of 1100 ^{o}C – 920 ^{o}C and cold rolled and annealed at (a) 80 % Reduction and annealed at 750 ^{o}C (b) 67 % reduction and annealed at 750 ^{o}C (c) 80 % reduction in 2 step with double annealing at 750 ^{o}C (d) 80 % reduction in a single step with single annealing at 750 ^{o}C, (e) 67 % reduction and annealed at 780 ^{o}C and (f) 67% reduction and annealed at 750 ^{o}C. The 80 % and 67% reductions were annealed for 3 and 4 minutes respectively

These conditions led to the formation of different textures in the steel. The summary of the analysis of these textures is presented in Table 5-6.

Table 5-6: Summary of the textures obtained from different hot rolling conditions of AISI 430

Details of the rolling Conditions		Observed textures
Strain rate = 0.1 s^{-1}, Td = 1100 ^{o}C, inter-pass time = 2 s		{011}<011>, {211}<111>, {554}<225>
Strain rate = 0.1 s^{-1}, Td = 1100 ^{o}C, inter-pass time = 20 s		{011}<011>, {554}<225>
Strain rate = 0.1 s^{-1}, Td = 1000 ^{o}C, inter-pass time = 20 s		{100}<001>, {554}<225>, {211}<011>
Strain rate = 5 s^{-1}, Td = 1000 ^{o}C, inter-pass time = 20 s		{100}<011>, {111}<123>, {554}<225>
Strain rate = 5 s^{-1}, Td = 1100 ^{o}C, inter-pass time = 2s		{100}<001>, {211}<111>, {211}<011>
Strain rate = 5 s^{-1}, Td = 1100 ^{o}C, inter-pass time = 20 s		{100}<011>, {211}<111>
Strain rate = 25 s^{-1}, Td = 1100 ^{o}C, inter-pass time = 20 s		{110}<001>, {211}<111>, {100}<011>
Strain rate = 50 s^{-1}, Td = 1000 ^{o}C, inter-pass time = 20 s		{011}<011>, {110}<112>, {100}<001>, {111}<123>
Plane strain condition	Hot rolled (Hotband)	{110}<001>, {110}<112>
	67 % Reduction cold work and annealed	{111}<011>, {100}<011>, {554}<225>
	80 % Reduction cold work and annealed	{100}<011>, {111}<011>
	Annealing at 750 ^{o}C	{100}<011>, {111}<011>, {554}<225>
	Annealing at 780 ^{o}C	{110}<001>, {110}<112>, {100}<011>
	Double annealing at 750 ^{o}C	{100}<011>, {554}<225>, {110}<011>
	Single annealing at 750 ^{o}C	{100}<011>, {110}<001>, {554}225>

*Td = Deformation temperature

5.8 Texture in AISI 433

The texture of the AISI 433 ferritic stainless steel hot rolled using conditions described in Table 5-4 are presented in figures 5.25 and 5.26. The samples hot rolled under conditions A (1100 -920 ^{o}C, 0.1 s^{-1}, 2 s) and B (1100-920 ^{o}C, 0.1 s$^{-1,}$ 20 s) presented similar textures but with differences in the improvement in the γ-fibre textures. The AISI 433 samples deformed under these two conditions (A and B) have both α-fibre (RD//<110>) and γ-fibre (<111>//ND) textures, as shown in figure 5.25. These conditions represent a combination of a high finishing rolling temperature and low strain rate with differences in the inter-pass time. Changing the inter-pass time from 2 s in A to 20 s in B, led to an increase in the intensity of {011}<011> texture from 2.5 in A to 5.3 in B. The second set of rolling conditions C (1000-820 ^{o}C, 0.2 s^{-1}, 20 s), D (1100-920 ^{o}C, 5 s^{-1}, 20 s), E (1100-920 ^{o}C, 5 s^{-1}, 2s) and F (1000-820 ^{o}C, 5 s^{-1}, 20 s) led to the formation of a strong {011}<011> component and weak γ-fibre textures {111}<123> and {554}<225>, as shown in Figure 5.26.

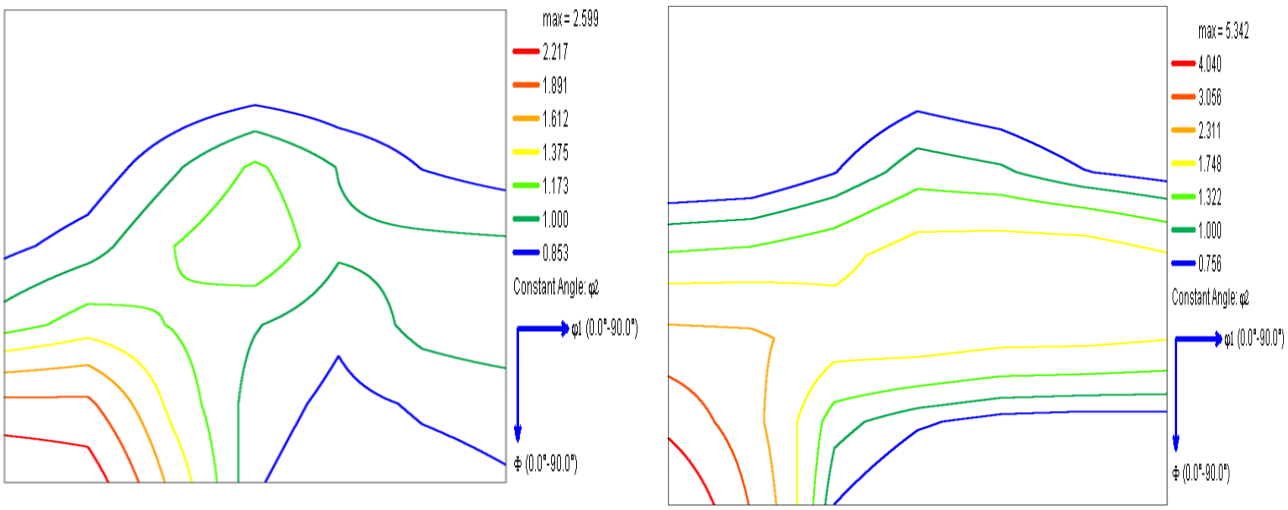

a b

Figure 5.25: EBSD ODF Φ_2 = 45^{o} RD-TD sections of the AISI 433 samples deformed at 1100 ^{o}C, to 820 ^{o}C, strain rate of 0.1 s^{-1} and inter-pass time of (a) 2 s (b) 20 s

Some observed textures at low strain rates of 0.1 s^{-1} were also present in the high strain rates conditions but with less intensities. With optimised cold work and annealing

conditions, these {011}<011> textures will transform into strong γ-fibre texture and a weak α- fibre texture.

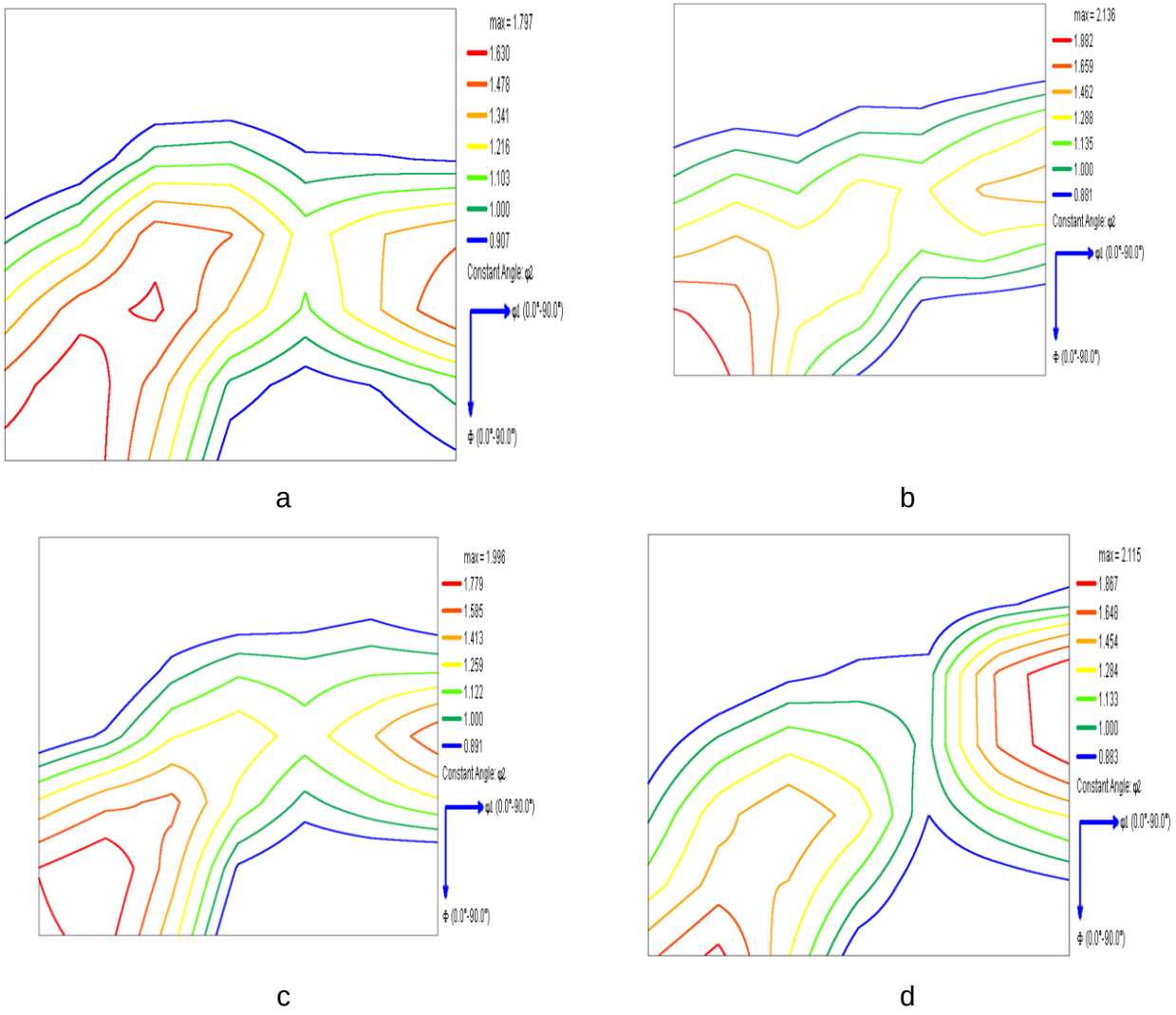

Figure 5.26: EBSD ODF Φ_2 = 45^o RD-TD sections of the AISI 433 samples deformed at : (a) 0.1 s^{-1}, 1000 ^{o}C – 820 ^{o}C and 20 s (b) 5 s^{-1}, 1100 ^{o}C – 920 ^{o}C, and 20 s (c) 5 s^{-1}, 1100 ^{o}C – 920 ^{o}C and 2 s (d) 5 s^{-1}, 1000 ^{o}C – 820 ^{o}C and 20 s

Conditions G (1100-920 ^{o}C, 25 s^{-1}, 20 s) and H (1000-820 ^{o}C, 50 s^{-1}, 20 s) also exhibited strong {011} <011> and {554} <225>, {111} <112> and no rotated cube component, see figure 2.7 (a) and (b).

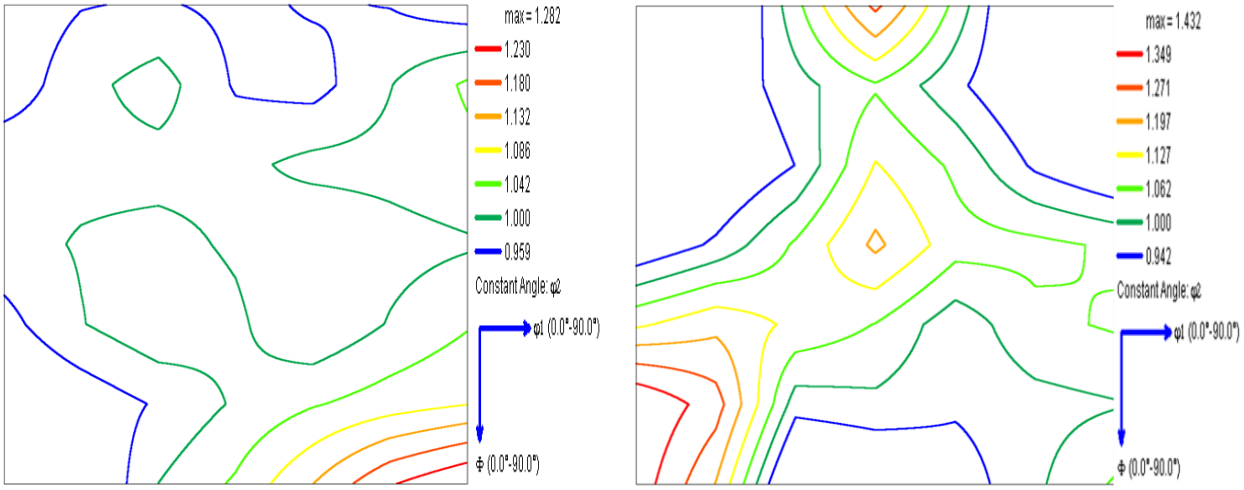

a b

Figure 5.27: EBSD ODF $\Phi_2 = 45^o$ RD-TD sections of the AISI 433 samples deformed at (a) 25 s^{-1}, 1100 ^oC – 920 ^oC and 20 s (b) 50 s^{-1}, 1000 ^oC – 820 ^oC and 20 s

By optimizing the cold rolling and annealing conditions, the conditions A and B can lead to desired γ-fibre textures whereas conditions C, D, E, F, G and H will lead to a blend of α-fibre and γ-fibre textures which if banded, can be considered as a recipe for ridging in this steel grade. The softening mechanisms identified in AISI 433 samples are similar to the softening mechanism identified in AISI 430 samples deformed at similar rolling conditions.

Figure 5.28 presents the image quality maps of the AISI 433 samples deformed under conditions B (1100-920 ^oC, 0.1 $s^{-1,}$ 20 s) and F (1000-920 ^oC, 5 s^{-1}, 20 s). The sample deformed under condition F exhibited a duplex structure consisting of large and small-sized grains as shown in figure 5.28 (b) whereas figure 5.28 (a) shows the structure of samples deformed under condition B consisting of almost only small equiaxed grains. Similar structures to F were observed in the 433 steel deformed under conditions C, D, E, G, and H whilst A and B shared a similar structure. It is evident from these quality maps that DRX occurred within the samples hot rolled under conditions A and B whereas DRV occurred within the samples deformed under conditions C, D, E, F, G and H.

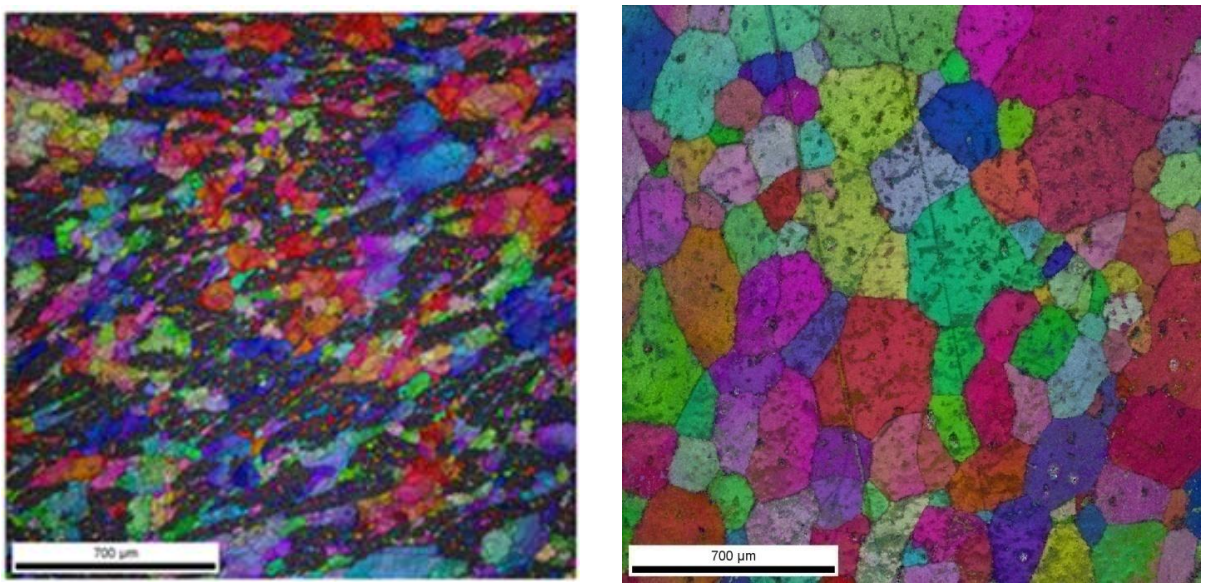

a b

Figure 5.28: Image quality maps of AISI 433 sample deformed at (a) 1100-920 ^{o}C, 0.1 s^{-1} 20 s (b) 1000-820 ^{o}C, 5 s^{-1} 20 s

The grain boundary character distribution (GBCD) of AISI 433 samples was similar to the AISI 430 samples with respect to the rolling conditions, as seen in samples deformed under conditions B and F, in Figure 5.29 (a) & (b) respectively. The condition B exhibited the same as A whilst C, D, E, G and H exhibited similar conditions as F. The fraction of high angle grain boundaries (HAGB) increased appreciably from 0.20 to 0.58 after deformation under condition B. This could be attributed to the formation of recrystallized grains [46-49]. The coincident site lattice (CSL) fraction decreased comparably in the sample F. This, therefore, shows a striking difference between the GBCDs between samples from the rolling conditions B and F. The interpretation of these GBCDs further confirms the occurrence of DRX at temperatures above 1000 ^{o}C and low strain rates whilst DRV occurs at temperatures below 1000 ^{o}C and high strain rates.

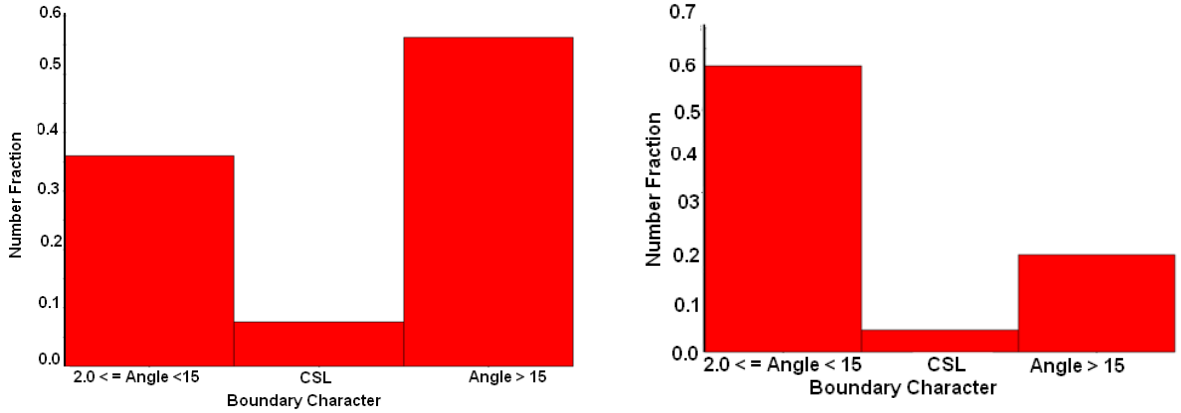

a b

Figure 5.29: GBCD of the AISI 433 samples deformed at condition (a) 1100-920 ^{o}C, 0.1 $s^{-1,}$ and 20 s (b) 1000-820 ^{o}C, 5 s^{-1}, and 20 s

5.8.1 Texture of the Plane Strain test samples from hot rolled in a laboratory mill

The hot band of AISI 433 samples hot rolled under plane strain conditions exhibited a texture similar to that of the industrially as-received samples, see figure 5.30. It exhibited a strong Goss textures {110} <001> and a weak γ-texture {554} <225> along with weak rotated cube component {100} <001>.

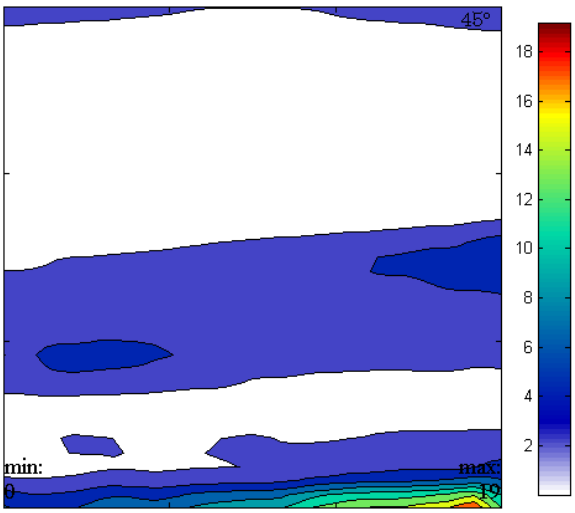

Figure 5.30 **:** XRD ODFs of AISI 433 sample hot rolled under (plane strain condition) at a high strain rate of 50 s^{-1}, a temperature of 1100 ^{o}C and an inter-pass time of 20 s

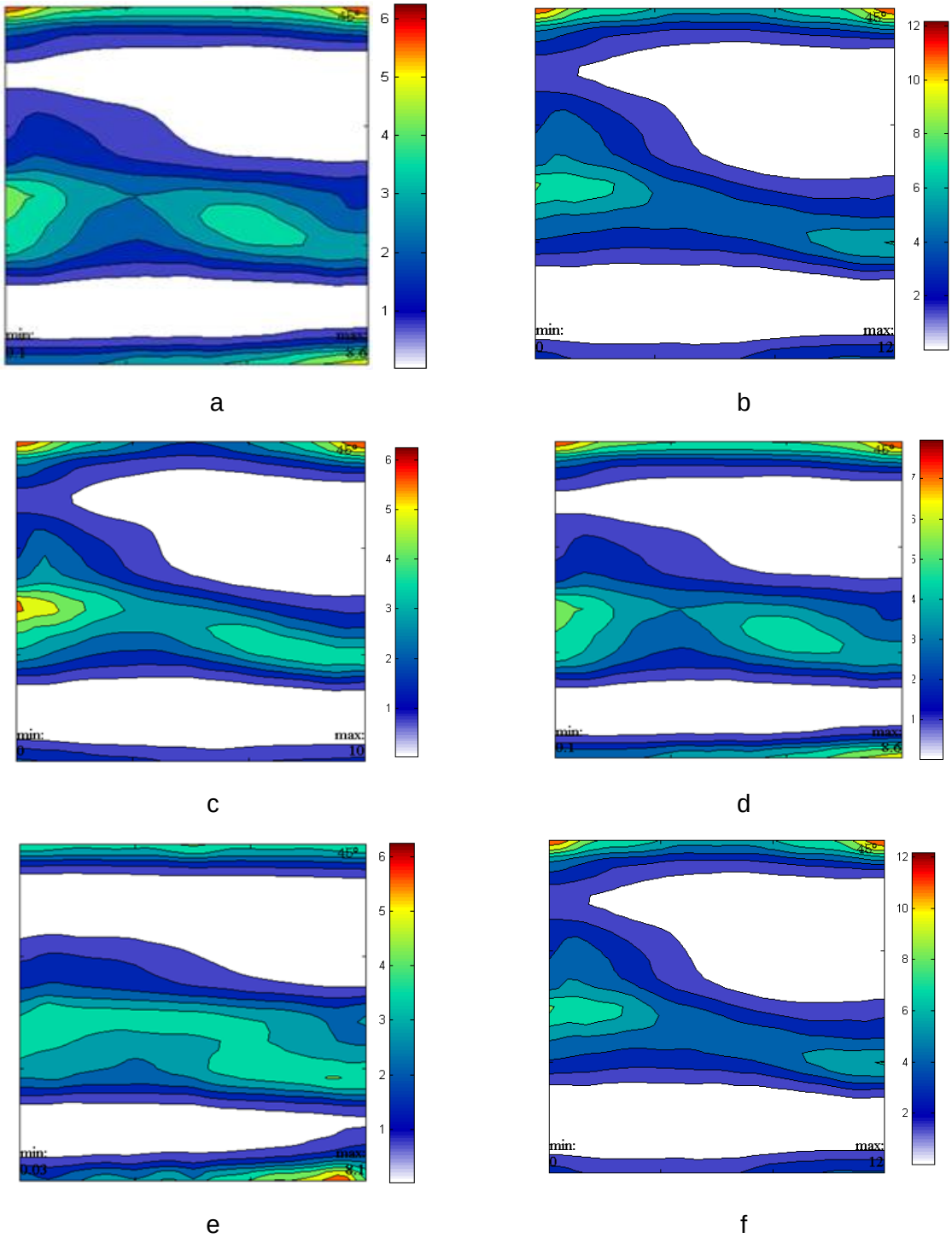

Figure 5.31 : XRD ODFs of AISI 433 sample hot rolled under (plane strain condition) at strain rate of 50 s^{-1}, temperature of 1100 ^{o}C – 920 ^{o}C and cold rolled and annealed at (a) 80 % Reduction and annealed at 750 ^{o}C (b) 67 % reduction and annealed at 750 ^{o}C (c) 80 % reduction in 2 step with double annealing at 750 ^{o}C (d) 80 % reduction in a single step with single annealing at 750 ^{o}C, (e) 67 % reduction and annealed at 780 ^{o}C and (f) 67% reduction and annealed at 750 ^{o}C. The 80 % and 67% reductions were annealed for 3 and 4 minutes respectively.

Similar to the AISI 430 steel, the major textures exhibited in AISI 433 under different reduction and annealing conditions are strong γ- fibre textures {554} <225>, {111} <123> and strong α-fibre textures {111} <011>, {100} <011> shown in figure 5.31. The combination of α-fibre textures and γ- fibre textures in the AISI 433 can result in ridging if banded. Comparatively the textures obtained in AISI 433 under these reductions and annealing conditions have less intensities and a lesser distribution of gamma fibre textures than the samples industrially cold rolled and annealed. It is therefore logical to optimize the Steckel mill hot rolling conditions to obtain the desired γ- fibre textures that will improve the ductility and formability of AISI 433 ferritic stainless steel as well as a reduction or elimination of ridging in this grade of ferritic stainless steel. These conditions corresponded to the formation of different textures in the steel. The analysis of textures found in this steel grade is summarised in Table 5-7.

Table 5-7**:** Summary of textures obtained from different hot rolling conditions of AISI 433

Description of the rolling Conditions		Observed textures
Strain rate = 0.1 s^{-1}, Td = 1100 ^{o}C, inter-pass time = 2s		{011}<011>, {554}<225>, {322}<236>, {111}<112>
Strain rate = 0.1 s^{-1}, Td = 1100 ^{o}C, inter-pass time = 20 s		{011}<011>, {111}<112>, {554}<225>
Strain rate = 0.1 s^{-1}, Td = 1000 ^{o}C, inter-pass time = 20 s		{011}<011>, {554}<225>, {322}<236>
Strain rate = 5 s^{-1}, Td = 1100 ^{o}C, inter-pass time = 20 s		{011}<011>, {554}<225>, {322}<011>
Strain rate = 5 s^{-1}, Td = 1100 ^{o}C, inter-pass time = 2s		{011}<011>, {111}<112>
Strain rate = 5 s^{-1}, Td = 1000 ^{o}C, inter-pass time = 20 s		{011}<011>, {211}<111>
Strain rate = 25 s^{-1}, Td = 1100 ^{o}C, inter-pass time = 20 s		{110}<001>
Strain rate = 50 s^{-1}, Td = 1000 ^{o}C, inter-pass time = 20 s		{100}<001>, {322}<236>, {011}<011>, {554}<225>
Plane strain condition	Hot rolled (Hotband)	{{110}<001>, {111}<112>
	67 % Reduction cold work and annealed	{100}<011>, {111}<011>, {554}225>
	80% Reduction cold work and annealed	{100}<011>, {110}<001>, {111}<011>
	Annealing at 750 ^{o}C	{100}<011>, {111}<011>, {554}225>
	Annealing at 780 ^{o}C	{110}<001>, {100}<001>, {554}225>
	Double annealing at 750 ^{o}C	{100}<011>, {111}<011>, {554}225>
	Single annealing at 750 ^{o}C	{110}<001>, {100}<011>,

The dominant textures found in all of these anisothermal simulated hot rolling tests were rotated cube textures {100} <001>, strong α-fibre textures RD//<110> and maximum γ-fibre (<111>//ND) textures at {111}<112> and {554} <225> locations. These textures show slight differences in comparison with the as-received samples.

5.9 Comparison of AISI 430 and AISI 433 textures

In sheet steels, particularly highly alloyed ferritic stainless steels, texture banding is frequently observed. During deformation processes, anisotropic plastic flow seems to occur in ferritic-stainless-steel sheet [81-84]. This leads to the exhibition of “ridging” or “roping” in the plane of the sheet [5]. Over the entire experimental range in this study the γ-fibre texture components increased in the texture intensity with respect to high rolling temperature, low strain rate and longer inter-pass times.

There were similarities in textures of AISI 430 and AISI 433, which apparently indicate that, the textures are likely to have been produced by similar mechanisms (dynamic recrystallization). One important step in determining the occurrence and extent of dynamic recrystallization was to follow the changes in the intensity of the texture components as the hot rolling parameters were varied. In AISI 430, the texture components have been produced basically by recrystallization whereas in the AISI 433 the rate of occurrence of recrystallization is also facilitated through the addition of Al which raised the A_{c1} temperature to ensure that the final rolling occurred at higher temperatures. Even though α-fibre RD//<110> and γ-fibre (<111>//ND) textures were observed in both grades, higher intensities of desired γ-fibre textures were realised in AISI 433 than AISI 430 which makes the additions of Al to the 430 to produce 433, a marginal improvement. At a rolling condition of 920 to 1100°C, a strain rate of 0.1 s^{-1}, and an inter-pass time of 20 s**,** the recrystallization texture becomes more pronounced in both AISI 430 and AISI 433.

6 CHAPTER 6: CONCLUSIONS AND RECOMMENDATIONS

6.1 Conclusions

It has been observed that groups of grains having a common crystallographic orientation can appear in ribbon-like form and can result in anisotropic banding. In ferritic stainless steel, such bands frequently consist of the cube-on-face texture component imbedded as layers in a cube-on-corner matrix. The foremost conclusions drawn from the results of these studies are as follows:

- The mill log analyses together with the hot compression test studies have revealed that both AISI 430 and AISI 433 ferritic stainless steels from Columbus Stainless Steels do exhibit a two-stage hot deformation behaviour which indicates two forms of softening mechanisms in these steel grades, i.e. as DRX and DRV.
- Dynamic recrystallization in both AISI 430 and AISI 433 does occur at temperatures above 1000 ^{o}C, strain rates below 5 s^{-1} and dynamic recovery at temperatures below 1000 ^{o}C.
- The dynamic recrystallization to dynamic recovery transition temperature was found to decrease with increasing strain rate in both grades of stainless steels.
- The dynamic recrystallization to dynamic recovery transition temperature was found to increase with increasing fixed inter-pass time in multi-pass testing in both grades of stainless steels.
- The simulated hot compressed samples exhibited a different texture from the as-received industrial hot rolled steel in both steels and this may be due to the differences in the strain per pass which is a limitation of the Gleeble equipment used as well as other differences between industrial and laboratory conditions.
- The AISI 433 shows a marginal improvement in the intensities of the observed and desired γ- fibre texture if compared to that of the AISI 430.
- Higher finishing rolling temperatures, lower strain rates and longer inter-pass times in multi-pass testing appear to improve the formation of the desired γ-fibre texture which contributes to ductility or drawability in these steels. A relatively stronger γ-fibre texture appears to be obtained under this condition.

6.2 Recommendations

From the analysis of these results, it is hereby recommended that the hot rolling temperatures be increased for rolling to occur above 1000 ^{o}C on the Steckel mill for both AISI 430 and AISI 433. Another hot rolling parameter that can be changed to obtain DRX is the inter-pas time whereas the low strain rates found under the laboratory conditions to promote DRX cannot, however, be considered under industrial conditions.

It will also be prudent to study the conditions that contribute to the formation of the Goss texture, the rotating cube texture {100}<001> associated with the transfer bars (roughing mill product) through the casting process as well as the alloying elements' contribution to the formation of texture in these grades of ferritic stainless steels.

REFERENCES

1. Automotive export manual – South Africa, (2011), pp 49-52. www.aiec.co.za.
2. Sello M.P., (2010), The laves phase embrittlement of ferritic stainless steel type AISI 441. Doctoral Thesis, University of Pretoria. Pretoria, South Africa. pp 26. www.upetd.up.ac.za/thesisavailable
3. Kim S. and Yoo Y., (2002), Continuous dynamic recrystallization of AISI 430 ferritic stainless steel. Metals and Materials International, Vol. 8, pp 7-13.
4. Raabe D. and Lucke K., (1992), Influence of particle on recrystallization texture of ferritic stainless steels. Materials Technology, Vol. 10, pp 457-464.
5. Shin H.J., An J.K., Park S.H. and Lee D.N., (2003), The effect of texture on ridging of ferritic stainless steel. Acta Mater, Vol. 51, pp 4693-4706.
6. Engler O., Huh M. and Tomé C.N., (2005), Crystal-plasticity analysis of ridging in ferritic stainless steel sheets. Metallurgical and Materials Transactions A, Vol. 36A, pp 3127 – 3139.
7. Wu P.D., Lloyd D.J. and Huang Y., (2006), Correlation of ridging and texture in ferritic stainless steel sheet. Materials Science and Engineering A, Vol. 427, pp 241–245.
8. Wu P.D., Jin H., Shi Y. and Lloyd D.J., (2006), Analysis of ridging in ferritic stainless steel sheet. Materials Science and Engineering, Vol. 423, pp 300-305.
9. Harase J., Ohta K., Takeshita T. R. and Schimizu R., (1990), Materials Science Forum, Vol. 14, pp 296–303.
10. Columbus Stainless Steel Technical data, CS430. www.columbusstainless.co.za
11. McGuire, (2008), Stainless steel for designers: ASM International, pp 69.
12. Rostfreie Edelstahl Stainless Steels, (2011), www.lucefin.com
13. Ustinovshikov Y., Pushkarev B. and Igumnov I., (2002), Fe-rich portion of the Fe-Cr phase diagram: electron microscopy study. Journal of Materials Science, Vol. 37, pp 2031-2042.
14. Anderson J. and Sundman B., (1987), Thermodynamic properties of the Cr-Fe system. CALPHAD, Vol. 11, pp 83-92.
15. Moeed K.M., (2012), The emphasis of phase transformations and alloying constituents on hot cracking susceptibility of type 304 and 316 stainless steel

welds. International Journal of Engineering Science and Technology, Vol. 4, pp 2206-2216.

16. Kim S.H., Moon H.K., Kang T., Lee C.S., (2003), Dissolution kinetics of delta ferrite in AISI 304 stainless steel produced by strip casting process. Materials Science and Engineering, Vol. 356, pp 390-398.
17. Meyrick G. and Wagoner R.H., (2001), Physical metallurgy of steels, class notes and lecture materials for MSE 651.01. The Ohio State University, USA. pp 11.
18. Mehran M., (2007), The effects of alloying elements on steels (I). Christian Doppler Laboratory for Early Stages of Precipitation, Institute of Materials Science, Welding and Forming shaping methods. Graz University of Technology. Technical Report, pp 22 -24.
19. Sello M.P. and Stumpf W.E., (2010), Laves phase embrittlement of the ferritic stainless steel type AISI 441. Materials Science and Engineering A, Vol. 527, pp 5194–5202.
20. Ryan N.D. and McQueen H.J., (1990), Flow stress, dynamic restoration, strain hardening and ductility in hot working of 316 stainless steel. Journal of Materials Processing Technology, Vol. 21, pp 177-199.
21. Grobner P.J., (1973), The 885 (475) embrittlement of ferritic stainless steels. Metallurgical Transactions, Vol. 4, pp 251.
22. Designer hand book for stainless steel fabrication, pp 10-12. www.ssina.com
23. Cabrera J.M., Omar A.A., Jonas J.J. and Prado J.M., (1997), Modelling the flow behaviour of a medium carbon microalloyed steel under hot working conditions. Metallurgical and Materials Transactions A, Vol. 28A, pp 2233 – 2243.
24. Lin Y.C., Fang X. and Wang Y.P., (2008), Predicted metadynamic softening in a multi-pass hot deformation low alloy steel using artificial neural network. Journal of Materials Science, Vol. 43, pp 5508-5515.
25. Dziedzic M. and Turczyn S., (2010), Experimental and numerical investigation of strip rolling from dual phase steel. Archives of Civil and Mechanical Engineering Vol. 4, pp 21 -30.
26. Kuziak R., (2006), Physical simulation of thermomechanical treatment employing gleeble 3800 simulator. Metal Transactions, pp 232-243.

27. Muller B.W., Cortie M.B. and Matthews L.M., (1990), Simulating the production of deep-drawable AISI 430 stainless steel. Journal of the South African Institute of Mining and Metallurgy, Vol. 90, pp 17-26.
28. Knudsen W., Sankar J., MaQueen H.J., Jonas J.J. and Hawkins D.N., (1980), Simulation of rolling schedules for HSLA steels. Hot Working and Forming Processes Conference, Sheffield. Metal Society of London, pp 51-56.
29. Sah J.P. and Sellars C.M., (1979), Effect of deformation history on static recrystallisation and restoration in ferritic stainless steel. The Metals Society of London.
30. Mirzadeh H. and Najafizadeh A., (2010), Flow stress prediction at hot working conditions. Materials Science and Engineering A, Vol. 527, pp 1160-1164.
31. Salgado M.F., Sabioni A.C.S., Huntz A. and Rossi E.H., (2008), High temperature oxidation behaviour of the AISI 430 and AISI 430E stainless steels in $Ar/H_2/H_20$ atmosphere. Materials Research, Vol. 11, pp 1516.
32. Sellars C.M., (1990), Modelling microstructural development during hot rolling. Materials Science and Technology, Vol. 6, pp 1072-1081.
33. Pistorius P.C. and Coetzee M., (1996), Sensitization of type 430 ferritic stainless steel during continuous annealing. The Journal of The South African Institute of Mining and Metallurgy, Vol. 96, pp 119-125.
34. Zhu L., Di W. and Zhao X., (2005), Recrystallization modelling of hot deformed Si-Mn TRIP steel. Journal of Iron and Steel Research International, Vol. 14, pp 61-65.
35. Dieter G., (1988), Mechanical Metallurgy. SI edition, McGraw – Hill, pp 519-522.
36. Stumpf W., (2003), Grain size modelling of a low carbon strip steel during hot rolling in a compact strip production (CSP) plant using the hot charge route. Journal of The South African Institute of Mining and Metallurgy, pp 617-630.
37. Gur C.H. and Pan J., (2009), Thermal process modelling of steels. Taylor and Francis, Group, LLC, NY, pp 93-99.
38. Hamada J., Ono N. and Inoue H., (2011), Effect of texture on r-value of ferritic stainless steel sheets. ISIJ International, Vol. 51, pp 1740 -1748.
39. Totten G.E., (2006), Steel heat treatment handbook, metallurgy and technologies. Second Edition, Taylor and Francis Group LLC, NY, pp 234 – 242.

40. Amuda M.O.H. and Mridha S., (2009), Microstructural features of AISI 430 ferritic stainless steel weld produced under varying process parameters. International Journal of Mechanical and Materials Engineering (IJMME), Vol. 4, pp 160-166.
41. Ryan N.D. and McQueen H.J., (1986), Mean pass flow stresses and inter-pass softening in multi-stage processing of carbon, HLSA, tool and stainless steels. Journal of Mechanical Working Technology, Vol. 12, pp 323-349.
42. Xu W. and Ferry M., (2005), Influence of starting microstructure on texture development in cold rolled and annealed low carbon steel strip. Materials Science Forum, Vol. 495, pp 519-524.
43. Bai D.Q., Yue S., Sun W.P. and Jonas J.J., (1993), Effect of deformation parameters on the no-recrystallisation temperature in Nb-bearing steels. Metallurgical Transactions A, Vol 24, pp 2151-2159.
44. Ma B., Peng Y., Jia B. and Liu Y., (2010), Static recrystallization kinetics model after hot deformation of low-alloy steel Q345B. Journal of Iron and Steel Research International, Vol. 17, pp 61-66.
45. Stumpf W.E., (2010), Lecture notes: Advanced course on phase transformations in metals and their alloys, University of Pretoria. Pretoria, South Africa. pp 5.1-1 – 5.7-3.
46. McQueen H.J. and Jonas J.J., (1975), Recovery and recrystallization during high temperature deformation. Treatise on Materials Science and Technology, Vol. 6, pp 393.
47. Yazdipour N., Dehghan-Manshadi A., Davies C.H.J. and Hodgson P.D., (2007), Simulation of dynamic recrystallization using irregular cellular automata. Materials Forum, Vol. 31, pp 164 -176.
48. NajafiZadeh A., Jonas J.J. and Yue S., (1992), Grain refinement by dynamic recrystallization during the simulated warm-rolling of interstitial free steels. Metallurgical Transactions A, Vol. 23, pp 2607-2617.
49. Wang Z., Guo Y., Xue W., Liu X. and Wang G., (2007), Effect of coiling temperature on the evolution of texture in ferritic rolled Ti-IF steel. Journal of Materials Science and Technology, Vol. 23, pp 337-341.
50. Poliak E.I. and Jonas J.J., (2003), Initiation of dynamic recrystallization in constant strain rate hot deformation. ISIJ International, Vol. 43, pp 684-691.

51. Yan J., Bi H., Li X. and Xu Z., (2009), Microstructure, texture and grain boundaries character distribution evolution of ferritic stainless steel during rolling process. Journal of Materials Processing Technology, Vol. 209, pp 2627-2631.
52. Zheng C., Xiao N., Li D. and Li Y., (2008), Microstructure prediction of the austenite recrystallization during multi-pass steel strip hot rolling: A cellular automaton modelling. Computational Materials Science, Elsevier, Vol. 44, pp 507–514.
53. Bakkalog˘lu A., (2002), Effect of processing parameters on the microstructure and properties of Nb microalloyed steel. Materials Letters, Vol. 56, pp 200-209.
54. DeArdo I.A., (1998), Mechanical behaviour of IF 409 ferritic stainless steel. MEng Thesis, McGill University. Montreal, Canada. pp 31.
55. Jafari M., Najafizadeh A. and Rasti J., (2007), Dynamic recrystallization by necklace mechanism during hot deformation of 316 stainless steel. International Journal of ISSI, Vol. 4, pp 16-23.
56. Suwas S. and Gurao N.P., (2008), Crystallographic texture in materials. Journal of the Indian Institute of Science, Vol. 88, pp 151-177.
57. Hutchinson W.B. and Hatherley M., (1979), An introduction to textures in metals. Chameleon Press Ltd., London.
58. Ray R.K., Jonas J.J. and Hook R.E., (1994), Cold rolling and annealing textures in low carbon and extra low carbon steels. International Materials Review, Vol. 39, pp 129-171.
59. Engler O. and Randle V., (2010), Introduction to texture analysis (macrotexture, microtexture and orientation mapping). Second Edition, Taylor and Francis Group, LLC, NY, pp 51-71 and 203-240.
60. Kestens L., Jonas J.J., (1996), Modelling texture change during the static recrystallization of interstitial free steels. Metallurgical and Materials Transactions A, Vol. 27, pp 155 -164.
61. Schwartz A.J., Kumar M. and Adams B.L., (2000), Electron backscatter diffraction in materials science. Review, Kluwer Academics / Plenum publishers, 233 Spring Street, New York, NY 10013.
62. Kamayaa M., Wilkinson A.J. and Titchmarsh J.M., (2005), Measurement of plastic strain of polycrystalline material by electron backscatter diffraction. Nuclear Engineering and Design, Elsevier, Vol. 235, pp 713–725.

63. Ruiz-Apariiw L., Garcia C.I. and DeArdo A.J., (2000), development of {111} transformation texture in interstitial free steels. Metallurgical and Metal Transactions A, Vol. 32, pp 2001-2325.
64. Chao, H.C., (1967), Mechanism of anisotropic lamellar fractures. Metallurgical Trans. ASM, Vol. 60, pp 37-50.
65. Wright R.N., (1972), Metall. Trans., Vol.3, pp 83-91.
66. Jeong W.C., (2008), Effect of hot-rolling temperature on microstructure and texture of an ultra-low carbon Ti-interstitial-free steel. Materials Letters, Vol. 62, pp 91-94.
67. Brochu M., Yokota T.S. and Satoh S., (1997), Analysis of grain colonies in type 430 ferritic stainless steels by electron back scattering diffraction (EBSD). ISIJ International, Vol. 37, pp 872–877.
68. Wu P.D., Lloyd D.J. and McEwen S.R., (2003), A simple model describing roping in Al sheet. Scripta Materialia, Vol. 48, pp 1243–1248.
69. Takechi H., Kato H., Sunami T. and Nakayama T., (1967), Mechanism of ridging formation in 17 % chromium stainless steel sheet. Trans. JIM, vol. 31, pp 717-23.
70. Sung J.H., Kong J.H., Yoo D.K., On H.Y., Lee D.J. and Lee H.W., (2008), Phase changes of the AISI 430 ferritic stainless steels after high-temperature gas nitriding and tempering heat treatment. Materials Science and Engineering A, Vol. 489, pp 38-43.
71. Jin H. and Gupta A.K., (2006), The effect of through thickness texture inhomogeneity on roping behaviour in AA661Al-Si-Mg alloy. Materials Science Forum, Vol. 702, pp 273-278.
72. Becker R., (1998), Effects of strain localization on surface roughing during sheet forming. Acta Materiallia, Vol. 46, pp 1385–1401.
73. Knutsen R., (2007), Correlating microstructural features and surfacing roughening in ferritc stainless steel. Materials Science Forum, Vol. 550, pp 65-74.
74. Saha R., Ray R.K. and Bhattacharjee D., (2007), Attaining deep drawability and non-earing properties in Ti + Nb interstitial-free steels through double cold rolling and annealing. Scripta Materialia, Vol. 57, pp 257–260.
75. Wu P.D., Lloyd D.J., Bosl A., Jin H. and McEwen S.R., (2003), Analysis of roping in AA6111 automotive sheet. Acta Materialia, Vol. 51, pp 1945–1957.

76. Beaudoin A.J., Bryant J.D. and Korzekwa D.A., (1998), Analysis of ridging in aluminium auto body sheet metal. Materials Transaction, Vol. 29, pp 2323–2332.
77. Wittridge N.J. and Knutsen R.D., (1999), Microtexture base analysis of the surface roughing behaviour of aluminium alloy during tensile deformation. Materials Science and Engineering A, Vol. 269, pp 205-216.
78. Raabe D., Sachtleber M., Weiland H., Scheele G. and Zhao Z., (2003), Grain-scale micromechanics of polycrystal surfaces during plastic straining. Acta Materialia, Vol. 51, pp 1539–1560.
79. Wu P.D. and Lloyd D.J., (2004), Analysis of surface roughening in AA6111 automotive sheet. Acta Materialia, Vol. 52, pp 1785–1798.
80. Held F., (1965), Mechanical working and steel processing: (ed.D.A.Edgecombe). American Institute of Mining, Metallurgical and Petroleum Engineers.
81. Tomida T. and Wakita M., (2012), Transformation texture in hot-rolled steel sheets and its quantitative prediction. ISIJ International, Vol. 52, pp 601–609.
82. Raabe D., (2003), Overview on basic types of hot rolling textures of steels. Materials Technology of Steel Research, Vol. 74, pp 327-337.
83. Holscher M., Raabe M. and Lucke K., (1991), Rolling and recrystallization texture of bcc steels. Materials Technology of Steel Research, Vol. 62, pp 567-575.
84. Raabe D., (1995), Materials Technology of Steel Research, Vol. 65. www.mpie.de
85. Petrov R., Kestens L., Wasilkowska A., and Houbaert Y., (2007), Microstructure and texture of a lightly deformed TRIP – assisted steel characterized by means of the EBSD technique. Materials Science and Engineering, Vol. 447, pp 285-297.
86. Raabe D. and Ylitalo M., (1996), Experimental investigation of the transformation texture in hot-rolled ferritic stainless steel using single orientation determination. Metallurgical Transactions, Vol. 27A, pp 49-57.
87. Hamada J., Ono N. and Inoue H., (2011), Effect of texture on r-value of ferritic stainless steel sheets. ISIJ International, Vol. 51, pp 1740-1748.
88. Bennett T.A., Petrov R.H. and Kestens L.A.I., (2010), Surface texture modification for improved roping behaviour of aluminium alloy 6016. Solid State Phenomena, Vol. 160, pp 197-202.

89. Jinxia L., Zhanying L., Cairu G., Zhaodong W., Xianghua L. and Guodong W., (2005), Evolution of textures in interstitial free steel during multiple cold rolling and annealing. Journal of Materials Processing Technology, Vol. 167, pp 132-137.
90. Davison R.M., (1974), Formability of low–interstitial 18% Cr-2%Mo ferritic stainless steel. Metallurgical Transactions, Vol. 5, pp 2294.
91. Singh C.D., (1996), Effect of annealing on hot band texture of ferritic stainless steel. Textures and Microstructures, Vol. 26, pp 445-468.
92. Filho A.F., Herrera C., De Lima N.B., Plaut R.L. and Padilha A.F., (2007), Texture evolution of ferritic (AISI 430) stainless steel strips during cold rolling, annealing and drawing. Materials Science Forum, Vol. 539, pp 4926-4931.
93. Schneider A. and Inden G., (2005), Simulation of kinetics of precipitation reactions in ferritic steels. Acta Materialia, Vol. 53, pp 519-531.
94. Miettien J., (1998), Approximate thermodynamic solution phases data for steels. CALPHAD, Vol. 22, pp 275-300.

7 APPENDIX A: Determination of the Ac_1 and the phase transformation temperatures using the Baehr dilatometer.

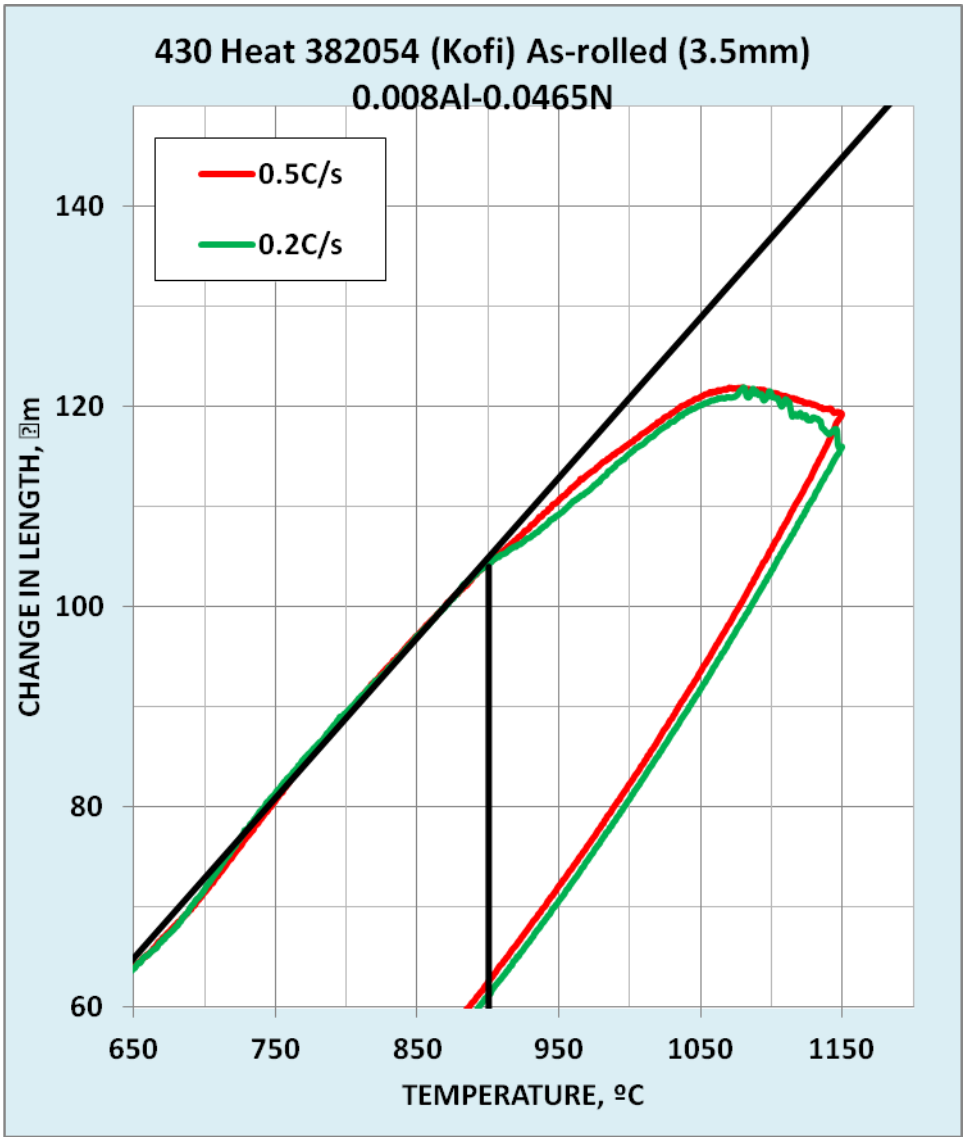

Figure 7.1: Ac_1 temperature of AISI 430 determined from Bhaer dilatometer (indicated on the figure by a thick solid black line) to be 900 ^{o}C.

8 APPENDIX A: Determination of the Ac_1 and the phase transformation temperatures using the Baehr dilatometer.

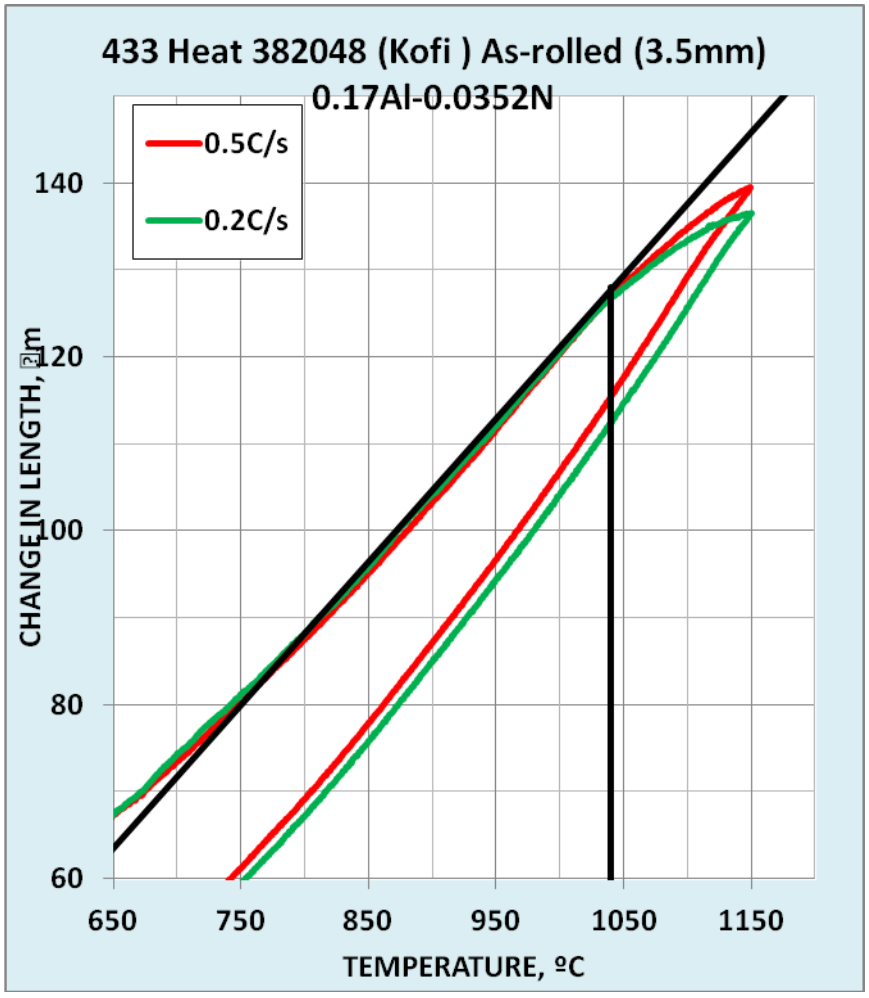

Figure 8.1**:** Ac_1 temperature of AISI 433 determined from Bhaer dilatometer (indicated on the figure by a thick solid black line) to be 1035 ^{o}C.

9 APPENDIX B: Template used in calculating true stress and true strain from the Gleeble data.

Exp/series no:	LK 2	Material:	AISI 430	Cast/slab no	NA	Condition:	Hot rolled	Test date	23-May-12	
Main purpose of test	To simulate the hot rolling process on the Steckel mill		Initial sample dimensions	D(0) cold mm	H(0) cold mm	D(0) hot mm	H(0) hot mm			
				10.001	15.001	10.147	15.220			
Heat to 1100 deg at 10 deg/s, hold at 1150 deg for 5 mins, lower to 1100 at 10 deg/s			Final sample dimensions	D(f) cold mm	H(f) cold mm	D(f) hot mm	H(f) hot mm		Inter-pass time	20
				16.89	6.09	17.136	6.179			
		Plan'd def t	105.80	Actual stroke	-0.003	Barrel factor	0.86			
Gleeble prg		Act def time	471.46	Plan'd strain	5.000	Plan'd str rte	5.000			
Load cell	1.000	Plan'd def T	1100	Actual strain	0.000	Calc str rte	0.000			
Corr factor	NA	Meas def T	1086	Meas cold str	1.041	Cold str rt	0.002			

Gleeble prg data point	Gleeble time seconds	Temp. meas. Deg C	Gleeble stroke mm	Gleeble force kN	Zero'd Gleeble stroke mm	Zero'd Gleeble force N	True strain (negative)	Flow stress (no friction) MPa	Von Mises flow stress (fr=0.2) MPa	Cum stress/ strain (no friction)	Cum stress/ strain (fr=0.2)
0	0	34	0.042045	-1.2349	0.0000	0.00	0.000	0.0	0.0	0.00	0.00
1	5	33.704	0.046201	-1.0142	0.0042	220.70	0.000	-2.7	-2.7	0.00	0.00
2	9.8693	65.187	0.068113	-1.0194	0.0261	215.50	-0.002	-2.7	-2.6	0.01	0.01
3	14.8693	116.97	0.092367	-1.0159	0.0503	219.00	-0.003	-2.7	-2.7	0.01	0.01
4	17.9917	145.74	0.11134	-1.017	0.0693	217.90	-0.005	-2.7	-2.6	0.02	0.02
5	22.9917	194.51	0.13792	-1.0161	0.0959	218.80	-0.006	-2.7	-2.7	0.02	0.02
6	26.1431	224.29	0.15559	-1.0157	0.1135	219.20	-0.007	-2.7	-2.7	0.02	0.02
7	31.1431	272.38	0.18338	-1.0162	0.1413	218.70	-0.009	-2.7	-2.7	0.03	0.03
8	34.2804	302.37	0.20142	-1.0164	0.1594	218.50	-0.010	-2.7	-2.7	0.03	0.03
9	39.2804	350.54	0.23038	-1.0161	0.1883	218.80	-0.012	-2.7	-2.7	0.04	0.04
10	42.4172	380.78	0.24862	-1.0164	0.2066	218.50	-0.013	-2.7	-2.7	0.04	0.04
11	47.4172	428.95	0.27799	-1.0165	0.2359	218.40	-0.015	-2.7	-2.7	0.04	0.04
12	50.5436	459.02	0.2962	-1.0162	0.2542	218.70	-0.017	-2.7	-2.7	0.05	0.05
13	55.5436	507.4	0.3242	-1.0158	0.2822	219.10	-0.018	-2.8	-2.7	0.05	0.05
14	58.7803	538.55	0.34081	-1.0147	0.2988	220.20	-0.019	-2.8	-2.7	0.06	0.06
15	63.7803	586.7	0.36116	-1.0123	0.3191	222.60	-0.021	-2.8	-2.8	0.06	0.06
16	66.9152	616.33	0.37242	-1.0124	0.3304	222.50	-0.021	-2.8	-2.8	0.06	0.06
17	71.9152	665.84	0.38807	-1.0072	0.3460	227.70	-0.022	-2.9	-2.8	0.06	0.06

10 APPENDIX C: Equations used for mill log analyses [36]

Eq. No.	EQUATIONS		DEFINITIONS
Sims Working Rolls corrective equations			
1 2	Flattened Work Roll radius	$R' = R\{1+(CP)/w\Delta h\}$ $C = \frac{16(1-\nu^2)}{\pi E}$	R' = flattened work roll radius (mm) R = nominal radius (mm) V = poison's ratio E = Young's modulus of outer skin of Material (GPa) P = roll force (N) W = width of plate(mm $\Delta h = (h_f - h_i)$ = reduction of thickness (mm)
Sims Mean Flow Stress calculations from mill log data			
3		$MFS_{sims} = \frac{P}{[(2/\sqrt{3})w\{R'(h_f - h_i)\}^{1/2}Q}$ $Q = [(\frac{1}{2})\{(1-r)/r\}^{1/2}\{K_3 - K_4\} - (\frac{\pi}{4})]$ $K_3 2\pi K_2$ $K_2 = [(\frac{1}{2})\tan^{-1}\{r/(1-r)\}^{1/2}]$ $K_1 = (\pi/8)(h_i/R')^{1/2}\ln(1-r)$ $K_4 = \{R'/h_i\}^{1/2}\ln[(Y/h_i)^2(1-r)$ $\phi = \{\tan(K_1 + K_2)\}\{h_i/R'\}^{1/2}$	MFS_{sims} = mean flow stress according to Sims (MPa) P = roll force (MN) W = plate width (mm) $r = (h_f - h_i)/h_i$